Université de Montréal

Moems 2 x 2 Switch Fabrics for all Optical Networking Applications

par
Nan Zhang
Département de Physique
Faculté des arts et des sciences

Thèse présentée
À la Faculté des études supérieures
en vue de l'obtention du grade de
philosophiae Doctor (Ph. D.)
En physique

July 2001

UNIVERSITÉ DE MONTRÉAL

Cette thèse intitulée:

MOEMS 2X2 SWITCH FABRICS FOR ALL OPTICAL NETWORKING APPLICATIONS

présentée par: **ZHANG, Nan**

en vue de l'obtention du diplôme de: **Philosophiae Doctor**

a été dûment acceptée par le jury d'examen constitué de:

M LESSARD Louis,	**Ph.D., président**
M. ROORDA Sjoerd,	**Ph.D., membre et directeur de recherche**
M. POLLA Dennis,	**Ph.D., membre et co-directeur de recherche**
M. MEUNIER Michel,	**Ph.D., membre**
M. RIZA Nabeel ,	**Ph.D., membre**

To the memory of my father

ACKNOWLEDGMENTS:

The successful completion of this thesis critically depended on the countless contributions from people throughout my academic life, including my formative years as an undergraduate and graduate student at Optics Department and National Lab of Crystal Materials, Shandong University. I am forever in debt to the many people who provided me with friendship and comradeship, whom I cannot acknowledge by name.

Of great benefit during my years in the Ph.D. program was having Dr. Sjoerd Roorda and Dr. Dennis Polla as my research advisors. I admire their talent, ability, consideration, thoughtfulness, and integrity. It was a real boon to learn from them and to work with them. I am sincerely grateful to them and attribute what I have accomplished during my Ph.D. study to their supervision, support, and mentorship.

I am equally grateful to MTL stuffs at University of Minnesota who gave much needed assistance to this project. Kevin Roberts helped me with wafer dicing; Mark Fisher made many important suggestions on processing details and mask generations; Suzanne Miller made deep etcher, the critical equipment for the processing, always ready for access; Tony, Kathy, Greg and Karen are always approachable, friendly, patient, supportive through all my time spent at MTL. Particularly, I would like to thank Ms.

Louise Larfortune at University of Montreal for her kind help and endless support through my doctoral program while I was away from the University.

I am grateful to my colleague in ADC, whose diligent efforts in maintaining and improving the performance of the lots of complicated equipment has been instrumental in the completion of this project. I would like to thank Souksmay Chouleymantry and Susan Bromley for their technical assistance throughout this project, and Mitch Voel for ANSYS assistants.

Finally, my deep thanks must go to ADC management team in optical fiber division, Gary Nault, Rod Christensen and Rick Makloski. Without their support, their encouragement and their supervision I would never have a chance to complete my doctoral program. "Thanks" from my heart!

ABSTRACT:

The current explosion of communication traffic volume is driven by an insatiable appetite for Internet Connectivity on geographic scales from intra-building to world-wide. This exponential growth of traffic volume and the demand for ever higher end-user data rates are expected to continue in the foreseeable future. Optical fiber communication technology has kept up with the growing traffic volume by expanding the use of Wavelength Division Multiplexing (WDM) technology, which allows multiple data channels at different optical wavelengths to be transmitted simultaneously over a single optical fiber.

While the growth of the backbone communication capacity has been tremendous, end-user access to this capacity is still expensive and limited to data rate of kilobits and megabits per second. Many research groups are exploring ways to extend high-data-rate capability from the backbone to the user. The use of WDM technology in such metropolitan area access networks is a powerful approach that is currently being actively explored. The challenge is developing the physical architecture of the metro WDM network is to provide intelligent network functionality at the optical layer. Optical switching, among others, is the key enabler for intelligent metro WDM. It allows network traffic switched at optical lambda lever without converting into electrical

domain, which will largely increase the traffic speed and capacity, eliminate network latency and provide networking scalability, flexibility, and transparency, etc.

To meet this tremendous demand, in this thesis, a non latching Micro-optical-electro-mechanical System (MOEMS) 2 x 2 optical switch successfully designed by using Microeletromechanical System (MEMS) technology. The basic structures of MOEMS 2 x 2 switch includes a micro-mirror, which re-directs the optical signal path from a pair of input channels to the desired output channels, and an electrostatic comb drive actuator, which drives the mirror in and out of optical path to realize the switching. The two pairs of fibers are inserted into four built-in pre-alignment grooves for launching and receiving optical signals. Several technical obstacles have been overcome encompassing: designing an actuator with large displacement (>50 μm) and yet maintaining a durable mechanical structures by using coupled-filed ROM simulation as analysis and optimization tool; developing a fabrication process that can ensure a high optical quality mirror fabrication, i.e. smooth surface and vertical profile; and, designing a new signal launching and receiving technique that can bring in the simplicity of the assembly and yet retain a high optical signal propagation quality.

The ANSYS Finite Element Model (FEM) simulation tools have been employed to analyze the electrostatic comb drive actuator design and optimization. The optimized actuator has a folded beam suspension structure with 3 μm beam width and 790 μm

beam length. The supported beams demonstrate a durable mechanical structure and stable driving motion. When the actuator is driven by a pulse generator at a frequency of 3 kHz, there is no mechanical damage, fatigue or stickiness observed. The coupled-field simulation shows a consistent result with the experimental measurements, and thus narrows the initial design span to reduce the development cycle time.

The mirror fabricated with modified Bosch deep dry etching process has a surface roughness of 20 nm and vertical profile of 90 ° ± 0.1°. The fabrication sequence features one-step etching for mirror, actuator and alignment grooves, which ensures an optimized optical alignment and the processing simplicity and thus drastically improve the wafer yield and performance reliability. With the developed deep ICP dry etching, a high aspect ratio of 1: 25 is achieved with very well controlled etching parameters, such as, etching rate, undercutting, micro-loading effect, etc. Both double coating technique and protection walls, introduced in this thesis, contribute to this outstanding result.

One of the most challenging aspects of new photonic device designs involves efficiently coupling single-mode fibers to the devices. Conventional beam expansion approaches that use spherical, GRIN, or cylindrical lenses, or combinations of these lenses, are often not suitable for demanding applications such as MOEMS switches or laser diodes. In this thesis, a tapered fiber with hemispherical end (TH) approach has also been developed that results in high coupling efficiency and low coupling loss, while

providing good reproducibility and ease of fabrication. For MOEMS switches, the TH fiber approach can satisfy important requirements, such as:

- High coupling efficiency
- Low coupling loss
- Good return loss
- Large misalignment tolerant

Also, optimal separation (i.e. distance between the launching and receiving fibers where the coupling loss is a minimum) has to be in a workable range for assembly. In the case of MOEMS switch, this ranges from 80 microns to 120 microns. Shorter distances will be difficult for assembly and can easily damage the lens and mirror, while longer distances will cause additional insertion loss and material waste. In addition, the beam diameter created by TH fiber can be smaller than 30 μm to ensure that there is no light scattering and crosstalk, due to light striking the edge of the mirror or passing over it. Finally, the TH fiber is tolerant to misalignment during the assembly process.

TH fiber fabrication, control, and reproducibility has been discussed. Also, light propagation and beam profile (light intensity distribution) has been investigated with experimental results and simulations reported. Measurements of coupling loss with different TH fibers will be discussed. Additionally, alignment tolerance issues with TH

fibers are studied and some comparisons are made. Using these techniques, fiber alignment, in MOEMS switch assemblies, has been simplified with resulting higher performance and improved characteristics. Varieties of TH fibers, in terms of lens diameter and taper length, have been developed with low coupling loss and good alignment tolerance.

Through this work, the complete FEM analysis with coupled-field simulations by Reduced Order Model (ROM) is able to be achieved to optimize the actuator design and reduce the development cycle. A simplified bulk fabrication processing is developed to accomplish a very simple, highly repeatable and yet compatible with IC processing. The optical quality of the micro-mirror developed by deep dry etch is drastically improved and yet the mirror remains a very vertical profile. A tapered fiber with hemisphere lenses is first employed into optical switch assembly to be well adapted with MEMS optical devices and the optical signal propagation calculation and measurements are also obtained. Finally the fully packaged 2 x 2 optical switch is characterized with low switching speed (1 ms) and excellent optical properties (insertion loss less than 0.7 dB).

Future research directions will be given out in the end for switch performance improvements and also for exploring more applications with various switching configuration based on this 2 x 2 optical switch block.

Total six US and international patents, resulted from this doctoral research project, have been filed in the following:

1) **ZHANG Nan**, *Method of Etching a Wafer Layer Using a Sacrificial Wall and Structure Formed Thereby*, U.S. Patent Application S/N 09/372,700.
2) **ZHANG Nan,** *Microelectromechanical Optical Switch and Method of Manufacture Thereof*, U.S. Patent Application S/N 09/372, 265.
3) **ZHANG Nan**, *Method of Etching a Wafer Layer Using Multiple Layers of the Same Photoresistant Material and Structure Formed Thereby*, S/N 09/372,428.
4) **ZHANG Nan**, *An Efficient, Low Loss Technique for Coupling Fibers to Photonic Devices Thereby*. 2000.
5) **ZHANG Nan,** *Improvement of Switch Output Channel Uniformity by Using On-chip Optical Path Balance Approach Thereby*. 2000.
6) **ZHANG Nan**, *Compact 1x4 Optical Switch Design on Single MEMS chip Thereby*. 2000.

RESUMÉ:

L'explosion actuelle du volume de transmission des données et de l'information est provoquée par un besoin insatiable de connecter les systèmes internets dans une échelle géographique très vaste tant au niveau d'un édifice qu'à l'échelle de la planète. Cet accroissement exponentiel de la transmission des données, les demandes toujours croissantes de la part des utilisateurs vont encore continuer pendant longtemps dans l'avenir. La technologie de communication à l'aide des fibres optiques a bien répondu à ces demandes et changements en augmentant l'utilisation des technologies WDM. Ces dernières permettent de transmettre des données à travers plusieurs canaux à différentes longueurs d'ondes et cette transmission se fait d'une façon simultanée dans une même fibre optique.

Pendant que l' épine dorsale de la capacité de communication a subit une croissance phénoménale; l'utilisation de cette capacité reste encore très dispendieuse et limitée à un taux de transmission de données de l'ordre de kilooctets et mégaoctets par seconde. Beaucoup de groupes de recherche à travers le monde sont en train d'explorer des moyens d'augmenter l'utilisation de la capacité de transmission des données. Ils se posent la question à savoir comment utiliser les résultats de recherche afin de fabriquer des composantes qui aideraient à atteindre cet objectif.

L'utilisation de la technologie des WDM dans un réseau régional métropolitain est une approche très puissante qui est activement explorée actuellement. En développant l'architecture physique du réseau métropolitain WDM, le défi était d'offrir un réseau intelligent fonctionnant avec des couches optiques. Les interrupteurs optiques, parmi tant d'autres, sont à la base de ce qui nous a permis de construire des réseaux métropolitains intelligents WDM. Cela permet au trafic des données en réseau de transformer celles-ci en levier optique lambda sans être converties en signaux électriques; ce qui a pour conséquence; l'augmentation de la vitesse et de la capacité de transmission des données, l'élimination de la lenteur des réseaux et d'obtenir la scalabilité , la flexibilité et la transparence des réseaux etc...

Afin de répondre à ces demandes toujours croissantes, dans cette thèse, nous avons développé un interrupteur 2 x 2 sans verrou à l'aide de la technologie MEMS. La structure de base de l'interrupteur MOEMS 2 x 2 se compose de :

- micro-miroir, qui réoriente le signal optique à partir de deux canaux d'entrée jusqu'aux canaux de sortie.
- Un collecteur électrostatique muni d'actuateur mobile, qui gouverne le miroir à l'intérieur et à l'extérieur de la piste optique afin de réaliser l'interruption.

Les deux fibres sont insérées à l'intérieur des quatre pistes préalignées avec des émetteurs et des récepteurs du signal optique. Nous avons résolu beaucoup de

problèmes et franchi beaucoup d'obstacles techniques; nous pouvons mentionner quelques unes :

- Dessiner la structure d'un actuateur mobile avec un grand déplacement (> 50µm.) et toujours maintenir une structure mécanique durable en utilisant la simulation du champ couple électrostatique comme outil d'analyse et d'optimisation;
- Développer les procédures de fabrication qui peuvent assurer la production des miroirs optiques de grande qualité, c'est à dire une surface lisse et un profil vertical, et développer une nouvelle technique d'émission et de réception de signaux optiques qui peut combiner la simplicité de l'assemblage et encore garder les qualités supérieures de propagation du signal optique.

Afin d'analyser le design et l'optimisation du collecteur électrostatique avec un actuateur mobile; nous avons utilisé l'instrument de simulation ANSY FEM. L'actuateur mobile optimisé a une structure de rayons effilés en suspension avec une largeur de 3 µm. une longueur de 790 µm. Les rayons supportés démontrent une structure mécanique durable et un mouvement de déplacement stable. Quand l'actuateur mobile est mis en mouvement par une pulsion du générateur à une fréquence de 3 Khz, et nous n'avons pas observé de dommage mécanique, ni de fatigue, ni de viscosité.

La simulation du champ couple a donné des résultats consistants avec les mesures des données expérimentales, ainsi nous avons diminué les événements aléatoires qui peuvent se dérouler pendant le développement des schémas et réduit du même coup le temps du cycle de développement.

Le miroir fabriqué avec le procédé de marquage Bosch Trench nous permet d'atteindre une rugosité de 15 nm (20 nm typique) et un profil vertical de $90^{\circ} \pm 0.1^{0}$. La séquence de fabrication présente une étape de marquage pour le miroir, l' actuateur ainsi que l'alignement des pistes ; ceci assure un alignement optique optimisé et nous permet d'obtenir un procédé simple et d'améliorer d'une façon très significative le '' wafer yield '' et la fiabilité des performances.

Avec le développement d'un procédé de marquage DEEP ICP; nous avons obtenu un rapport très élevé d'aspect soit 1 :25 , ayant un profil de marquage très bien contrôlé, comme par exemple; le taux de marquage, le coupage, l'effet de micro-chargement etc.. Les deux techniques; soit la couverture et la protection des murs; introduites dans cette thèse a contribué a atteindre ces résultats.

Le défi le plus grand dans le design des appareils photoniques réside dans le fait qu'il faut mettre en couple des fibres qui sont en mode simple avec d'autres appareils. Les approches conventionnelles de l'expansion des rayons qui utilisent le GRIN

sphériques ou les lentilles cylindriques ou la combinaison de ces deux lentilles, ne sont pas souvent appropriées pour des applications comme les interrupteurs optiques MOEMS ou des diodes au laser.

Dans cette thèse, une fibre effilée dont l'autre bout est hémisphérique (TH) a été développée, ce qui résultent en une efficacité d'accouplement très élevée, et des pertes d'accouplement moindre, cela permet aussi d'obtenir une très grande reproductibilité et une facilité de fabrication.

Pour les interrupteurs optiques MEMS, l'approche de la fibre TH peut satisfaire à des demandes très importantes; par exemple:

- Une très haute efficacité d'accouplement,
- Une perte négligeable d'accouplement,
- Un bon retour de perte,
- Une tolérance très grande aux désalignement.

Nous avons aussi un écartement optimal; (C'est à dire la distance entre l'émetteur et le récepteur optique là où les pertes d'accouplement sont minimales.)qui devrait être dans une plage de travail pour l'assemblage. Dans le cas de l'interrupteur MEMS , cette plage se situe entre 80 μm à 120 μm. Les distances plus courtes seront plus difficiles à

atteindre à cause des problèmes que l'on pourrait rencontrer pendant l'assemblage et peut endommager facilement les lentilles et le miroir; pendant que les distances plus longues vont causer des pertes pendants l'insertion et une perte de matériel.

En plus, le diamètre du rayon crée par la fibre TH peut être plus petit que 30µm.. afin de s'assurer qu'il n'y a pas de lumière qui s'éparpille et s'enchevêtre, à cause de l'échauffement des coins du miroir par la lumière ou quand la lumière passe. Finalement, la fibre TH tolère les désalignements pendant les procédés d'assemblage.

La fabrication, le contrôle, la reproductibilité de la fibre TH a été discutée. Nous avons aussi fait la recherche sur la propagation de la lumière et le profil du rayon (la distribution de l'intensité de la lumière) ceci avec les données expérimentales ainsi que les simulations. Les mesures des pertes pendant l'accouplement ont été discutées avec différentes fibres TH. Ensuite, les problèmes de tolérance avec les fibres TH de l'alignement ont été étudiés, nous avons fait certaines comparaisons.

En utilisant ces techniques, l'alignement des fibres, dans les assemblages des interrupteurs MEMS, a été simplifié ce qui a été pour conséquence, d'obtenir des performances élevées et des caractéristiques améliorées. Divers fibres TH, en termes de diamètres de lentilles et de longueur effilée ont été développées avec des pertes d'accouplement minimes et une bonne tolérance aux désalignement.

À travers ce travail, nous avons effectué l'analyse complète du FEM avec des simulations du champ couplé avec ROM peut être atteinte afin d'optimiser le design de l'actuateur et réduire le cycle de développement.

Nous avons développé un procédé de fabrication très simple afin d'accomplir une très simple, et très répétitive expérience compatible avec les procédés IC. La qualité optique du micro-miroir développé par DEEP ICP etc. a été amélioré d'une façon phénoménale et le miroir demeure avec un profil vertical; une fibre effilée avec des lentilles hémisphériques sont pour la première fois utilisées dans l'assemblage d'un interrupteur optique qui sera utilisé pour la première fois et qui sera bien adapté avec un appareil optique MEMS et le calcul de la propagation des signaux optiques et des mesures sont ainsi obtenues. Finalement, l'assemblage complet d'un interrupteur optique est caractérisé par un interrupteur de basse vitesse (1 ms) et des excellentes propriétés optiques (les pertes d'insertion plus petit que 0.7 dB).

Nous avons donné des pistes de recherches à la fin de la thèse afin d'améliorer les performances de l'interrupteur optique ainsi que pour explorer de nouvelles façons de l'appliquer avec différentes configurations d'interrupteurs basés sur des blocs d'interrupteur 2 x 2.

Il résulte du travail contenu dans cette thèse les breverts d'invention suivantes:

1) **ZHANG Nan**, *Method of Etching a Wafer Layer Using a Sacrificial Wall and Structure Formed Thereby*, U.S. Patent Application S/N 09/372,700.
2) **ZHANG Nan,** *Microelectromechanical Optical Switch and Method of Manufacture Thereof*, U.S. Patent Application S/N 09/372, 265.
3) **ZHANG Nan**, *Method of Etching a Wafer Layer Using Multiple Layers of the Same Photoresistant Material and Structure Formed Thereby*, S/N 09/372,428.
4) **ZHANG Nan**, *An Efficient, Low Loss Technique for Coupling Fibers to Photonic Devices Thereby*. 2000.
5) **ZHANG Nan,** *Improvement of Switch Output Channel Uniformity by Using On-chip Optical Path Balance Approach Thereby*. 2000.
6) **ZHANG Nan**, *Compact 1x4 Optical Switch Design on Single MEMS chip Thereby*. 2000.

TABLE OF CONTENTS:

LIST OF FIGURES:

Chapter 1

Chapter 2

Chapter 3

Chapter 4

Chapter 6

LIST OF TABLES:

Chapter 1

Chapter 2

Chapter 3

Chapter 4

Chapter 5

CHAPTER 1: INTRODUCTION

1. OPTICAL SWITCHING TECHNOLOGIES FOR ALL OPTICAL NETWORKING

In the last two decades, there has been an unprecedented demand for increasing communication bandwidth. Present broadband and multimedia services require very much higher transmission and switching speeds compared with the simple services available in the past. Even if optical fibers have been widely deployed during all this time, it is only more recently that Wavelength Division Multiplexing (WDM) has been used to take advantages of the very high bandwidth available in optical fibers[1-5].

Wavelength Division Multiplexing[6] is a technology that uses distinct wavelengths to transmit different signals in a single fiber. This technology has been successfully used to increase the transmission bit rate in Point-to-Point links. However, The transparency offered by optical fiber will lead to the merger of transport and switching functions, which will result in faster and more flexible network capabilities. Optical switch fabrics are key enablers of this intelligent networking. The capabilities of such devices will greatly enhance system performance and functionality over the current Point-to-Point systems. The optical

transparency of a guided-wave network allows flexible transport and routing of signals between different network endpoints.

Optical cross-connect systems, one of the major applications for optical switches, simplify provisioning and operations by allowing networking at the optical layer[7]. In other words, the Point-to--Point WDM transmission technique means that the entire capacity of each optical fiber should be electrically processed at every node. For example, asynchronous transfer mode (ATM) cells or IP packets are processed at every node in a store-and-forward fashion. Therefore, electrical processing will become the bottleneck resisting node and network capacity expansion. To avoid this problem, all optical networking (AON) will use direct optical connections without electrical routing processing, which provides abundant transmission capacity with large throughput optical nodes. All optical networking solution becomes even more compelling to metro WDM, which can drastically ease the bandwidth bottleneck between broadband access and high-speed long haul. Figure 1.1 is an example of all optical networking architecture[8].

The main AON components, besides WDM line terminals, and optical cross-connects (OXCs), are optical add/drop multiplexers (OADMs)[9], which also consist of optical switch fabrics. OADMs (Figure 1.2) can route the various WDM channels at every node in the network. In its simplest version, such a multiplexer is a four port device consisting of an entering input fiber, an exiting through-fiber, a drop-fiber for removing data streams, and an add-fiber for inserting data. In a WDM system, each

data channel is a different optical wavelength. Each wavelength needs to be routed correctly at each node to either the through-port or drop-port, where data is either accepted or rerouted in a different direction. If a particular wavelength is dropped at a node, it can be reused to transmit a new flow of data. Optical switches realize this re-configurable wavelength routing. In this application, switching speed requires less than 1 ms. Switching must be wavelength and bit rate independent, i.e. transparent, and integratable with other components such as WDM multiplexer, demultiplexer and VOA.

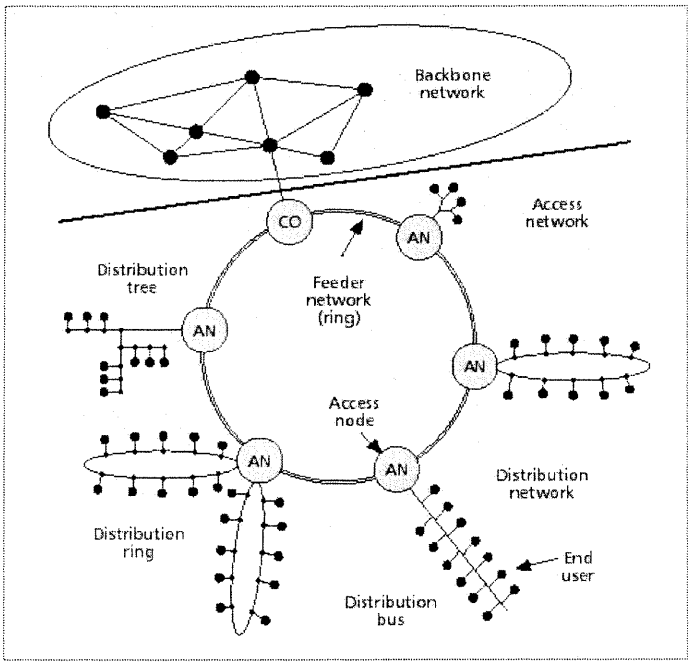

Figure 1.1 Access Network and all optical backbone architecture.

In addition to OXCs and OADMs, another application of optical switches is in provisioning of lightpaths[4]. In this application, the switch fabrics are used inside optical crossconnects to reconfigure them to support new lightpaths. Therefore, the switches are replacements for manual fiber path panels. Thus for this application,

switches with millisecond switching times are acceptable. The challenge here is to realize large switch sizes, that is, the matrix switches. Another important application is that of protection switching[4]. Here the switches are used to switch the traffic stream from a primary fiber on to another fiber in case the primary fiber fails. This application typically requires switching times of the order of a microsecond to a hundred microseconds. Small 2 x 2 switches are usually sufficient for this purpose.

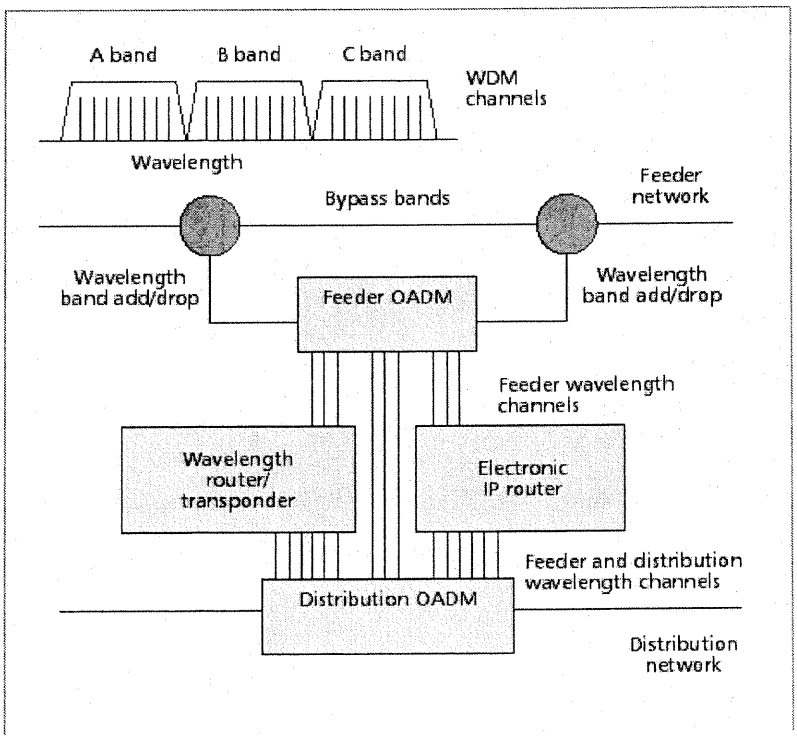

Figure 1.2 OADMs in WDM network.

To meet all optical networking requirements, the optical switch fabrics should feature[10] the fast switching speed, integration with other optical and electronics components, compact design, cost effective/batch fabrication, wavelength and bit rate independence and yet be scalable to large matrix switches or

easily fabricated in switch arrays. However, none of the switching technology in the past could fulfill all the criteria that the future all optical networking is looking for.

Three different evolution stages in telecommunication switching systems can be stated as follows: A first stage concerns mostly present electronic switching fabrics[11]; that is, systems where the lighwave signals coming from fiber optic links are first converted into the electronic domain, then, all the multiplexing and routing function are performed; and finally, the resulted electronic output signals are reconverted to the photonic domain and coupled to the output fibers. A second evolutive stage refers to the photonic transmission and switching functions, but still controlled by electric circuits. The switching technique in this category is the current research and development focus for optical networking. Those switching technologies include, the optical mechanical switches, LN electro-optical switches[12-14], Polymer thermo-optical switch[15], Silica thermo-optical switch[16-17], Semiconductor amplifier (SOA) switch[18], liquid crystal switch[19], etc. Table 1.1 lists those technologies and summarizes the basic performances for each technology. A third approach is constituted by all optical switching devices, that are the components where light is controlled by light[20].

A perspective can be reached after reviewing Table 1.1, that the current switching technology is not suitable for future all optical networking application, largely due to lack of scalability, labor intensity from the optical alignment and assembly and thus very costly, not integratable with other electric and optical

devices, etc. Cost effective solution becomes extremely important for the realization of metro WDM and fiber to home (FTHH) implementation. Therefore, all optical networking requires that new switching technologies come into play to keep up with rather rapid growth of internet traffic and bandwidth demands.

Table 1 Various switching technology comparison.

Type	Loss	Speed	Scalability	Cost	Integration
Mechanical	Low	Slow	Not Good	High	No
$LiNbO_3$	Medium	Fast	Not Good	High	No
SOA	High	Fast	Not Good	High	No
Polymer	High	Medium	Limited	Medium	No
Silica	High	Medium	Limited	Medium	No
Liquid Crystal	Medium	Medium	Not Good	High	No

2. MICROELECTROMECHANICAL SYSTEM (MEMS) TECHNOLOGY

Microelectromechanical system (MEMS) is penetrating an increasing number of technologies[21-22]. In areas as diverse as chemistry, wireless communications, acoustics, data storage, imaging, automobiles, inertial navigation, and now fiber optic communications. Scientists and engineers are building devices with potential to radically alter their industries.

MEMS research grew out of the vast capabilities developed by the semiconductor industry[23-25], including deposition, etching, photolithography, and an array of chemical processes, such as those using highly selective etching chemicals that have different etch rates for different crystallographic orientations and materials. These processes, which researchers originally developed to build microelectronic devices, also enable the creation of micromechanical devices, that is, structures capable of motion on a microscopic scale. There are two basic technologies that are used in MEMS processing, that is, surface micromachining and bulk micromachining. Surface micromachining is to deposit multiple layers on the substrate and then selectively remove some of the layer materials, which leaves a device with movable elements. Bulk micromachining is using deep etching to etch away part of the silicon materials from the substrate to create the designed device.

MEMS devices offer a number of advantages to designers. They are made using integrated circuit (IC) batch-processing techniques, so although fabrication may be a complicated, multistep process, the devices are economical to produce because many are made simultaneously. In addition, designers and manufacturers can exploit the extensive capabilities of the IC-fabrication industry and can profitably use previous-generation equipment. When a billion-dollar IC factory becomes obsolete in less than five years, the ability to reuse equipment for a new class of cutting-edge products is compelling.

IC-fabrication techniques also allow designers to integrate micromechanical, analog, and digital microelectronic devices on the same chip, producing multifunctional integrated systems. Contrary to intuition, MEMS devices have proven to be robust and long-lived. Research in this area during the last decade has yielded microscopic versions of most macromachines. In particular, the size scale at which these machine work makes them a particularly good match to optics problems, where devices, structures, and relevant wavelengths range in size from one to several hundred micrometers.

Therefore, the rapidly expanding demand for high network capacity and unrelenting pressure to reduce costs have made optical MEMS, micro optical electromechanical system (MOEMS), an extremely active area of research and development[26]. Optical MOEMS research focus on devices such as optical modulators, micromirrors, and arrays of tilting micromirrors. However, perhaps the single most powerful device built there is an optical switch. The MEMS switch fabrics allow the building of a wide variety of devices and systems. These include wavelength add-drop multiplexers, positioning switches, optically powered remote nodes, power limiters, variable attenuators[27], and WDM signal equalizers used to maintain the strength of the signal. The optical switch offers a single building block that enables optical scientists to take a modular approach to building complex systems from simple, well-understood elements.

Other potential technology advantages offered by MEMS optical switches compared to the previous available technology (Table 1.1) are: low cross talk, polarization and wavelength independence, and low-power consumption.

3. 2 x 2 MOEMS OPTICAL SWITCH FABRICS

Optical switch fabrics have varying types of configurations. A 2 x 2 switch is the basic building block for many of those matrix switch configurations. Figure 1.3 represents one matrix switch example, in which a 4 x 4 matrix switch fabric is composed of six 2 x 2 switch elements. Besides the role as basic element for matrix switch configurations, 2 x 2 switch can be largely deployed in network multiple line

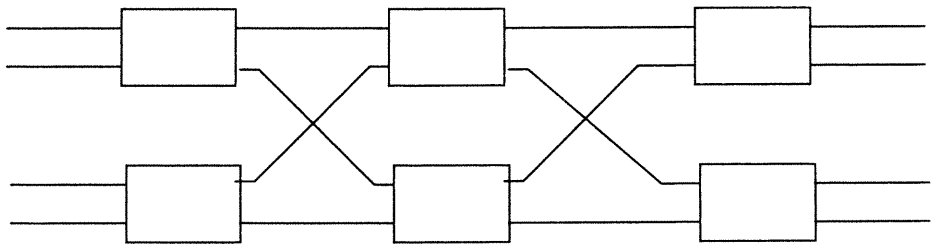

Figure 1.3 An example of the matrix switch fabric consisting of 2x2 elements.

protection and restoration, as well as the optical add/drop modules (OADMs) applications. MOEMS 2 x 2 switch is particular attractive to many researchers mainly because it offers cost effective solution, reliable performance, compact size,

scalable to large matrix switch fabrics or switch arrays and integration with other components. None of the previous switching technologies can really have all those critical features on which all optical networking is keen.

MOEMS 2 x 2 switches are very promising for AON applications. However, all the currently developed 2 x 2 MEMS optical switches have not been really deployed in the optical network system due to various reasons. Toshiyoshi and Fujita [28], reported a composite device consisting of two parts, that is torsion mirror substrate and an electrode substrate. The system was tested with single mode fibers at 1550 nm collimated by spherical lenses. The main draw back of this approach are, the torsion beam could present fatigue and the usage of ball lens with two separate substrate structures make it difficult to do optical alignment and assembly. L. S. Huang et al[29] and S. S. Lee et al[30] reported an hybrid 2 x 2 switch with applications in FDDI systems. This device consists of two different modules: a central chip fabricated with surface micromachining containing the reflective mirrors, and a bulk micromachined silicon submount used to passively align the input/output fibers and to place ball lens. Again, it uses the ball lenses and the torsion mirror is hard to maintain a 90 ° angle, which results in additional insertion loss. L.Y.Lin[31-34] et al reported a surface micromachined cross connect that contains a set of lenses to collimate the signals coming from the input optical fibers, an array of mirrors to redirect the signals, and a set of lenses to focus the redirected signals into the output fibers. The mirrors are rotated from horizontal (Off state) to the vertical position (On state) and using springs to return the mirrors to the horizontal position. While the

idea of a low-cost monolithic device is very attractive, the present status of micromachining technologies still imposes a limit to the coupling efficiency. In this design, binary-amplitude Fresnel lens were used considering their fabrication was compatible with the surface micromachining technology selected, however these components presented a limited transmission efficiency, plus the required special processes are difficult to incorporate with other component in a single chip. H. Toshiyoshi, D. Miyaichi and H. Fujita[35] reported an optical switch with electromagnetic actuation. A magnetic field produced by an electromagnet (ferrite core and cooper wire) is used to rotate the mirror form horizontal to the vertical position. However, the variations in mirror angle from a perfectly vertical position as well as poor mirror flatness make it impossible to use single mode fibers. W. H. Juan et al[36] reported high-aspect ratio mirrors fabricated with Deep Etching and Shallow Diffusion (DESD), with only 30 μm actuator displacement and 50 μm thick mirror. The mirror, however, can not catch all the beams due to the mirror array layout and the limited mirror size. Marxer et al[37-38], reported a 2 x 2 switch fabricated in a Silicon-on-insulator (SOI) wafer by Deep Reactive Ion Etch (DRIE); this approach allows fabrication of a mirror, an actuator and alignment grooves with the same mask, and is very attractive for potential integration with other components. However, they partially removed the fiber tip to bring fiber close to each other to reduce the insertion loss, which will result in alignment difficulties. Moreover, the use of two combs drives in opposite direction results in the inappropriate switching functionality, that is, when power is off, the mirror is half blocking the signals, which is absolutely undesirable. The maximum displacement of designed actuator is

30 μm. Surface roughness is larger than 34 μm and the mirror verticality is only 89-°. Probably the first 2x2 MOEMS switch was developed by N. Riza and D. Polla with PZT actuator[39,40] by surface micromachining, which is constructed with 22 PZT bars. The technology is very interesting because PZT actuator has potential to travel very long distance, however, the chip dimension is very large and driving voltage required is very high.

In a word, many technical challenges still remain unsolved and many researches still need to be explored in MOEMS switch. Firstly, none of the MOEMS switches can really be employed into networks due to optical alignment difficulties which result in large insertion loss [33, 34, 36], due to the inappropriate designs that block the optical signal while power is off[38], or, due to reliability issues introduced by surface micromachining. Secondly, the coupled fields Finite Element Model (FEM) analysis have not been implemented into the MOEMS device design to reduce the development cycle and to optimize the design parameters. Thirdly, the optical interface becomes more and more crucial to improve the switch performance and to reduce cost. However, none of the conventional collimators and ball/micro-lenses can really provide a good solution due to the mismatch of dimensions with MEMS devices or due to the difficulties of on-chip assembly.

Therefore, how to design and develop a novel MOEMS 2 x 2 switch[41] aiming at solving above existing issues is the focus of this work. In this thesis a non-latching 2 x 2 switch is successfully designed by using MOEMS technology. Its basic

structures (Figure 1.4) include a micro-mirror, an electrostatic comb driver actuator, and four launching and receiving fibers. Those elements are all integrated on a single silicon chip. The micro mirror will re-direct the optical signal path from a pair of input channels to the desired output channels, and the electrostatic actuator will drive the mirror in and out of optical path to realize the switching. The fibers are inserted into four built-in pre-alignment grooves to launch and receive optical signals. The main challenges of this project can be described as follows. First is to design an actuator that travels over 50 μm at an IC compatible voltage (less than 100 Volt) and yet maintains a durable mechanical structure aided by coupled-field electrostatic simulation. Second is to develop MEMS processing that can ensure a micro mirror fabricated with high optical quality, which means smooth surface and vertical profile. Third is to design a novel signal launching and receiving technique that can increase the simplicity of the assembly and yet retain a high optical signal propagation quality (low coupling loss).

Through this work, the complete FEM analysis with coupled-field simulations by Reduced Order of Model (ROM) will be used to optimize the actuator design and to reduce the development cycle. A simplified bulk micromachining technique will be developed to accomplish a high repeatable and high yield switch fabrication that is compatible with IC processing. A micro mirror will be fabricated by Deep ICP etching. A tapered fiber with hemisphere lenses will be first employed into optical switch assembly to be well adapted with MEMS optical devices. At last, a fully packaged 2 x 2 MEMS switch will be tested and characterized.

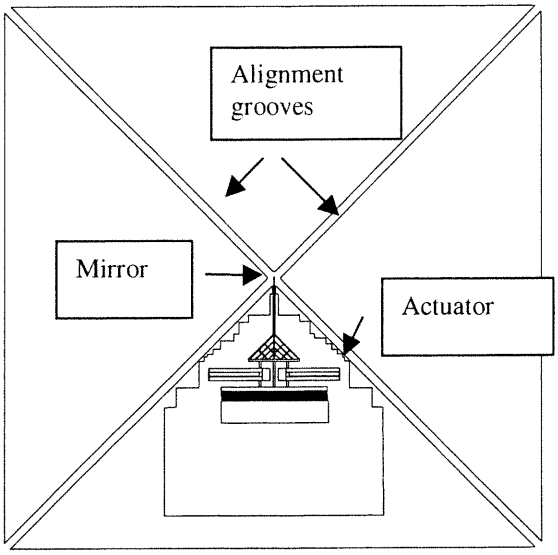

Figure 1.4 2 x 2 MEMS optical switch schematic layout.

4. DISSERTATION OUTLINES

The goal of this thesis is using MEMS technology to design, develop and fabricate a truly functional optical MOEMS 2 x 2 switch fabric. This switch should feature low insertion loss, fast switching speed, compact, wavelength and bit rate transparent, and have the potential for scalable to high level matrix switches, also, be integratable with electronic circuits and other optical components. This switch will be targeted to be largely implemented in optical network protection and restoration systems, and most importantly, be deployed in metro WDM OADMs.

The finite-element simulations on structural static behavior of the suspension spring, dynamic analysis of the comb drive actuator and transient mode analysis are

first presented in chapter 2, as well as the actuator design considerations. In chapter 3, the bulk-micromachining techniques employed in this research are then described with extended experiments on the deep ICP etching technique. The chip level characterizations, including surface roughness measurements and actuation testing, are then carried out and evaluated, followed by the in-depth studies on tapered fibers with hemisphere (TH fiber) lens as signal launching and receiving channels in chapter 4. Comparison of experimental results on light propagation both in free space and the tapered region with theories on the mode field profile of Gaussian beams is also made in this chapter. In chapter 5, the fabricated chip is assembled with the TH fibers in an active optical alignment system, and then the whole device is packaged with hermetic sealing technique, followed by device performance testing and reviews. Finally, in the last chapter, a discussion on successful development and remaining issues of MOEMS switch leads to a conclusion on its wide applications for AON, and a consideration on potential future researches.

REFERENCES:

1 **Dutta, R., Rouskas, G.N.**, *A Survey of Virtual Topology Design Algorithms for Wavelength Routed Optical Networks*, Optical Networks, (2000), 1 (1), 73-88.

2 **Hoanca, B., Dubovitsky, S.,** *All-Optical Routing Using Wavelength Recongnizing Switches,* J. Lightwave Technology, (1998), 16(12), 2254.

3 **Elmirghani, M.H.,** *All-Optical Wavelength Conversion: Technologies and Applications in DWDM Networks*, IEEE J. Communications, (2000), 3, 1-9.

4 **Ramaswami R., Sivarajan, K.,** *Optical Networks: A Practical Perspective, San Francisco*: Morgan Kaufman, 1998.

5 **Ramaswami R., Sivarajan, K.**, *Routing and Wavelength Assignment in All-Optical Networks*, IEEE/ACM Trans, Net., (1995), **3 (5),** 489-500.

6 **Silvalingam, K, M.,** *Optical WDM Networks - Principles and Practice,* March, 2000.

7 **Ghani, N., Dixit, S., Wang, T.,** *On IP-over-WDM Integration*, IEEE J. Communications, (2000), **3**, 13-26.

8 **O'Connell, D.,** *Carries Banking on Optical Infrastructure,* Telecommunicaitons, (2000), **6**, S3-S5.

9 **Ware, A., Lacey, J.,** *Optical Switches in the Next-Generation Transport Network*, Telecommunications, (2000), **6**, S8-S12.

10 **Thylen, L., Karlsson, G., Nilsson, O.**, *Switching Technology for Future Guided Wave Optical Networks: Communication*, Academic Press, 1998.

11 **CIR,** *Optical Switching Bazzar,* Optical Watch, (2000), **3**, 1-3.

12 **Okayama, H. Kawahara, M.**, Low-Crosstalk 2x2 Digital Optical Switch, Electronics Letters, (1994), **30 (5),** 403-405.

13 **Granestand, P.**, *Integrated Optics 4x4 Switch Matrix with Digital Optical Switches*, Electronics Letters, (1990), **26 (1),** 4-5.

14 **Granestrand, P.,** *Strictly Non-blocking 8x8 Integrated Optical Switch Matrix in Ti: $LiNbO_3$*, Topical Meeting on Integrated and Guided Wave Optics, Opt. Soc. Am., 1986.

15 **Keil, N., Yao, H.H., Zawadzki, C.,** *2x2 Digital Optical Switch Realised by Low Cost Polymer Waveguide Technology,* Electronics Letters, (1990), **32 (16),** 1470-1471.

16 **Okuno, M., Kato, K., Nagase, A.**, *Silica-Based 8x8 Optical Matrix Switch Integarting New Switching Units with Large Fabrication Tolerance*, IEEE J. Lightwave Technology, (1999), **17 (5),** 771-781.

17 **Nagase, R.**, *Silica-Based 8x8 Optical Matrix Switch Module with Hybrid Integrated Driving Circuits and its System Application*, J. Lightwave Technology, (1994), **12 (9),** 1631-1639.

18 **Davies, D.A.O., Fisher, M.A.**, *Integrated Lossless InGaAsP/InP 1-to-4 Optical Switch,* IEEE J. Quantum Electronics, 1994, **30 (3),** 717-723.

19 **Huang Y.T.**, *Polarization-Independent Optical Switch Composed of Holographic Optical Elements*, Optical Letters, (1995), **20 (10),** 1198-1200.

20 **Wagner, R.,** *Multiwavelength Lightwave Networks*, OFC'2000 Short Course, Maltimore, Maryland, 2000.

21 **Hiroyyuki, F., Hiroshi, T.,** *Micro Actuators and Their Applications*,

Mircoelectronics Journal, (1998), **29,** 637-640.

22 **Marchall, S.**, *New Applications Emerging as MEMS Technology Advances*, R&D Magazine, (1998), 32-37.

23 **Gardner, J.W.**, *Microsensors: Principles and Applications*, John Wiley & Sons, New York, 1995.

24 **Sze, S. M.,** *Semiconductor Sensors*, John Wiley & Sons, New York, 1994.

25 **Campbell, S. A.,** *The Science and Engineering of Microelectronic Fabrication*, Oxford University Press, New York, 1996.

26 **Wu, M.C.,** *Micromachining for Optical and Optoelectronics Systems*, Proceedings of the IEEE, (1997), **85 (11),** 1833-1856.

27 **Gile, C.R., Aksyuk, V., Barber, R.**, *A Silicon MEMS Optical Switch Attenuator and Its Use in Lightwave Subsystems* IEEE J Selected Quantum Electronics, (1999), **5(1),** 18-25.

28 **Toshiyoshi, H., Fujita, H.,** *Electrostatic Micro Torsion Mirrors for an Optical Switch Matrix,* Journal of MEMS, (1996), **5 (4),** 231-237.

29 **Huang, L.S., Lee, S.S. Motamedi, E., Wu, C.**, *Optical Coupling Analysis and Vibration Characterization for Packaging of 2x2 MEMS Vertical Torsion Mirror Switches,* Proceedings of SPIE, (1998), **3513,** 135-143.

30 **Lee, S.S., Huang, L.S.,** *Free-Space Micromachined Optical Switches Based on MEMS Vertical Torsion Mirrors,* J Lightwave Technology, (1999), **17(1),** 7-13.

31 **Lin, L.Y., Goldstein, E.L., Tkach, R.W.**, *Free-Space Micromachined Optical Switches with Submillisecond Switching Time for Large-Scale*

Optical Crossconnects, IEEE Photonics Technology Letters, (1998), **10 (4),** 525-527.

32 **Simmons, J.M., Saleh, A.A.M., Goldstein, .LY. Lin,** *Optical Crossconnects of Reduced Complexity for WDM Networks with Bidirectional Symmetry*, IEEE Photonics Technology Letters, , (1998), **10 (10),** 819-821.

33 **Lin, L.Y., Goldstein, E. L., Simmons, J. M., Tkach, R. W.,** *High-Density Micromachined Polygon Optical Crossconnects Exploiting Network Connection-Symmetry,* IEEE Photonics Technology Letters, (1998), **10 (10),** 1425-1427.

34 **Lin, L.Y., Goldstein, E. L., Tkach, R. W.,** *Free-Space Micromachined Optical Switches for Optical Networking,* IEEE J. Selected Topics in Quntum Electronics, (1999), **5 (1),** 4-9.

35 **Toshiyoshi, H., Miyauchi, D., Fujita, H,** *Electromagnetic Torsin Mirrors for Self-aligned Fiber-Optic Crossconnectors by Silicon Micromachining*, IEEE J Selected Topics in Quntum Electronics, (1999), **5 (1),** 10-17.

36 **Juan, W.H., Pang, S.W.**, *Batch-Micromachined, High Aspect Ratio Si Mirror Arrays for Optical Switching applications,* Tech. Dig., Transducers'97, (1997), 93-96.

37 **Marxer, C., Thio, C.,** *Vertical Mirrors Fabricated by Deep Reactive Ion Etching for Fiber-Optics Switching Applicatiosn*, IEEE J. MEMS, (1997), **6(3),** 275-278.

38 **Marxer, C., de Rooij, N.F.,** *Micro-Opto-Mechanical 2x2 Switch for Single-Mode Fibers Based on Plasma-Etched Silicon Mirrros and Electrostatic*

Actuation, J. Lightwave Technolgy, (1999), **17 (1),** 10-17.

39 **Riza, N., Polla, D.**, *Micromechanical Fiber-optic Switch s for Optical Networks*, Integrated Optics and Microstructures, (1992), **SPIE 1793,** 108-126.

39 **Riza, N., Polla, D.**, *Microdynamical Fiber-Optic Switch and Method of Switching Using Same*, US Patent 5208880, (1993).

41 **Zhang, N.,** *Microelectromechanical Optical Switch and Method of Manufacture Thereof*, U.S. Patent Application S/N 09/372, 265.

CHAPTER 2: ACTUATOR DESIGN AND FEM ANALYSIS

1. INTRODUCTION

The actuator is the key element of the optical switching design. The design criteria of an actuator for optical switching operations are underlined in three aspects. First is the larger displacement, in the 2 x 2 switching configuration the displacement must be over 50 microns in order to assure that the mirror is completely retrieved from the optical path. Second is the fast switching speed, which must be less than 10 ms for current networks, however, less than 1 ms switching speed is needed for future high speed WDM ring networks, particularly, the optical add/drop modules (OADMs). Last is the durable mechanical structure, which is the key factor for reliable switching performance.

The electrostatic force is one of the most commonly used actuation principles in many micro-actuators, including continuously rotating motors [1,2] and linear actuators suspended by thin beams [3-6]. Comb-drive actuators, first demonstrated by Tang et al. [3,4], are widely used, since their output force is easily controlled by the applied voltage, and the output force needed to drive passive structures is extracted more easily than in rotational actuators.

The basic structure of the electro-static comb drive designed for this optical switch application is shown in Figure 2.1. It features a single comb driver design with folded beams. A support triangle is attached to the blade (connected to the mirror) to reduce the vibration of the mirror in high-speed motion. The central element of the electrostatic actuator is a comb finger structure. It is essentially a capacitor with variable geometry. The capacitor plates can deform and move relative to each other due to electrostatic, inertia or mechanical forces, resulting in a measurable capacitance change. This change transduces electrical and mechanical energy and provides information about the location of the plates, which will enable switch performance monitoring. By applying an appropriate voltage to the anchors, the gap between the plates can be controlled.

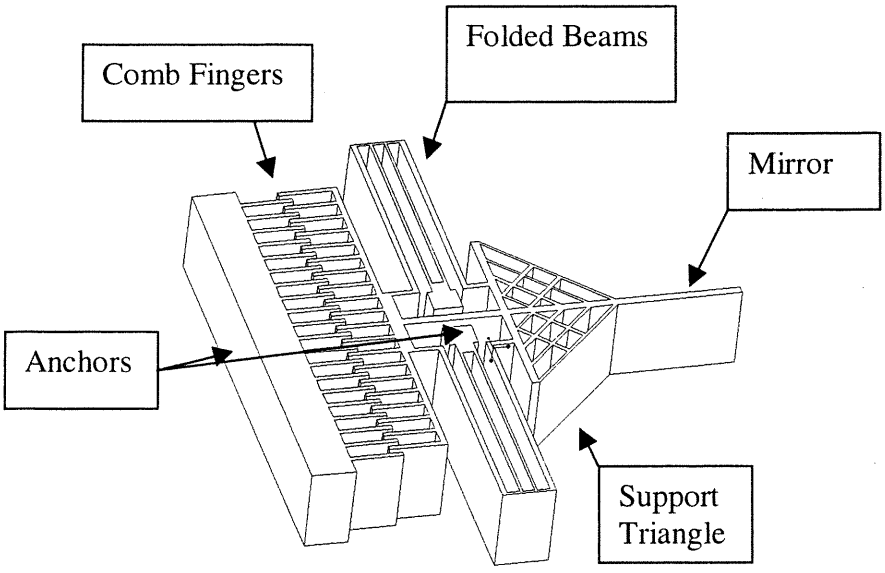

Figure 2.1 Basic structure of an electrostatic comb actuator.

The structural resonant frequency, the driving voltage and the model transient behavior are key parameters for designing the actuator to meet the

switching performance requirements. Therefore, the first and majority part of this chapter contributes to the coupled field Finite Element modeling (FEM) simulations of the comb drive actuator, including static stiffness analysis (spring constant), model analysis (resonant frequency), electrostatic analysis, and coupled-field simulation for transfer function (driving voltage) and model transient behavior analysis. The second part discusses the design parameters, considerations and optimizations based on the summary of ANSYS simulation results. The actuator design datasheet will list the parameters designed after ANSYS simulations.

2. COUPLED FIELD FINITE ELEMENT ANALYSIS BASED ON REDUCED ORDER MODELING

2.1 Introduction

The MEMS simulation involves numerical analyses in diverging areas of physics, such as solid mechanics, electromagnetics, heat transfer, fluid dynamics and acoustics. The interaction between these individual phenomena can be simulated by a coupled field analysis [7]. The coupling can be weak or strong. In a weakly coupled case, the physics domains are analyzed individually and sequentially in an iteration loop where convergence difficulties can occur. In a strongly coupled case, the whole problem is solved simultaneously providing full system eigen frequencies and stability features.

The software tool used for FEM analysis is ANSYS 5.6. The ANSYS finite element (FE) software product line is suited for performing the myriad of physics simulations required for MEMS [8]. Release 5.6 of the ANSYS/Multiphysics program provides accurate, high-fidelity time-harmonic and time-domain solutions in a fast and efficient manner. However, the full 3-D model simulation for coupled field analysis is time consuming and requires huge computer hardware space. Therefore Reduced Order Modeling (ROM) is introduced to offer a simplified solution for coupled field analysis and yet retain a good accuracy [9]. ROM takes on two forms in ANSYS, one consisting of lumped finite elements (spring, mass, damper, transducers, capacitor, inductor, resistor, etc.) and substructuring of large linear systems when reduction to simple lumped elements is not feasible or is cumbersome.

The actuator is composed of a silicon-based substrate with room-temperature properties as shown in Table 2. 1. Those material properties will be implemented in the following ANSYS simulations.

Table 2.1 Material properties for ANSYS simulations.

	Silicon	
E	Elastic modulus	150000 MPa
ν	Poisson's ratio	0.17
ρ	Density	2.33×10^{-15} kg/μm^3
	Air	
ε_0	Permittivity	8.854×10^{-6} pF/μm

2.2 Static Stiffness/Spring Constant Analysis

There are two main design criteria for the suspensions of large amplitude, lateral actuated comb drivers. First, the suspension should provide freedom of travel along the direction of the comb-finger motions (y), and yet restrain the structure from moving sideways (x) to prevent the comb fingers from shorting to the drive electrodes. And thus, the spring constant along the x direction must be much higher than that along the y direction, i.e., $k_x >> k_y$. Second, the suspensions should allow for the relief of the built-in stress of the structural material as well as axial stress induced by large vibrational amplitude.

A folded-beam suspension design fulfills these two criteria. Figure 2.2 is the layout of a folded beam. This design allows large deflection in the y direction (perpendicular to the length of the beams) while providing stiffness in the x direction (along the length of the beams). Furthermore, the only anchor points for the whole structure are near the center, thus allowing the parallel beams to expand or contract in the x direction, relieving most of the built-in and induced stress. The purpose of this section is to obtain the optimal suspension beam design by simulating the beam stiffness with varying structures.

Various loads (force or pressure) are applied on different nodes of the model to test the impact on the stiffness analysis results. Also, various folded beam designs are analyzed to study the relationship between spring constant and beam geometry.

The displacement as a function of forces is finally evaluated, and the minimum force needed to travel over 50 μm is obtained.

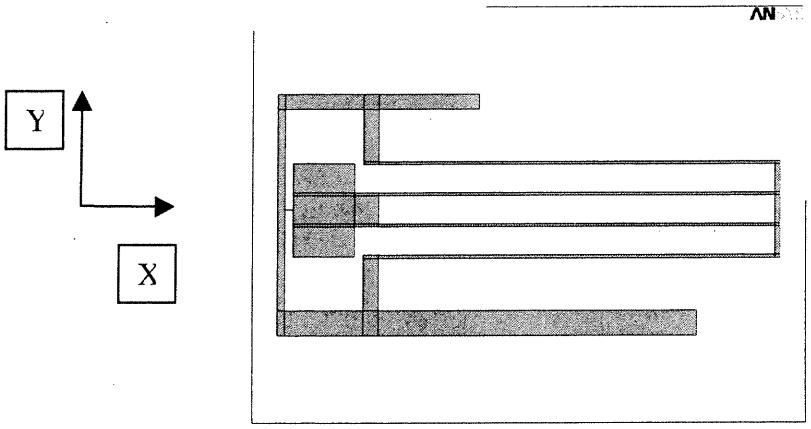

Figure 2.2 Folded beams.

2.2.1 *Loads testing*

A force is first applied on the nodes that are located on the lower "force-adopt" beam (N_1 to N_4), followed by applying a pressure on area 1 (See Figure 2.3) to compare the stiffness simulation outcomes from the loads variations.

As observed from simulation results (Table 2.2), the simulated spring constants stay almost unchanged when the force applied on different nodes, that is, N1 through N4. A 0.04 μN/μm differentiation occurred by loading force vs. pressure on the beam. For the rest of the analysis, force will be loaded on node 1 for

consistent result and comparison. The solide45 (brick 8 nodes) is used as mapped mesh element with set global size of 20 μm (Figure 2.4 meshed structures).

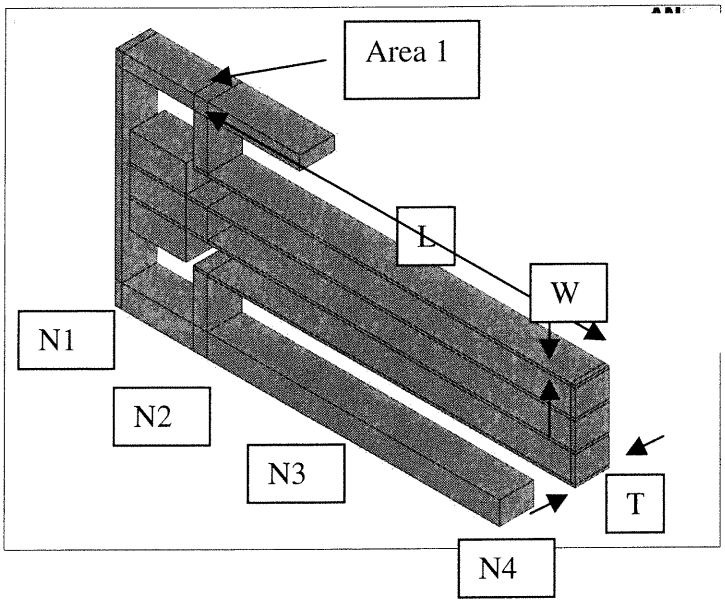

Figure 2.3 Loads testing schematic drawing (L is beam length, W is beam width and T is beam thickness, which is always 75 μm in this design.).

Table 2.2 Loads testing (beam width = 4 μm, beam length = 990 μm).

Loads Type	Nodes/Area	Loads Amount	Displacement	Stiffness
Force	N1	1μN	1.378 μm	0.7257 $\mu N.\mu m^{-1}$
Force	N2	1 μN	1.378 μm	0.7257 $\mu N.\mu m^{-1}$
Force	N3	1 μN	1.388 μm	0.7205 $\mu N.\mu m^{-1}$
Force	N4	1 μN	1.380 μm	0.7246 $\mu N.\mu m^{-1}$
Pressure	S1	1.523 μPa	1.312 μm	0.7621 $\mu N.\mu m^{-1}$

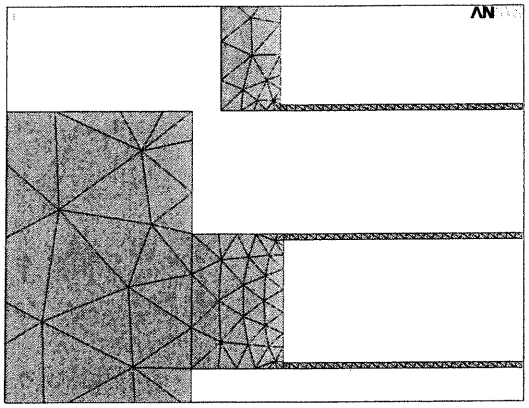

Figure 2.4 Meshed folded beam for stiffness analysis.

The amount of force applied to the beam also influence the spring constant results. An accelerated ramp up curve is observed when the applied force rises from 0.2 μN to 6 μN (Figure 2.5). That introduces a change of 0.024 $\mu N \mu m^{-1}$ in spring constant. After the applied force exceeds 40 μN, the stiffness approaches a constant value of about 0.7254 μN.μm-1. Therefore, in the remaining analysis a force of 40μN is applied to obtain consistent stiffness analysis results.

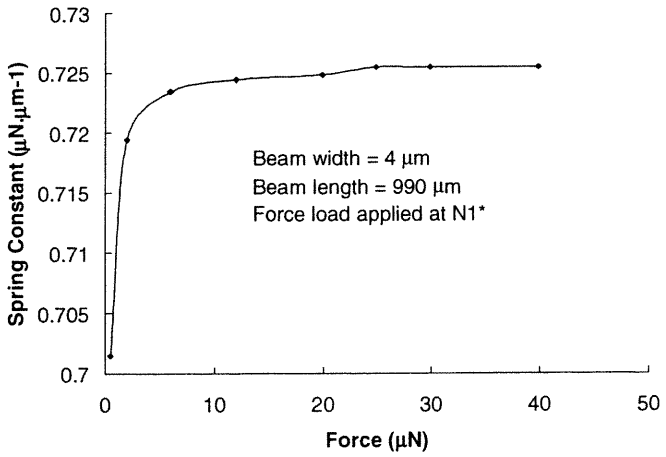

Figure 2.5 Spring constant as a function of loaded force amount.

2.2.2 *Stiffness and beam geometry*

Figure 2.6 shows the stiffness changes with the beam width. For a beam width of 2 μm and 990 μm length, the stiffness is 0.092 $\mu N.\mu m^{-1}$, however, when the beam width increases to 6 μm, the stiffness becomes 2.41 $\mu N.\mu m^{-1}$. Thus, the stiffness is very sensitive to beam width. A narrower beam is favorable for larger displacement at a given driving force. Meanwhile, the stiffness will reduce when the beam length is longer. Taking a beam width of 3 μm as an example, the stiffness is 0.612 $\mu N\mu m^{-1}$ for beam length of 790 μm, and decreases to 0.3 $\mu N\mu m^{-1}$ for beam length of 990 μm.

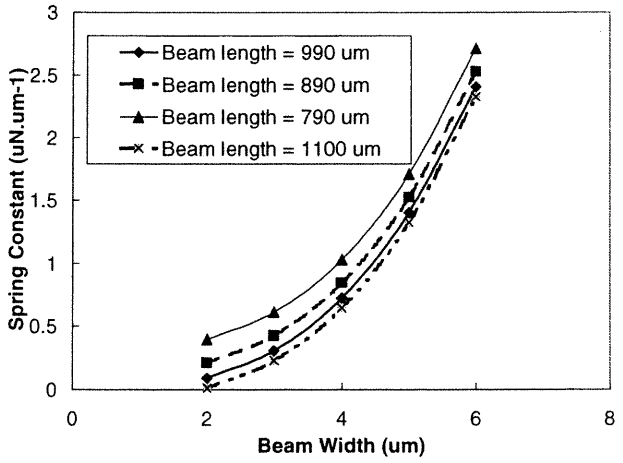

Figure 2.6 Stiffness change with beam widths and lengths.

In addition, stresses introduced by beam deflection also depend on the beam geometry. Figure 2.7 shows the maximum Von Mises[12] stress as a function of the beam width at different beam lengths. Obviously, a wider beam will help to reduce the maximum stresses existing around the corner of the folded beam

when the beam is deflected. A longer beam will increase the Von Mises stresses around the beam corner and thus the beam becomes fragile and breaks during deflections. Figure 2.8 shows the distribution of the Von Misses stress across the folded beam area. The maximum stress happened around the corner of the beam.

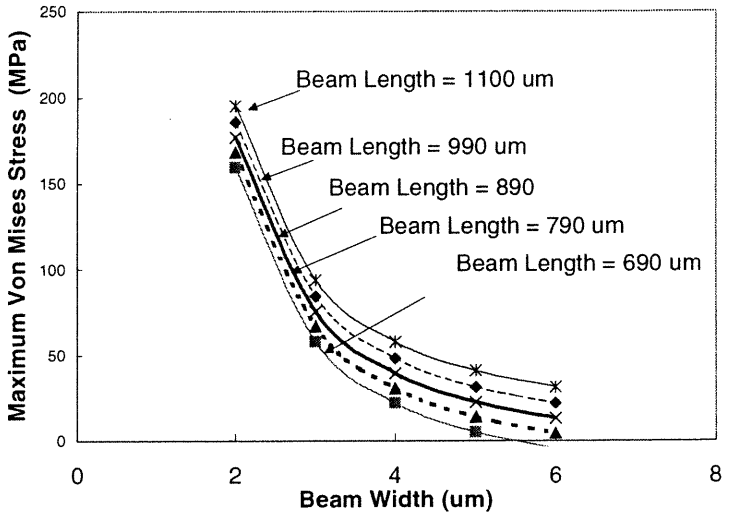

Figure 2.7 Beam Von Misses stress vs. beam widths and lengths.

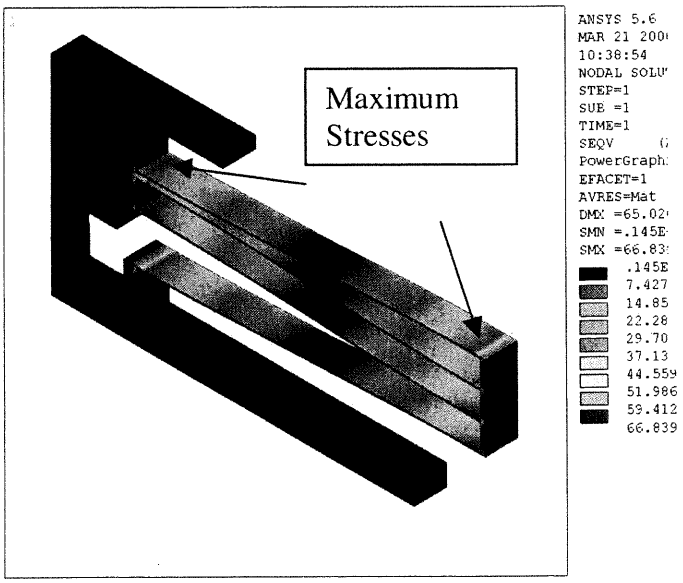

Figure 2.8 Beam Von Mises stress distributions.

To complete the folded beam design, the spring constant ratio along lateral (x) direction and y direction also needs to be evaluated, and that is $k_x/k_y \sim (L/W)^2$. Table 2.3 lists the results of the beam stiffness ratio. The results show that increasing beam width will reduce the ratio of k_x and k_y. Taking beam length of 790 μm as an example, for the beam with width of 2 μm the ratio is 156000, it reduces to 17000 when the beam width increases to 6 μm. A system with high k_x and k_y ratio could offer a more stable motion along y direction without lateral motion. The large lateral motion along x direction might cause electrical short circuit between two electrodes.

Table 2.3 Beam stiffness ratio between k_x and k_y.

Beam Width (um)	2	3	4	5	6
k_x/k_y	156000	69000	39000	25000	17000

2.2.3 *Folded beam design considerations*

As described in the last section, increasing the beam width will lead to increasing beam stiffness along x and y direction. Thus, the ratio of k_x and k_y will remain relatively constant as beam width varies. To achieve over 50 μm displacement, a narrower beam is desired. However, considering manufacturability and fabrication yield, a beam width of 3 μm is the design choice vs. 2 μm. As for beam length, a longer beam will create higher stresses around beam corners (67 MPa

for beam length of 790 μm and 93.48 MPa for 1100 μm beam) and higher aspect ratio of beam dimension, which will cause mechanical failure in the actuator fabrication. Therefore, 790 μm length is chosen even though a longer beam can be good for larger traveling.

Figure 2.9 shows the minimum force needed to realize the displacement of 55 μm along y, that is, 68 μN for a beam with width of 3 μm and length of 790 μm. For this beam design, the spring constant is 1.23 $\mu N\mu m^{-1}$ in x direction and 3.35 $\mu N.\mu m^{-1}$ in y direction, which gives $k_x/k_y=69000$. Table 2.4 for the summary of parameters of the final design simulations.

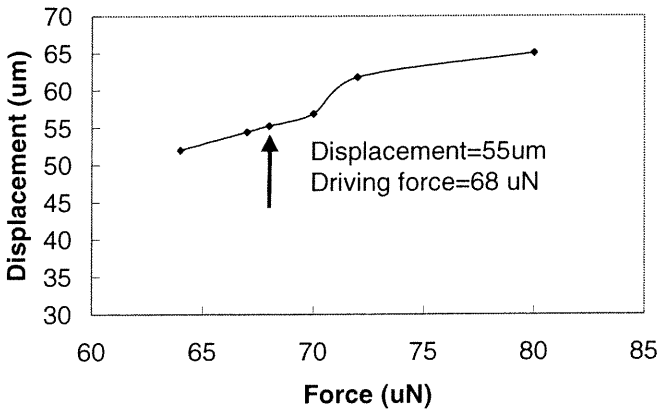

Figure 2.9. Displacement as a function of driving force.

Table 2.4 Simulation parameters for an actuator with folded beam of length=790 μm, width=3 μm.

Spring Constant	Maximum Stress	Force Applied	Displacement
1.23 μN.μm-1	67 MPa	68 μN	55 μm

2.3 Model Analysis

The purpose of the model analysis is to determine the structure's vibration characteristics of natural frequency, mode shapes, mode participation factors (how much a given mode participates in a given direction), and to obtain the effective mass in the displacement direction. The effective mass will later be used as primary input in coupled field ROM simulations.

2.3.1 *No pre-stress and no damping*

Considering a matrix representation of the transient dynamic equations

$$M\ddot{u} + D\dot{u} + Ku = f \tag{2.1}$$

where M, D, and K represent the mass, damping, and stiffness matrices, u is the degree of freedom vector, and f is the forcing function; dot denotes time derivative.

With no pre-stress and no damping model analysis, the damping is ignored and free vibration is assumed, $\{F\{t\}\}=0$, (no pre-stress) and the equation becomes

$$[M]\{\ddot{u}\} + [K]\{u\} = 0 \tag{2.2}$$

The solid model is meshed primarily with solid hexahedral (brick) elements; however, shell elements are used to mesh the individual comb teeth. With combinations of two elements, a total of 15688 elements in this meshed solid model

need to be solved. Figure 2.10 shows the meshed results. Figure 2.10 (a) is the mesh elements on the folded beams. 2.10 (b) is a close look at the shell elements on comb fingers. Figure 2.10 (c) is the mesh area around anchors and the Degree of Freedom (DOF) constrains on the anchor and (d) is the front view of the meshed comb actuator.

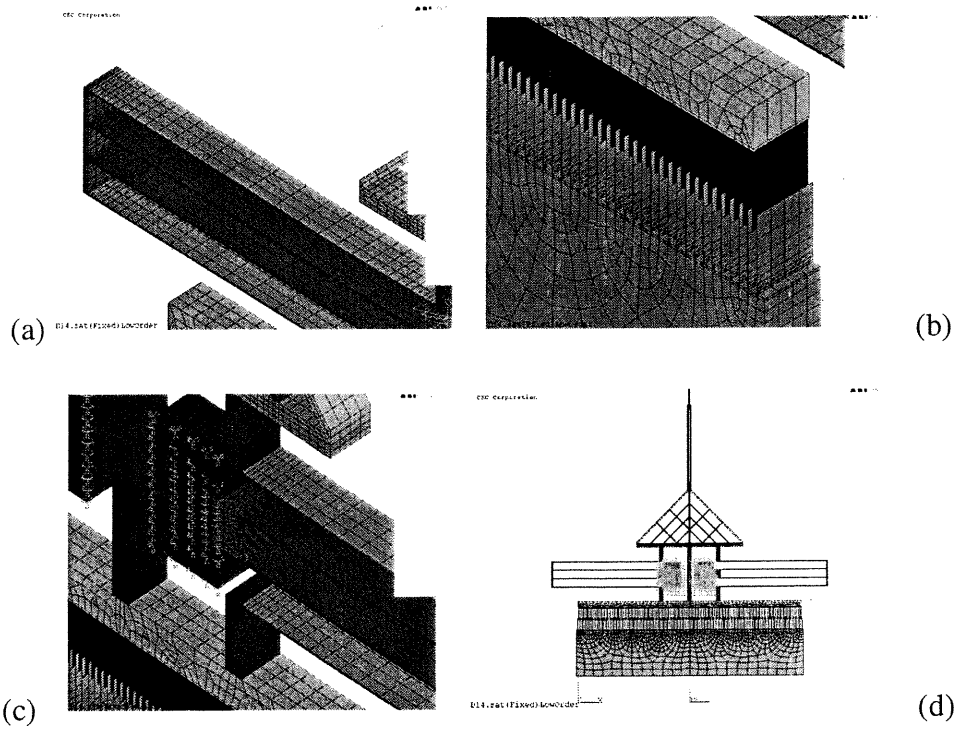

Figure 2.10 Model analysis meshing results. (a) Folded beams (b) Comb fingers (shell elements) (c) Anchors (d) Top view of the whole meshed actuator.

Table 2.5 lists the simulation results for no pre-stress and no damping model analysis. The participation factor calculations are for Y direction, which is the desirable actuation direction. Mode #1 is the desirable mode shape for the actuator. Its y direction ratio is 1, which means the device's sole movement is along y direction with participation factor of 0.2056E-03, and the frequency is 874

Hz. The effective mass is 0.4228E-07 Kg, compared with a structural mass of 0.526E-07 Kg calculated from AutoCAD at density of 233E-17 Kg/μm^{-3}. Figures 2.11 (a)-(d) show selected mode shape animation results. Figure 2.11 (a) is the only one that has movement solely along y direction; in (b) mode the structure moves back and forth along z direction; in (c) mode the folded beam swings up and down, while the rest of the structure has a slight movement along y direction; and in (d) mode the main movement is along x direction (one of the folded beams swings down while another

Table 2.5 Model analysis results under no pre-stress and no damping.

Cumulative Mode	Effective Mass (Kg)	Frequency (Hz)	Participation Factor	Ratio
1	0.4229E-07	874	0.2056E-03	1.000000
2	0.1075E-16	2215	0.3279E-08	0.000016
3	0.1959E-21	7823	0.1399E-10	0.000000
4	0.6994E-09	8138	0.2645E-04	0.128620
5	0.1241E-22	11209	-0.3522E-11	0.000000
6	0.3471E-20	14996	-0.5892E-10	0.000000
7	0.2394E-23	23025	-0.1547E-11	0.000000
8	0.6284 E-25	25912	-0.2507E-12	0.000000
9	0.6168E-23	39560	-0.278E-11	0.000000
10	0.2103E-12	39713	-0.4586E--06	0.002230

Sum of effective masses=0.4324E-07 Kg.

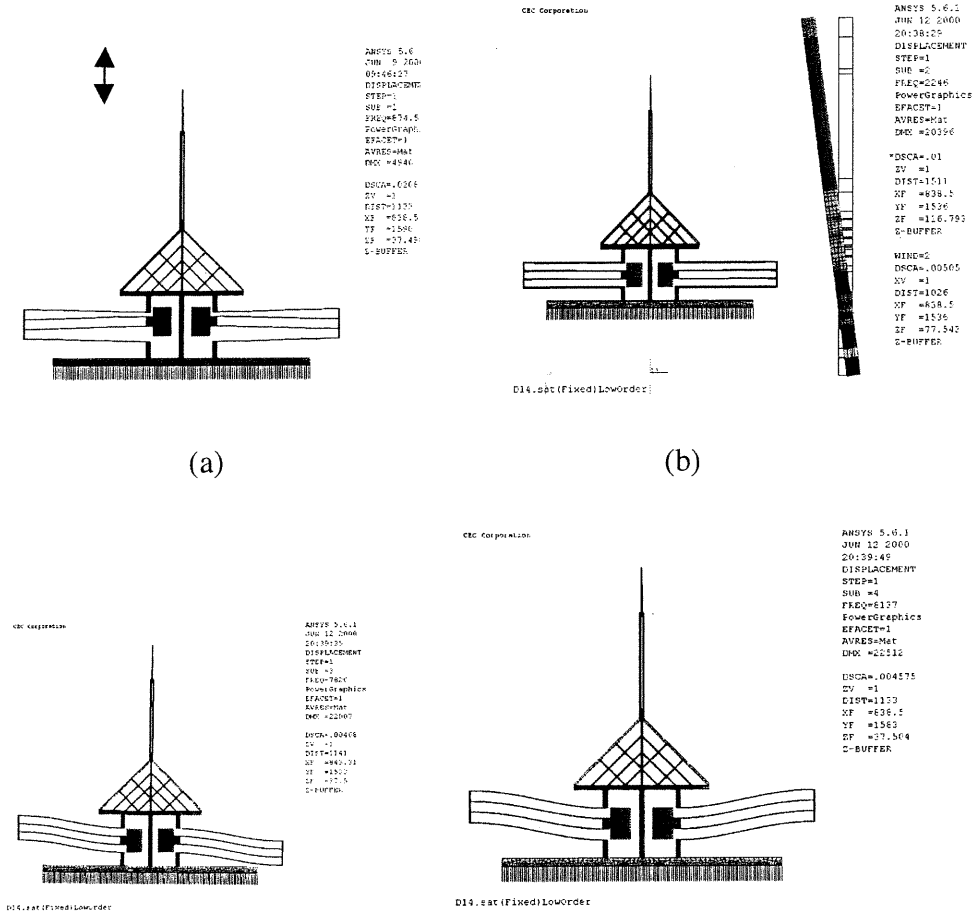

(a) (b)

(c) (d)

Figure 2.11 Examples of mode shape animations. (a) Mode #1: f=874 Hz; (b) Mode #2: f=2245 Hz; (c) Mode #3: f= 7825 Hz; (d) Mode #4: f= 8138 Hz.

one swing up), and the whole structure vibrates in the x, y direction by twisting around two anchors. This is the mode that needs to be avoided from the switching operation since it will create the vibration that drives the mirror away from the center of the optical path. However, the frequency of this mode is about 8138 Hz,

almost ten times of the main mode frequency. Therefore, the chance to activate this mode with the basic mode is very small. The rest of modes are all far away from the dominant mode of 874 Hz, and they will not be discussed in detail.

2.3.2 *Pre-stress but no damping*

There are three main steps involved in this simulation, that is, model generation, pre-stress the model with a static analysis, then model analysis with pre-stress. Pressure of 268 Mpa is applied, and the five modes pre-stressed analysis results are listed in Table 2.6.

Table 2.6 Model analysis results under pre-stress and no damping.

Cumulative Mode	Effective Mass (Kg)	Frequency (Hz)	Participation Factor	Ratio
1	0.42267E-07	874	0.2056E-03	1.000000
2	0.3515E-14	2245	0.5929E-07	0.000288
3	0.1182E-22	7825	-0.3438E-11	0.000000
4	0.7078E-09	8136	0.2660E-04	0.129405
5	0.4214E-22	11221	-0.6492E-11	0.000000

Sum of effective masses=0.4298E-07 Kg.

The results show that the frequency for the first mode is 874Hz compared with 874 Hz for no pre-stress, no damping analysis. However, at high

modes a frequency shift is observed. Taking the tenth mode as an example, a frequency shift of 239 Hz occurred for no pre-stress, no damping analysis (38713 Hz) in comparison to the pre-stressed model analysis (38952 Hz). The frequency shifts 239 Hz higher. The effective mass along Y direction is 0.4227E-07 Kg.

2.3.3 *Pre-stress and damping*

To evaluate the influence of damping on the modes properties, model analysis with pre-stressed and damping is studied. The mass (alpha) damping and stiffness (beta) damping are given in Figure 2.12, of which the combined damping ratio is shown in solid curve. A damping ratio of 0.5% is taken for the damping model analysis as shown in Figure 2.12.

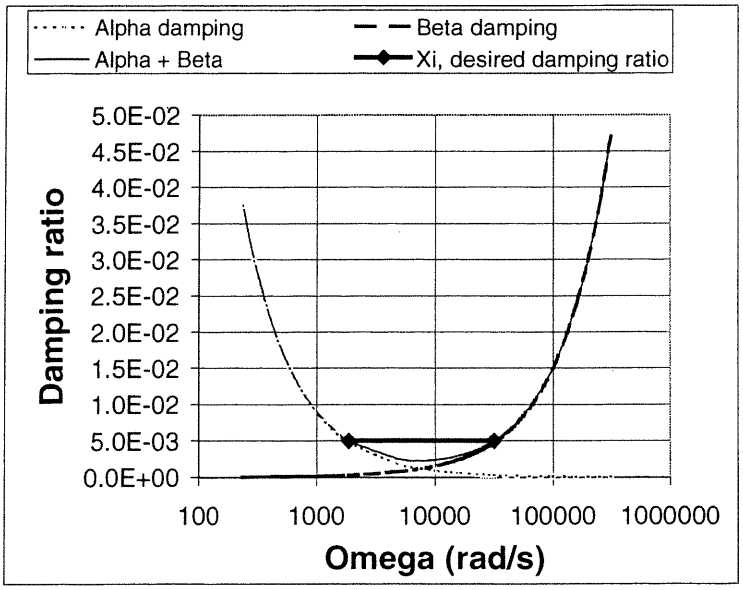

Figure 2.12 Damping coefficient conversion.

The simulation results (Table 2.7) show that introducing the damping ratio results in the frequency shift, again, for high mode, while influences little on low modes, particular the first mode that we are interested in. Therefore, the effective mass along the y direction from no pre-stress and no damping analysis will be taken into the following coupled field analysis.

Table 2.7 Model analysis results for pre-stress with damping ratio of 0.5%.

Mode	Complex	Frequency (Hertz)	Model Damping Ratio
1	-2	874	0.2442E-02
2	-6	2228	0.2735E-02
3	-59	7826	0.7557E-02
4	-63	8139	0.7845E-02
5	-120	11220	0.1070E-02
6	-215	15072	0.1430E-01
7	-501	23020	0.2176E-01
8	-641	26046	0.2460E-01
9	-1476	39533	0.3732E-01
10	-1487	39685	0.3746E-01

2.4 Electrostatic Analysis

The purpose of this section is to design and simulate the electrostatic properties of the comb finger actuator and achieve the relationship between capacitance and strokes, which will be taken as primary input for the transfer function simulation.

2.4.1 *Theoretical background*

Two conducting parallel plates separated by an insulating layer create a capacitor with a capacitance given by [10]

$$C = \varepsilon l \frac{t}{g} \tag{2.3}$$

where t is the width of the plates, l is the length of the plates , g is the separation between the two plates and ε is the dielectric constant of the air gap. If the finger overlap is l, finger thickness is t, finger gap is g, then the capacitance becomes:

$$C = \varepsilon l \frac{t}{g} \tag{2.4}$$

If a voltage V is applied across these two plates, the potential energy of this capacitor is

$$U = -\frac{1}{2} C V^2 = -\frac{\varepsilon y t V^2}{2g} \tag{2.5}$$

For electrostatic actuation a voltage is applied on the fixed electrode. The movable electrode at ground potential will be displaced in the y direction due to the fringe

fields created in the comb. And thus the driving force F_f created in the comb can be expressed by the following formula[11]:

$$Fy = -\frac{\partial U}{\partial y} = \frac{nt\varepsilon V^2}{g} \tag{2.6}$$

where n is the number of fingers, t is the thickness of the electrodes, ε is the dielectric constant of the air gap, V is the voltage between the electrodes and g is the gap between fingers. See Figure 2.13.

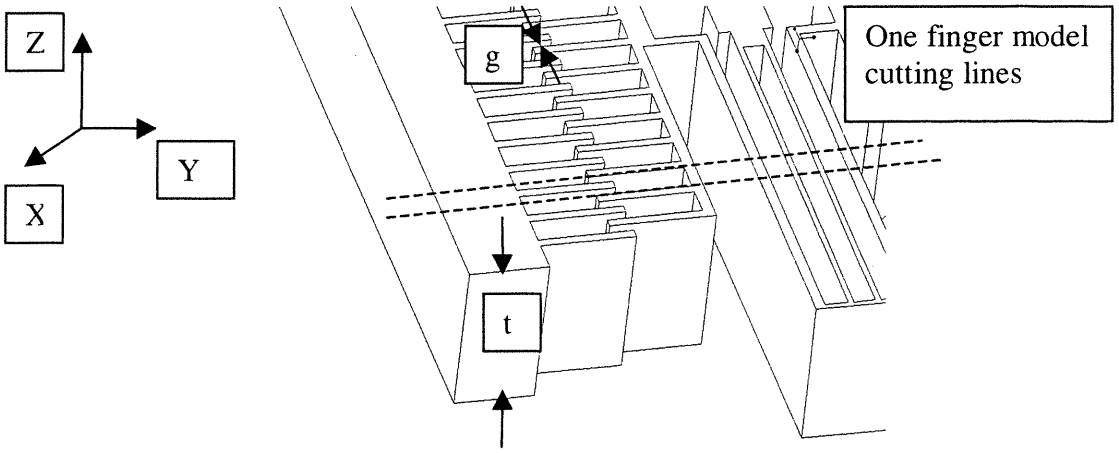

Figure 2.13 Comb finger structural parameters.

If the displacement of the electrode follows Hook's law, a reaction force F_k is generated

$$F_k = k\Delta_y y \tag{2.7}$$

Where k_y is the spring constant in y direction and Δy is the displacement. In equilibrium, the forces F_y and F_k have to be equal and the displacement can be expressed as a function of the voltage V and the other parameters

$$\Delta y = \frac{nt\varepsilon V^2}{gk_y} \tag{2.8}$$

The above equation indicates that a narrow gap between fingers, a large number of fingers, thick finger structures and a large driving voltage are desirable for large displacements. The key point is to design the comb finger that can provide enough force to drive the mirror over 50 μm at an IC compatible voltage range (less than 100 Volt).

2.4.2 *One finger/tooth model*

A one finger/tooth model is built for capacitance simulation (Figure 2.14). In Figure 2.14, in addition to one pair of finger/tooth, the model encompasses the segments cut (Figure 2.13 with dotted lines) from the folded beam. The simulation parameters are listed in Table 2.8. Basically, the one finger model is surrounded by an air-meshed box which defines the boundary conditions for this model.

However, two sets of infinite elements need to be included so that the electric distribution field is simulated as close to the real situation as possible. Therefore, two cases with infinite elements are examined. One is to add the infinite elements on the top of the box, another is to add the infinite elements on the top, as well as at both front-back ends of the boundary box. Figure 2.15 shows the meshed

boundary box implemented in the simulations with the infinite elements only on the top of the box.

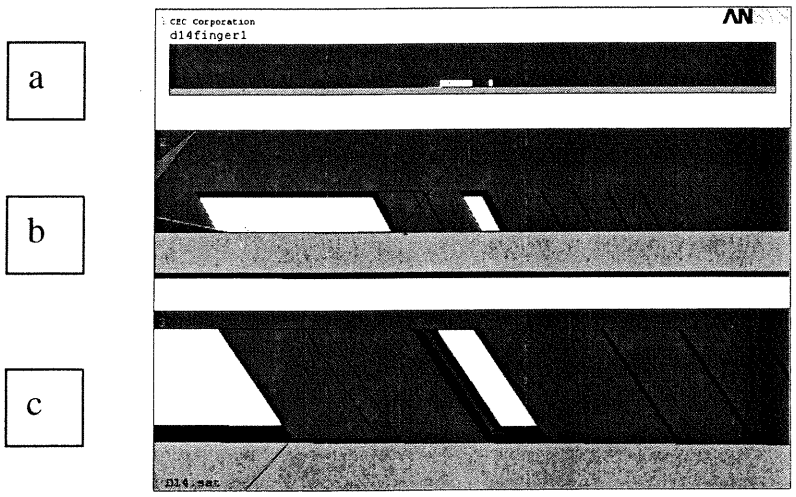

Figure 2.14 One finger model for capacitance simulation. (a) is the cross section view of the model with "air box" , (b) and (c) are enlarged views of the finger cuts.

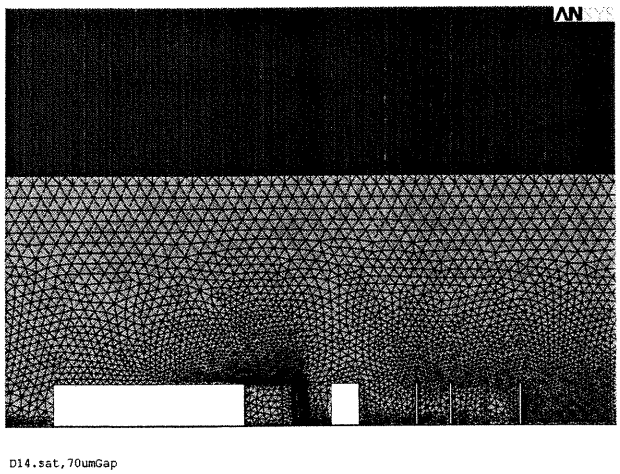

Figure 2.15 One finger model with meshed boundary box (infinite element on the top case).

A modified version of the ANSYS CMATRIX.MAC is used to compute the capacitance over a range of comb stroke positions.

Table 2.8 One finger/tooth model simulation parameters.

Element Type	Displacement Range	Finger Length	Finger Width	Finger Gap	Initial Overlap
Solid123 Tetrahedral	0- 55 μm	90 μm	3 μm	3 μm	20 μm

2.4.3 *Simulation results*

Figure 2.16 shows the simulation results from three different boundary conditions in comparison with theoretical calculations from equation (2.4). The capacitance as a function of finger displacement follows almost the same linear relation under three different boundary conditions described above. The difference between the simulation and calculations is about 0.27 pF. In Table 2.9, a comparison between those three simulations is presented.

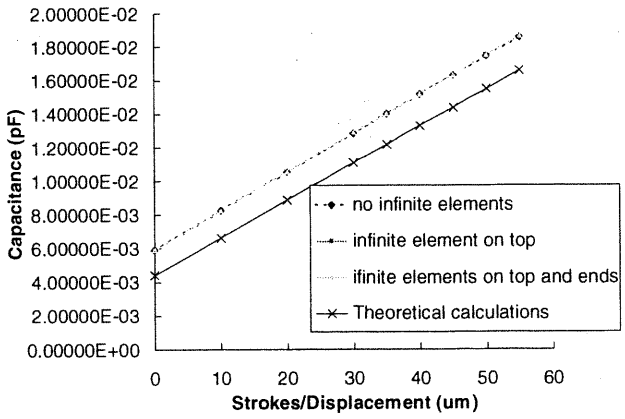

Figure 2.16 Capacitance simulations compared with theoretical calculations (eq2.8).

Table 2.9 Simulation comparison between different boundary conditions.

File name	015	070	080	090	100	110	125
Strokes	55 μm	0	-10 μm	-20 μm	-30 μm	-40 μm	-55 μm
No-Infinite	1.8600	0.5924	0.3620	0.1321	0.0417	0.0257	0.0194
inftop	1.8633	0.5934	0.3634	0.1335	0.0430	0.0271	0.0189
inftoend	1.8632	0.5936	0.3633	0.1335	0.0430	0.0271	0.0189

Figure 2.17 (a)-(c) shows the electrical field distribution around the finger overlap region from the simulation results. (a) is the case that infinite elements are used on the top of the boundary box, in (b) the infinite elements are used both on the top and on the two ends of the boundary box, while in (c) there are no infinite elements used.

2.5 Coupled Field Simulations

In coupled field analysis, the comb capacitors are replaced with the TRANS126 transducer. A single transducer is used for the drive comb. A three-dimensional finite element model of the comb structure is modeled over the stroke-range of the device to compute the capacitance as a function of stroke. This relationship forms the input parameters for the transducer element. Only uniaxial motion (y direction) is considered at the connection point to the resonator. The

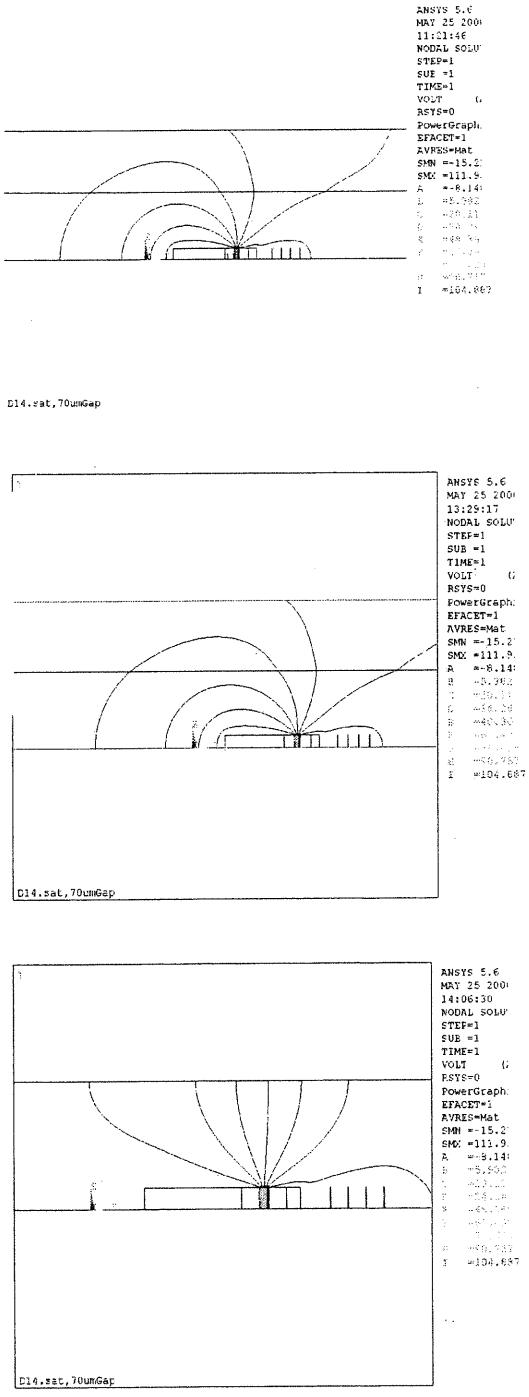

Figure 2.17 Simulated electric field distributions. (a) No infinite elements (b) Infinite elements on top of the box (c) Infinite elements on top and both ends.

simulation uses a complete lumped element approach as shown in Figure 2.18. The stiffness of the system is computed from the static simulations where the applied force and displacement are recorded to compute stiffness. The effective mass is determined from an eigenvalue analysis. The damping factor is preset to correspond to a Q-factor of 100.

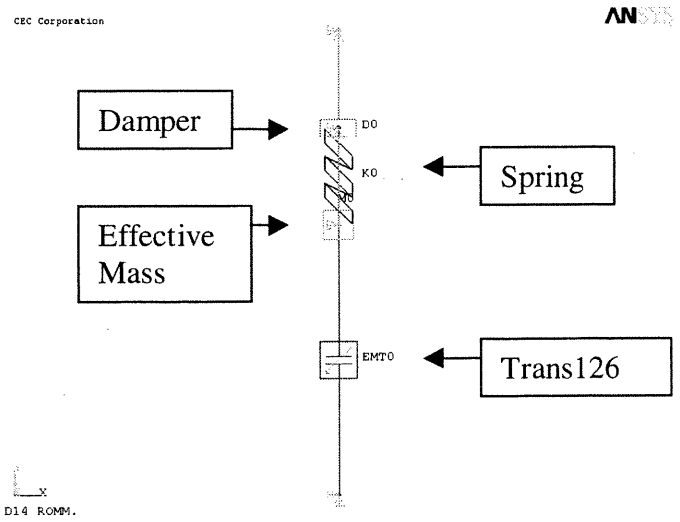

Figure 2.18 Reduced Order Model (ROM) for coupled field analysis.

2.5.1 *Transfer function*

A reduced order macro model (ROM) of the system has been developed and is shown in Figure 2.18. This simple model consists of a spring, mass, damper, and electro-mechanical transducer. The model has only one structural and one electrical degree of freedom, making it very quick to solve. Since the ROM only contains one structural degree of freedom, it has only one structural vibration mode, and is therefore unable to account for more complicated structural response.

The effective mass used in the ROM model is that which corresponds to the first vibration mode as obtained from model analysis of the complete device.

Key parameters for the model are determined via the static structural, model, and electrostatic analyses described above. A static analysis based upon the parameter values in Table 2.10 and Table 2.9 shows that the spring beams will bump up against the stops, and the switch will reach its maximum deflection of 55 μm, when a DC potential of about 65 volts is applied across the device. Figure 2.19 shows the deflection vs. voltage relationship for the static analysis. Note that as the electrostatic model of the comb is improved, any changes in the deflection vs. capacitance relationship will affect the behavior of the ROM model. Figure 2.20 shows the comparison between the simulation with calculated capacitance vs. simulated capacitance from Section 2.4.

Table 2.10 ROM model parameters.

K	Stiffness	1.23 μN/μm
M	Effective mass	0.4223×10^{-7} kg
Q	Quality factor (damping)	100

In Figure 2.20, both the calculated curve and the ANSYS simulated curve show the displacement saturation with driving voltage. When the driving voltage is higher than 40 volt, the displacement does not maintain linear relationship with its driving voltage, i.e. the mirror does not travel much further

even at a higher driving voltage. This saturation is probably caused by the stored mechanical potential energy in the folded beams that tehnds to pull the mirror back to its original position.

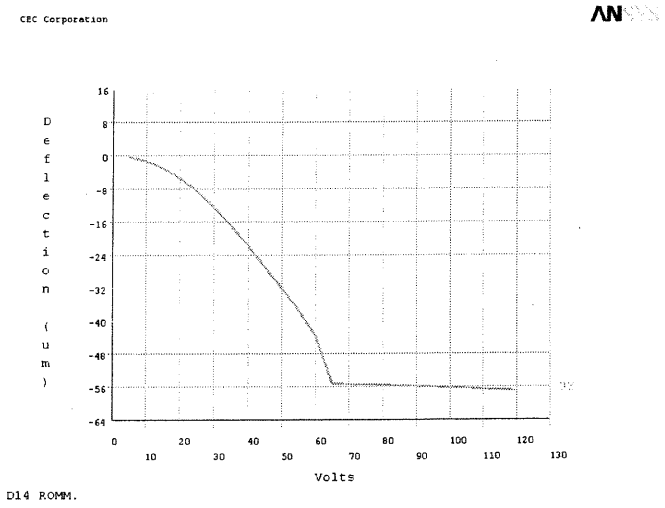

Figure 2.19 Transfer function from ROM simulation.

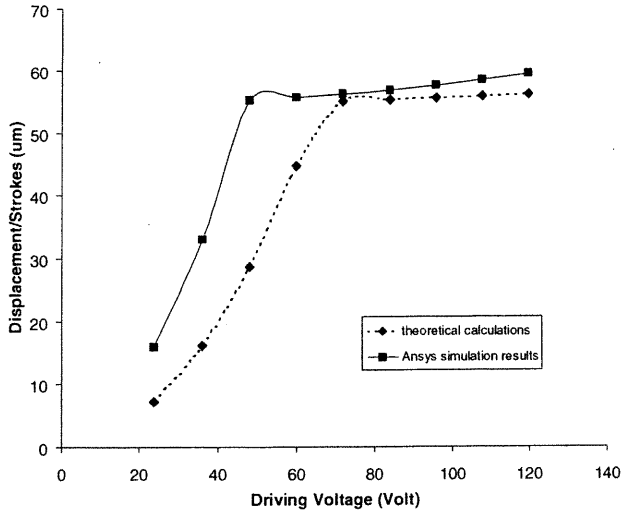

Figure 2.20 Deflection vs. voltage curves from simulations and theoretical calculations.

2.5.2 *Transient analysis*

A transient analysis of the ROM model was performed in which the mass was initially displaced 55 um (its maximum possible deflection), and then released. No potential was applied across the electro-mechanical transducer, and the equation of (2.1) becomes

$$M\ddot{u} + D\dot{u} + Ku = 0 \tag{2.9}$$

Figure 2.21 is an original ANSYS plot of the displacement of the mass as a function of time, and shows the classic decaying sinusoidal response of a system in free vibration. The duration of reduction of amplitude to 1/e is 0.04 seconds. In addition, a free vibration transient analysis has been performed using the full, 3D solid element structural model. Results from this analysis should be useful in indicating the stress levels within the MEMS structure for various positions within its stroke, as well as for predicting the amount of "off-axis" deflection (UX and/or UZ) of the mirror.

Figures 2.22 and 2.23 show the model transient model behaviors along X and Z direction, respectively. The vibration amplitude envelope along X is periodic, the maximum of which is about 1.0 μm, while the minimum is about 0.1 μm. Along the Z direction the vibration amplitude reduces from 0.8 mm to 0.4 μm in a period of 0.02 Seconds.

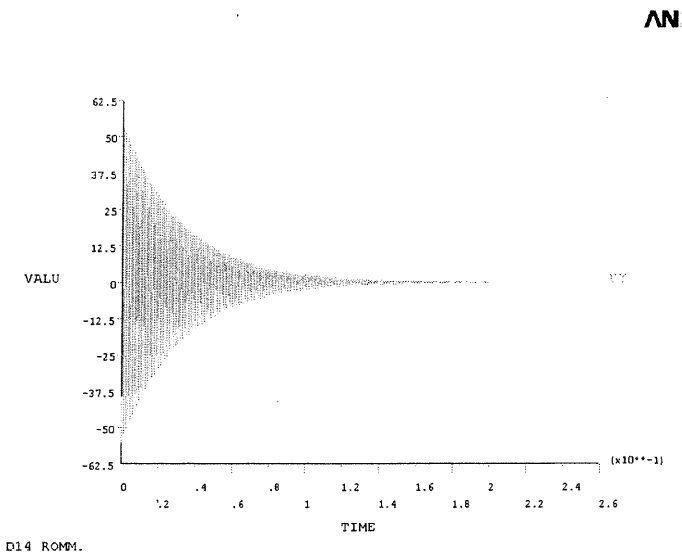

Figure 2.21 Displacement as a function of time (ROM); Horizontal axe is: time in second and vertical axe is: displacement amplitude in micron.

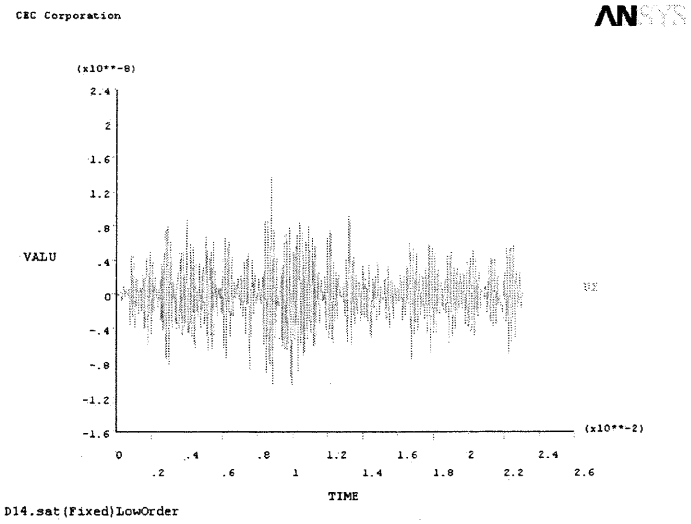

Figure 2.22 Displacement along Z direction as a function of time (full model); Horizontal axe is: time in second and vertical axe is: displacement amplitude in micron.

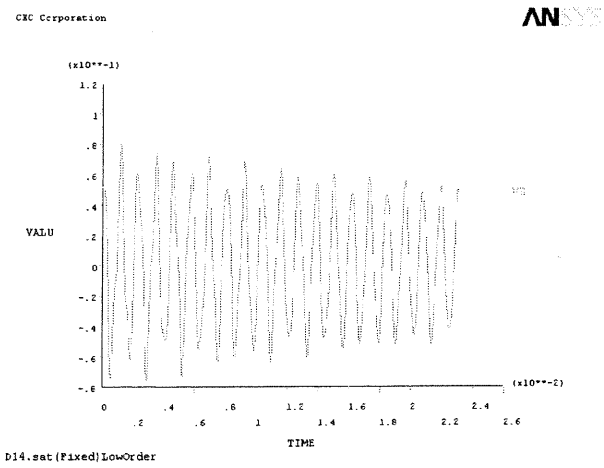

Figure 2.23 Displacement along X direction as a function of time (full model); Horizontal axe is: time in second and vertical axe is: displacement amplitude in micron.

3. DESIGN CONSIDERATIONS

The optimal design parameters acquired from previous ANSYS simulation sections are listed in Table 2.11. First, after the folded beam design simulations and consideration from section 2.2.2, the folded beam that has length of 790 μm and width of 3 mm is the design choice that can fulfill both the large displacement requirement and yet maintain a durable mechanical structural. With this folded beam, the force required to actuate for a 55 μm displacement is analyzed at 68 μN. Another conclusion can also be drawn, that is the smaller the fingers gap the larger the driving force. However, the gap is limited by the etching aspect ratio that can be obtained through deep dry etching process. The 3 μm gap is chosen to keep a 1:25

aspect ratio for deep etching to 75 μm trench. With 140 finger pairs, overlap of 20 μm, the corresponding voltage is 64 Volt obtained from transfer function simulation. The larger overlap will contribute to a larger driving force. The instability of the actuator is proportional to the overlap length (See Appendix A).

Table 2.11 Optimal design parameters for electrostatic comb actuator from FEM.

Folded Beam		Comb Fingers					Comment
Width	Length	Length	Width	Overlap	Number	Gap	64 volt for
3 μm	790 μm	90 μm	3 μm	20 μm	140	3 μm	55 μm

In order to test the ANSYS simulation result, a set of designed actuators are made in one mask layout for later fabrication. Beam lengths in a range of 700 μm to 1100 μm, beam widths range from 2 μm to 9μm, finger widths from 2 μm to 5 μm, the finger overlap is from 20 μm to 30 μm and there are from 140 to 170 finger pairs. Table 2.12 lists the actuator designs that will be focused on through the fabrications because those are most promising designs obtained from ANSYS simulations. Those designs combine the parameters that most likely deliver the performance that is desired for the switching design.

Table 2.12 The comb actuator design sheet (unit: μm).

Beam Length	Beam Width	Finger Width	Finger Gap	Finger Overlap	Finger Number
790	5	3	3	20	158
790	5.5	3	3	20	140
790	6	3	3	20	140
790	3	3	3	20	140
790	4	3	3	20	140
1100	5	3	3	20	140

REFERENCES:

1 **Fan, L.S., Tai, Y.C., Muller, R.S.,** " *IC-Processed Micro-Motors Design, Technology, and Testing,*" Tech. Dig. IEEE Micro Electro Mech. Syst. Workshop, Salt Lake City, UT, Feb. 20-22, (1989), 1-6.

2 **Mehregany, M., Nagarkar, P., Senturia, S.D., Lang, J.H.,** " *Operation of Microfabricated Harmonic and Ordinary Side-Drive Motors*", Tch. Dig. IEEE Micro Electro Mech. Syst. Workshop, Napa Valley, CA, Feb, 11-14, (1990), 1-8.

3 **Tang, W.C., Nguyen, T.H., Howe, R.T.,** *"Laterally Driven Polysilison Rosonant Microstructures"* Tech. Dig. IEEE Micro Electro Zmech. Syst. Workshop, Salk Lake City, UT, Feb. 20-22, (1989), 53-59.

4 **Tang, W.C.,** *"Electrostatic Comb Drive for Resonant Sensor and Actuator Application"*, Ph.D. dissertation, University California, Berkeley, CA, 1990.

5 **Kim, C.J., Pisano, A.P., Muller, R.S., Lim, M.G.,** *"Polysilicon Microgripper*" Tech Dig. IEEE Solid-State Sensor and Actuator Workshop, Hilton Head, SC, (1990), 48-51.

6 **Takeshima, N., Gabrial, K.J., Ozaki, M.,** "*Electrostatic Parallelogram Actuators*" Dig. Tech. Papers, Transducers'91, San Francisco, CA, 63-66.

7 **Ostergaard, D., Gyimesi, M., Affour, B.,** "Efficient Reduced Order Modeling for System Simulation of Micro Electro Mechanical Systems (MEMS) from FEM Models" CAD, Design and Test, 1999.

8 **Gyimesi, M., Ostergaard, D.,** *"Electro-Mechanical Transducer for MEMS Analysis in ANSYS"*, Proc. ICCAD, IEEE, (1999) 283-286.

9 **Varghese, M., Rabinovich, V.L., Senturia, S.D.,** " *Reduced-Order Modeling of Lorentz Force Actuation with Model Basis Functions*", External customer exchange copy, 2000

10 **Trimmer, W.S.N., Gabriel, K.J.,** *"Design Considerations for a Practical Electrostatic Micro-Motor"*, Sensors and Actuators, 11 (1987), 189-206.

11 **Jaecklin, V.P., Linder, C., de Rooij, N.F., Moret, J.M.,** *"Micromechanical Comb Actuators with Low Driving Voltage"*, J. Micromech. Microeng., 2 (1992), 250-255.

12 **Gere, J.M., Timoshenko, S.P.,** *Mechanics of Materials*, PWS, 1997, Forth Edition.

CHAPTER 3: CHIP FABRICATION AND CHARACTERIZATIONS

1. INTRODUCTION

The MEMS fabrication has always used a large number of very sophisticated techniques. Surface micromachining [1,2] and bulk anisotropic silicon etching [3-5] were used to build pressure sensors, inertial sensors, micropumps, micromotors, XY-stages and other smart devices [6-10]. Both technologies suffer some limitations such as the sticking of the structures for surface micromachining and the silicon crystal orientation dependency for anisotropic etching. Deep silicon dry etching has been investigated to extend the bulk micromachining and to fulfil some requirements like: etch depths from 20 to 300 μm, aspect ratio greater than 30 [11-14] and more freedom in design.

The fabrication process for the electrostatic actuator and associated alignment groove structures is a straightforward application of the bulk-micromachining technology. The Deep Inductive Coupled Plasma (ICP) etchings are used to define features, concluding with a final removal of a sacrificial layer to free the suspended microstructures. This chapter highlights the important processing steps, followed by a discussion on several performance-related fabrication issues.

2. FABRICATION SEQUENCE

The difficulties remaining in defining fabrication processes are how to get the smooth etching surface of the mirror with vertical profile, and how to fabricate a structure of a very large geometric aspect ratio with a good yield. From previous chapter, the FEM analysis demonstrated that the small finger gap (3 μm), narrow (3 μm) and yet longer folded beams (790 μm) are desirable for larger actuator displacement. However, the switch design requires a trench of 75 μm in depth. It becomes a challenge to fabricate structures with an aspect ratio that is over 1:25 particularly for such a small features. Therefore, it is necessary that extensive design and testing of the fabrication process are carried out to satisfy both mirror surface and actuator displacement requirements simultaneously.

The micro mirror is the crucial part of the switch that reflects the light. In real development, the mirror fabrication is developed and processed in the first place, followed by the actuator process. The integrated chip, which includes micro mirror, actuators and built-in pre-alignment grooves, is completed in the end. Instead of describing the detailed development curves for mirror and actuator, the integrated chip fabrication sequence will be presented in this section.

Silicon-on-isolator (SOI) wafers are used in the chip fabrication, the parameters of which are described in Table 3.1. Figure 3.1 is a diagram showing the

SOI wafer dimensions. Oxide layer serves as silicon etching stop layer in dry etching. The manufacturer of SOI wafers is Sibond L.L.C. , MEMC, MO.

A two-mask processing sequence is illustrated in Figure 3.2. A significant advantage of this processing is that all the critical features are defined with one mask, such as actuator, alignment grooves and micro-mirror, eliminating errors due to mask-to-mask misalignment. Moreover, this processing is also compatible with IC fabrications, which means that the integration electronics are allowed to be built in with the switch and to realize the on-chip electronic drive circuit.

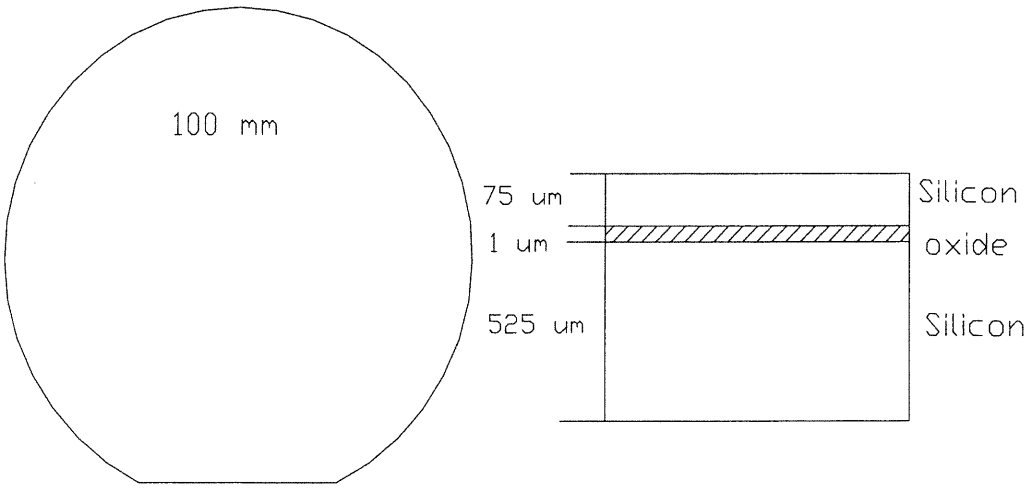

Figure 3.1 The dimensions of SOI wafers.

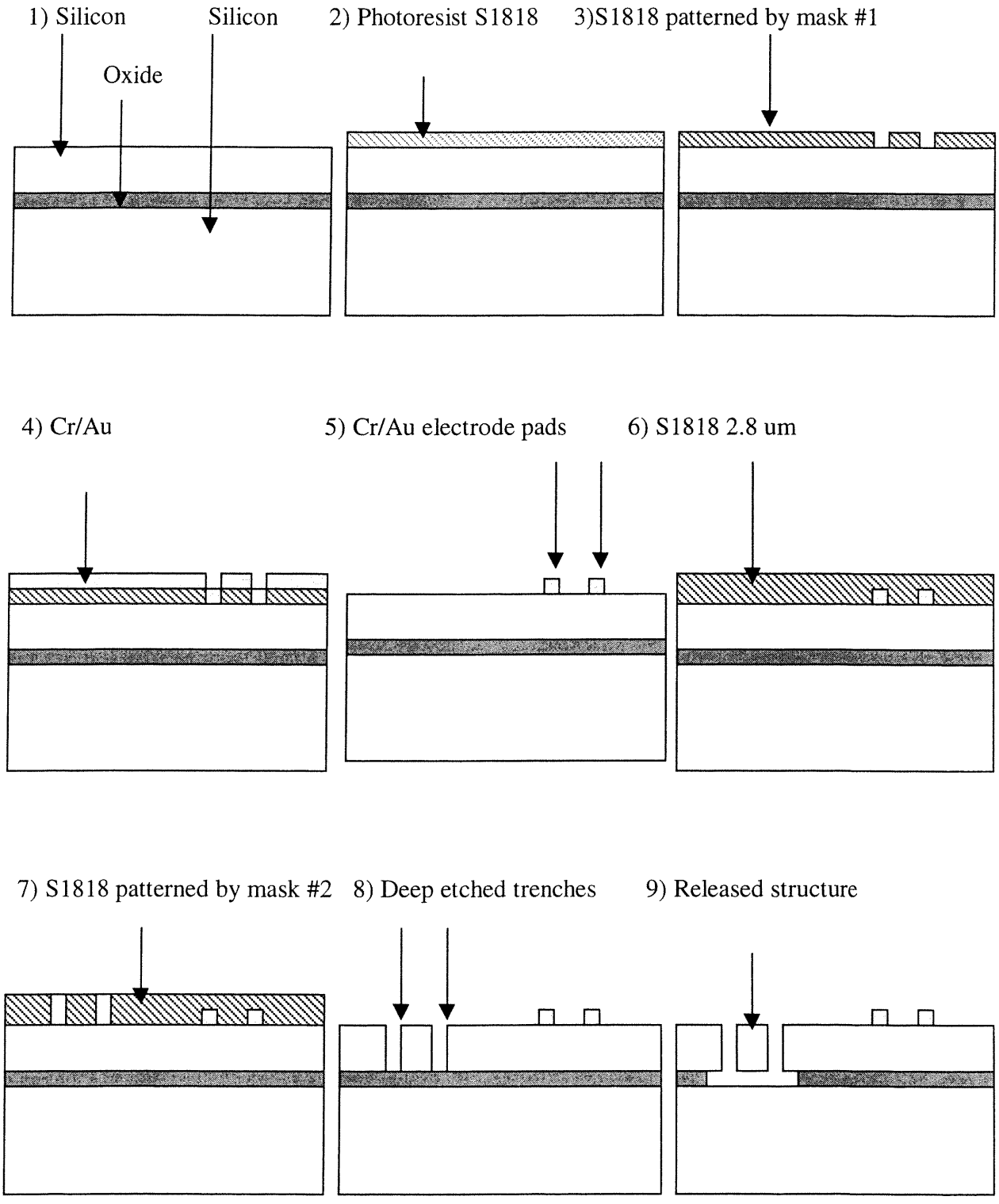

Figure 3.2 Diagrams of fabrication sequence.

Table 3.1 SOI parameters.

Handle layer	Diameter	100 mm
	Type/Dopant	P/Boron
	Resistively	8 – 22 ohm-cm
	Thickness	525μm ± 15 μm
	Backside	Etch, laser mask
	Flat	Primary only, SEMI std
Isolation layer	Oxide	1.0 μm Target Thermally grown SiO_2
Device layer	Type/Dopant	P/Boron
	Resistively	10 – 20 ohm-cm
	Thickness	75 μm ± 2 μm

The processing begins with SOI wafers (step1)) inspection. The next steps involve the definition of the electrode pad structures. First a photoresist layer (S1818) of 1.5 μm thickness is coated by a spinner (step 2), the wafer is baked in the oven at 90 °C about 30 minutes, then printed by MA6/BA6 aligner with the designed mask #1(step 3). The E-beam evaporator is used to deposit the metal film on the printed SOI wafers (step 4). The equipment is Temescal FC1800 evaporator designed for substrates (diameters of 2, 3 and 4 inches) and pieces. The following

metals can be evaporated in this system: Al, Au, Ge, Ni, Pd, Pt, Ti, Ag, Cu, Cr, and W. Cr underneath Gold is chosen to achieve a better adhesion with Silicon for wirebonding and yet a good thermal conductivity with substrate. Cr film with thickness of 500 Å is deposited at a rate of 2 Å/second and the evaporator chamber pressure is 2×10^{-6} mTorr. The Gold is deposited at the same rate with a thickness of 4000 Å under pressure of 4×10^{-6} mTorr. After metal film is deposited, a lift-off process emerges to remove the unwanted metal while keeping the electrode pad in place (step 5). The wafer is soaked in acetone for two hours and rinsed with acetone, methanol, Isopropyl alcohol (IPA) and DI-water, respectively.

After stripping the metal and photoresist layer, an extensive cleaning processing has to be carried out. This includes soaking the wafer in BOE (10:1 buffered HF) for 10 seconds, rinsing with DI-water for about 5 minutes, then soaking in the hot H_2SO_4:H_2O_2 for 20 minutes. It is necessary to fully clean the wafers before the following photolithography with the mask #2, otherwise, the small features are easily "washed" away during printing process due to poor adhesions between photoresist and silicon substrate. A double coating technique [15] (step 6) is introduced here to cover the wafer with 2.8 μm thick S1818 photoresist layer. After softbaked on a hotplate for 1.5 minutes, the wafer is then baked another 50 minutes in the oven at 90 °C. The softbaked wafers are printed with mask #2 using the same MA6/BA6 aligner (step 7). The printed wafers need to be postbaked in the oven for 30 minutes, and hence the beams, the electrostatic actuator, the supporting

structures, the micromirror and alignment grooves are all defined in this final masking step.

The structures are anisotropically patterned by deep dry ICP etching in an SF_6 plasma to achieve nearly vertical sidewall (step 8). Since this is a crucial processing step involved in the switch fabrication that has a huge impact on the device performance and fabrication yield, an extensive discussion will be given out on deep dry etching processing development in the next section.

Following the deep dry etching, the S1818 mask residuals is removed with Oxygen Asher running for 25 minutes at 400 W and 250 mTorr. To increase the reflectivity of the mirror, a final gold film of 80 nm is deposited with E-beam evaporator. The wafer is then diced into individual chip on a sewing machine. In order to protect the device from dicing damage, a photoresist S1818 is coated on top of device at 500 RPM, then bake the wafer on a hotplate at 90 °C for 1.5 minutes to keep minimum adhesion. After dicing, the movable structures is wet-released by HF. Figure 3.3 (a-d) are scanning electron micrographs of the completed structures. Figure 3.3 (a) is the structure of anchor that is grounded to support the folded beams (beams: 3μm wide, 790 μm long); (b) is the comb fingers with 3 μm width; (c) is the micromirror inserted in the middle of the optical signal intersection and the ends of the alignment grooves; and (d) is the comb actuator with supporting triangles.

Through the fabrication process, various tools have been utilized to exam the quality of device. A detailed quality control flow is attached in Appendix B.

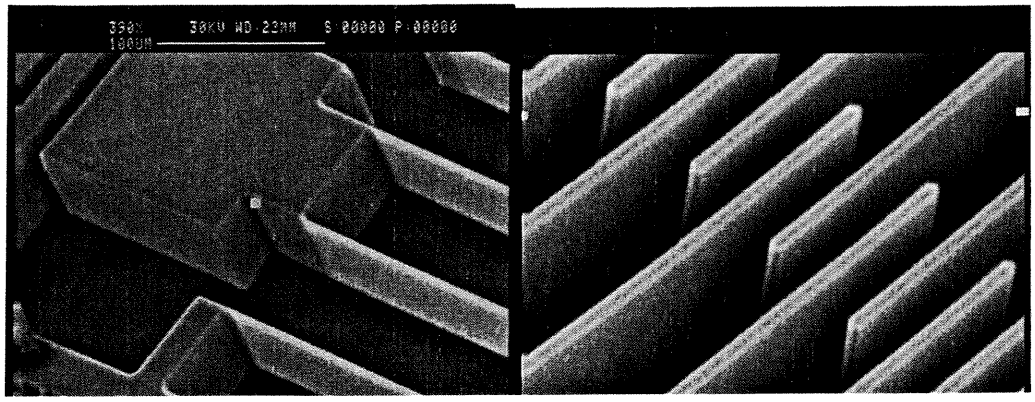

(a) (b)

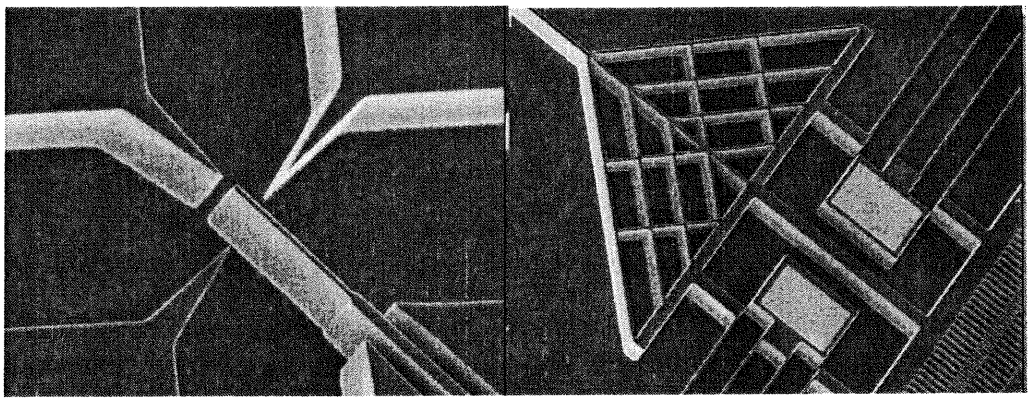

(c) (d)

Figure 3.3 SEMs of fabricated switches: (a) anchor and beams; (b) comb fingers; (c) alignment groove and mirror; (d) actuator top view.

3. DEEP DRY ICP ETCH

Having described the fabrication sequence, several important processing issues involved with deep trench etch process are identified and discussed, which largely affect the yield and performance of the finished structures. First, a brief

background on dry etch techniques is introduced, then the parameters needing to be well controlled in the deep dry etching processing are described. Also, the dry deep trench etch fabrications have been characterized.

3.1 Introduction

The deep etch has to meet several requirements. Since the etching step is usually only part of a complex fabrication sequence, it is advantageous, if process-compatible masking materials can be applied, e.g. photoresist or an already existing layer. In particular, the silicon must be etched with sufficient selectivity compared with masking material. For exact definition of the geometry of the microstructures, it is also necessary that etch depth and etch profile can be well controlled. On the other hand there exist common wet etchants. Mixtures of HNO_3, HF, CH_3COOH and/or water exhibit relatively high etch rates (10 – 300 μm/min), but etch the silicon isotropically and the process is hard to control. Other wet etchants such as KOH or EDP attack silicon anisotropically, that is, attack particular crystal planes more rapidly than others. KOH, for instance, shows a well controllable etch behavior, but the potassium ions may change the electrical characteristics of circuits[16]. An additional problem for most wet etchants is the need for special masks, which are often difficult to be adopted in the processing sequence.

The deep dry etching technology emerges, as the anisotropic etching of silicon is becoming increasingly important as device sizes shrink. Small dimensions are making edge losses and edge geometry more critical [17].

There is a diverse range of plasma sources available on the market today for silicon deep dry etching, including reactive ion etching (RIE), magnetically enhanced RIE (MERIE), electron cyclotron resonance (ECR), and inductively coupled plasma (ICP). Not all of these are suitable for high aspect ratio deep etching. The suitability can best be judged in terms of the critical operational parameters of the plasma source. One of the key parameters is the pressure. This strongly influences physical properties of the plasma, gas fragmentation and hence surface chemistry. In terms of the plasma, low pressure will result in reducing the collisional Ion/neutral scattering, thereby improving the ion directionality. In addition, benefits are gained such as increasing the volatility of reaction by-products and reducing gas phase and surface polymerization. This has additional benefits of reducing residues, contamination, etch product redeposition and particle levels. High-density sources, which rely on resonant energy transfer and some degree of plasma confinement, can overcome these deficiencies allowing low-pressure operation and higher etch rates. Diverging ion trajectories from ion-neutral collisions in the sheath can influence the sidewall profile. High ion densities decrease the sheath thickness ($\propto \eta_I^{-1/2}$) which further reduces ion/neutral scattering, thereby potentially improving profile control[18]

.

Various RF and microwave coupling techniques are capable of exciting plasma in this mode. Of these, inductive coupling is now recognized as perhaps the simplest and yet the most flexible excitation technique. The ICP is based on a simple principle of operation: a time varying axial magnetic field induces an azimuthal electric field (from $-d\beta/dt = \nabla \times E$) which effectively confines the plasma current. The energy of ions impinging on the wafer surface can be independently controlled by using RF biasing. This simple principle of operation allows a wide processing window and an ease of scalability, which is not possible with some of the other resonant techniques such as ECR. Another concern of diffusion source such as ECR is relatively poor uniformity over large areas through a general lack of scalability. Thus the ICP would appear to be the most suitable source for this application.

The dry deep etcher utilized is Plasma-Therm ICP etcher, manufactured by Plasma-Therm, FL. The standard etching processing for this ICP etcher is patented Bosch silicon etching processing[19], which is deep silicon dry etching technique at room temperature involving a cycle of silicon sidewall passivation and an aggressive SF_6 etch. The mechanism of fluorine chemistry in plasma etching is described in Figure 3.4. It is an isotropic etching if there is no passivation processing involved. The passivation processing is depicted in Figure 3.5, which is introduced to achieve a vertical profile of etched sidewall. The gas for passivation is C_4F_8, and SF_6 for etching. In the passivation cycle, the newly etched portions are protected by polymers formed on the sidewall so that only the exposed portions close to the bottom of the trenches are etched in the followed etching cycle. By carefully

balancing the etching and passivation cycling a well controlled vertical profile can be obtained. Therefore, how to modify the Bosch process to be applied to the switch chip fabrications is discussed next.

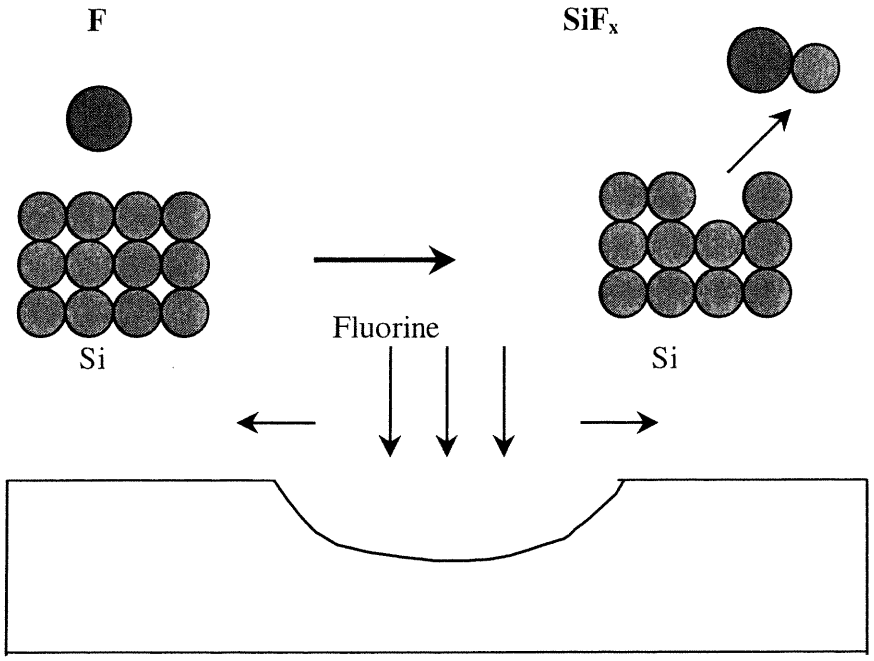

Figure 3.4 Schematic of fluorine chemistry in plasma etching.

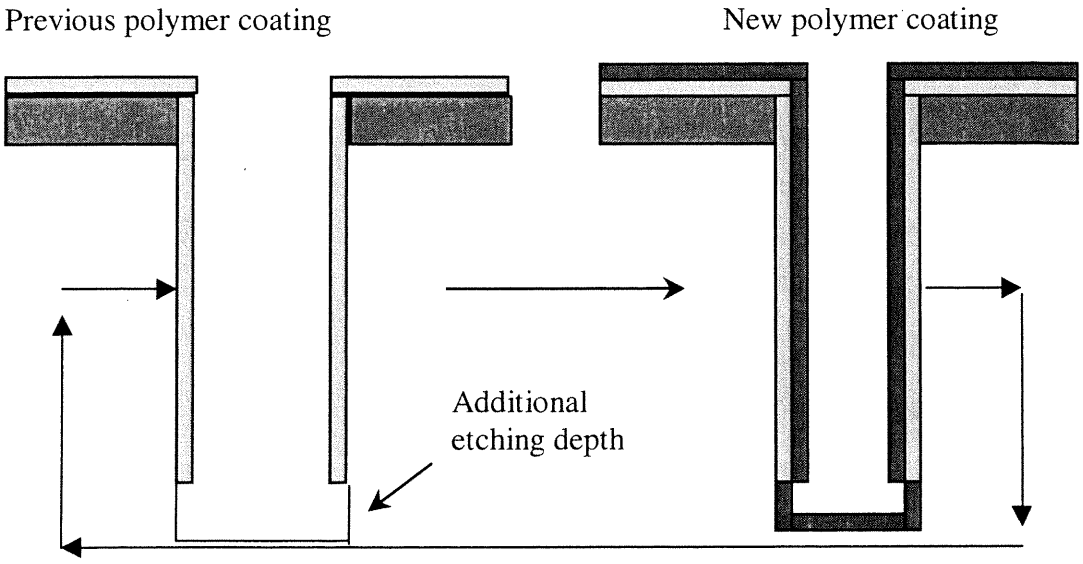

Figure 3.5 Cycling schematic between etching and passivation.

3.2 Process control and characterizations

The requirements for dry etching can be summarized as: 1) High etch rate for high throughput with precise etch stop; 2) Controllable etch profile: vertical, tapered, undercut; 3) High etch selectivity of etch mask; 4) Low surface damage: avoid contamination and defect generation 5) Uniform and reproducible. To meet those requirements, there are a couple of parameters that need to be well defined in the dry etching processing, and those are rate, profile, selectivity, and uniformity. Sometimes a compromise has to be made in order to get balance between different parameter needs. In the following sections some effects that influence the consequences of the deep dry etching are discussed, and the device performance are characterized.

3.2.1 *Undercutting and over-cutting*

Structure undercutting is largely caused by microloading effect introduced during deep trench etching. Microloading effect, defined as the etch depth reduction with reduction of trench width dimension, is called etch-size-dependent effect or lag-effect. It needs to be minimized for a synchronous etching and is dependent upon a number of parameters including the collision probability [18]. This probability is given by ion sheath thickness (d_I) over ion mean free path (I_I):

$$\rho_c = d_i / I_i \propto pV^{3/4} \eta_e^{-1/2} T_e^{-1/4} \rho \qquad (3.1)$$

where V is the sheath potential, η_e and T_e are the electron density and temperature respectively. This suggests that low pressure, low bias and high plasma density can reduce microloading effect.

Figure 3.6 (a) shows the undercutting that occurred between narrower trenches. The etch rates of larger open trenches are higher than those of narrower trench gaps. If the pressure maintains constant, the etch rate increases with the spacing between elements, that is, the larger the trench gap the faster the etching. This is because with narrow gap the trench bottom becomes harder to be reached by the active particles, and hence the etching rate is reduced. The microloading effects in the deep dry etching processing are measured with Scanning Electronic Microscopy (SEM). Figure 3.6 (b) is a SEM picture shown the lag-effect measurements. The samples that were designed with various widths of trench gaps are fabricated by deep dry ICP etching, and then are cut with cross section for the lag-effect measurements by SEM.

In Figure 3.7, the curves a and b represent the relationship between lag-effect and the trench gaps, that is the lag-effect increases gradually with the reduction of the trench gap. When the trench gap is less than 10 μm, the lag effect became more severe. Taking the lag-effect as zero for trench gap of 100 μm, the maximum lag-effect of 0.4 μm/min is reached for gap=3 μm at pressure = 24 mTorr. If too much undercutting occurs on the bottom, some small features with larger open

gaps will be over-etched while elements between small gaps have not been etched to the oxide layer and hence will not be released from substrate as needed.

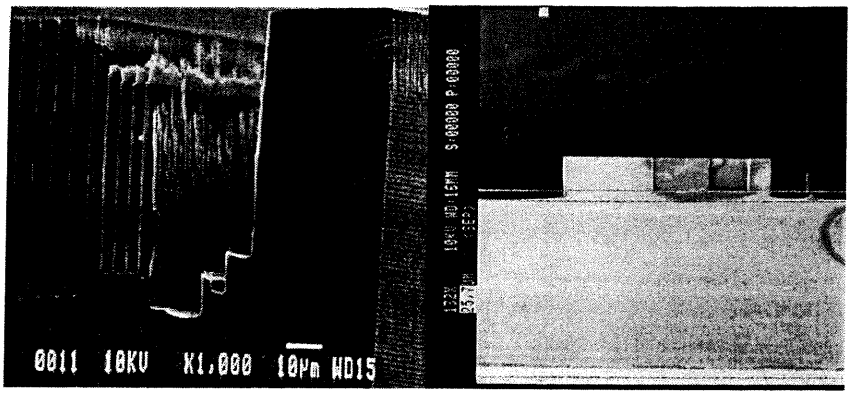

(a) (b)

Figure 3.6 SEM photos of undercutting etched by Deep ICP etcher: (a) is the undercutting features (Pressure: 23 mT, DC bias: 60 W, RF power: 825 W); (b) is the cross section for lag-effect measurements (Pressure: 23 mT, DC bias: 60 W, RF power: 825 W).

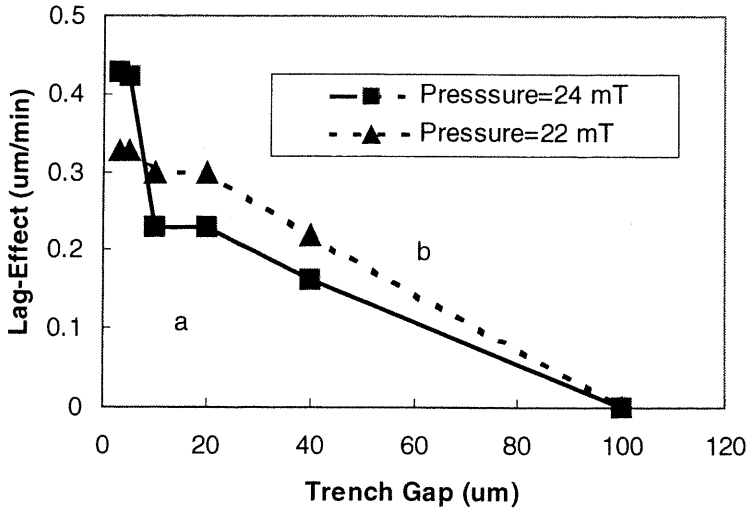

Figure 3.7 The Lag effect against the trench gap.

The lag-effect , however, can be improved by adjusting etching parameters, for instance, chamber pressure. In Figure 3.7, curve a and b are measured under different pressures and less lag-effect is observed when chamber pressure maintain at 22 mTorr.

On the other hand, over-cutting on top of the small features can be caused by the masking material selection. Figure 3.8 (a) shows the comb drivers that are etched by using SiO_2 as deep etch mask. The finger tops are heavily etched away. While in Figure 3.8(b), which photoresist is used as etch mask, no over-cutting occurred even for 3 μm fingers with 3 μm gaps in between. The Dektak surface profile measurements in Figure 3.9 evaluate the mirror top overcut introduced by using oxide as deep etching masking material. 3.9 (a) is the top of the mirror suffered undercut so sever that majority of the mirror is gone , while the 3.9 (b) the mirror top overcut is significantly reduced after using PR as masking materials.

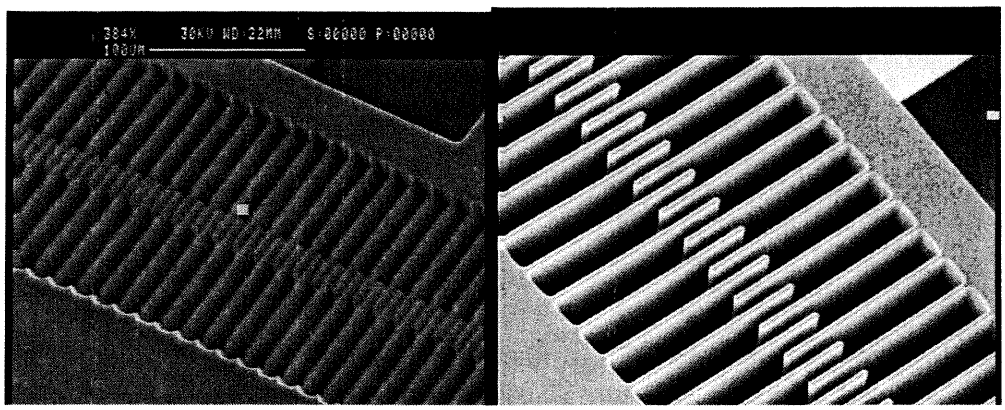

(a) (b)

Figure 3.8 Deep etching comparison: (a) using SiO2 as masking materials; (b) using photoresist as masking material.

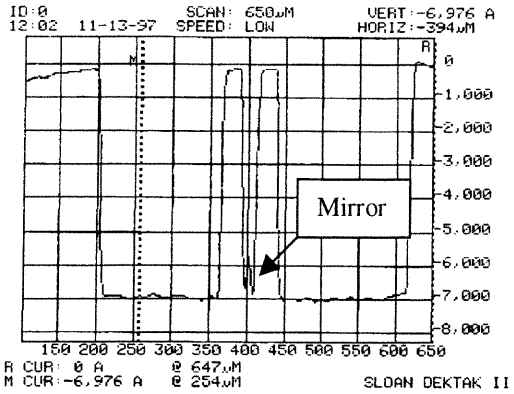

(a)

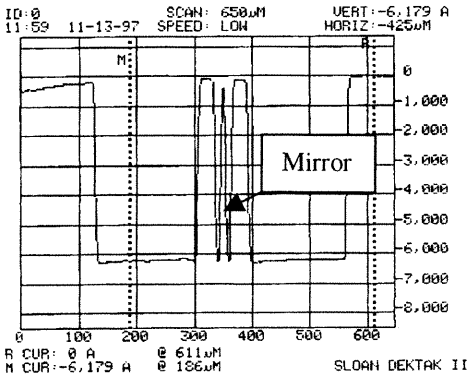

(b)

Figure 3.9 Mirror top overcuts measured by Dektak: (a) SiO_2 as etching mask; (b) photoresist as etching mask.

The reason of the over-cutting in Oxide-masking-etching is probably that in comparison with photoresist, the etching with an oxide mask is more isotropic. A possible explanation [20] is that more radicals containing carbon are generated during etching with photoresist than with an oxide mask. Such radicals react on the sidewalls and produce additional polymeric films, which then impede lateral etching [21].

3.2.2 *Vertical profile and protection wall*

Among the parameters, the etch profile is very important for switching applications. If the mirror is not perfectly perpendicular, the light reflecting off the mirror will be offset from the path and miss the receiving fiber input end to cause additional insertion loss. Thus anisotropic etching is highly desirable for a vertical etching.

Anisotropy A, can be defined in terms of vertical (V_v) and lateral (V_l) etch rates as

$$A = 1\text{-}V_l/V_v \qquad (3.2)$$

Anisotropy in reactive dry silicon etching essentially results from either one or two of the following mechanisms:

1. Reduction in the reaction probability at the sidewall below a critical value. In other words, reducing the spontaneous lateral etching rate to zero. This can be achieved by reducing the chamber pressure.
2. Sidewall passivation (as shown in Figure 3.5 in the introduction section) based protection from radical, atomic, and neutral etching species, with or without the addition of a polymerizing chemistry. Sidewall passivation based anisotropy can be enhanced by reducing the reaction probability depending on the precursor gases.

Figure 3.10 (a) and (b) are the etching results under different chamber pressures. Less pressure will improve the anisotropic etching such that the small features will not be etched away.

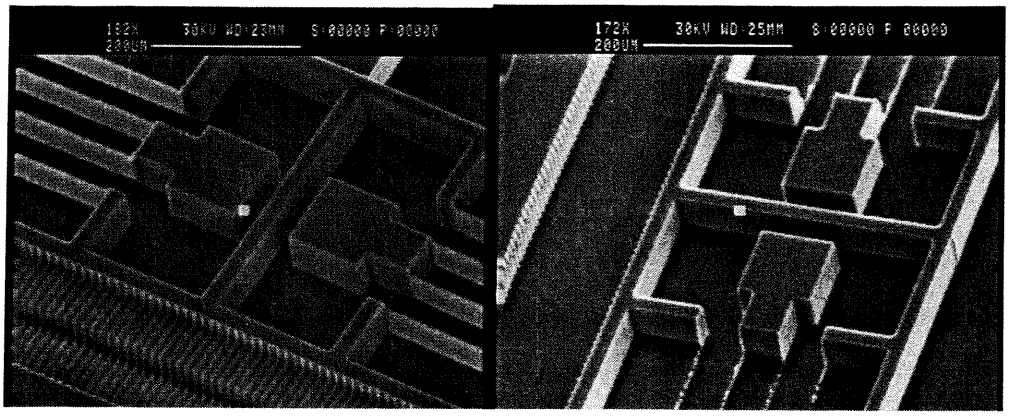

(a) (b)

Figure 3.10 SEM photos of the actuator etching features. (a) over-etched fingers (Pressure: 24 mT, DC bias: 60 W, RF power: 825 W) and (b) etched away fingers beams (Pressure: 25 mT, DC bias: 60 W, RF power: 825 W).

The passivation and etching cycle parameters of Bosch [19] processing has also been modified to achieve the vertical profile and yet retain the smooth surface finish. The aggressive etch time is decreased, while the secondary etch time and passivation time are increased. Therefore, the overall etch rate becomes lower than the Bosch program, but a relatively high vertical profile is obtained. Figure 3.11 shows the results before and after etching. The measured verticality for Bosch etching is larger than 89 ° while for modified Bosch processing, a 90 ± 0.1 ° verticality has been obtained.

On the other hand, in the original switching structure (as shown in Figure 1.1) a large trench gap discrepancy exists throughout the design layout, for instance, the trench gap between finger is 3 um, while around mirror, there is a wide open space which will lead to a much faster etching rate (Microloading effect). If not well controlled, quite often the mirrors will be etched away during ICP etching. In order to prevent from mirror-over-etching, two protection walls (Figure 3.12) are built along the both sides of the mirror that serve as trenches to give mirror a narrower open gap and hence slow down its etching rate [22].

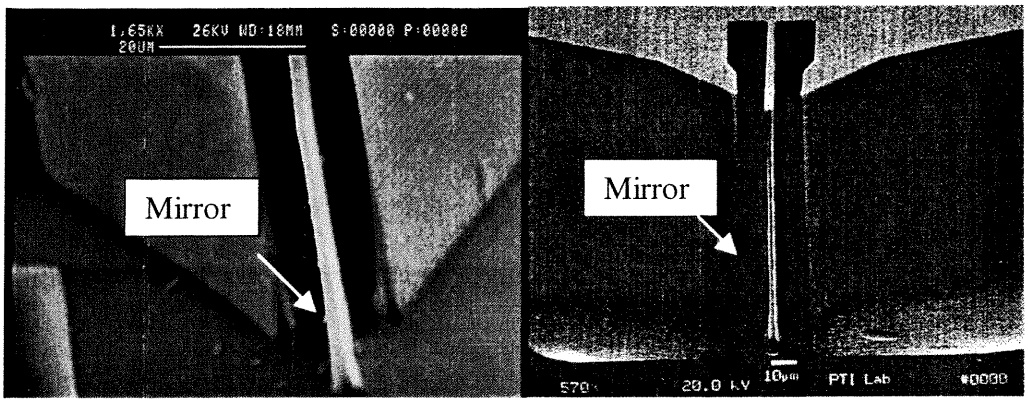

(a) (b)

Figure 3.11 Mirror vertical profile comparison: (a) fabricated by Bosch; (b) fabricated by modified Bosch.

Moreover, for deep dry etching, the profile of the trench sidewall varies with the width of the trench. A trench width of 20-30 microns will provide close to a vertical profile (90 °). The profile will go towards re-entrance (> 90 °) as the trench width get larger. In the design of optical switch, the initial position of the mirror is exposed to a very large area that the trench width could be above 100 microns. Therefore, after Deep Trench Etch, the mirrors will not be perfectly vertical

and hence the insertion loss will increase due to the signal loss coming from the light scattering. By building two protection walls along two side of the mirror, which are located 20 microns on the both sides of the mirror, the trench for the mirror becomes 20 microns which is the optimized width to obtain a vertical etch profile. The protection walls then can be etched away in late release procedure. Therefore, having the protection walls in place will benefit on a uniform etch rate, a vertical profile and a smooth surface finish[22].

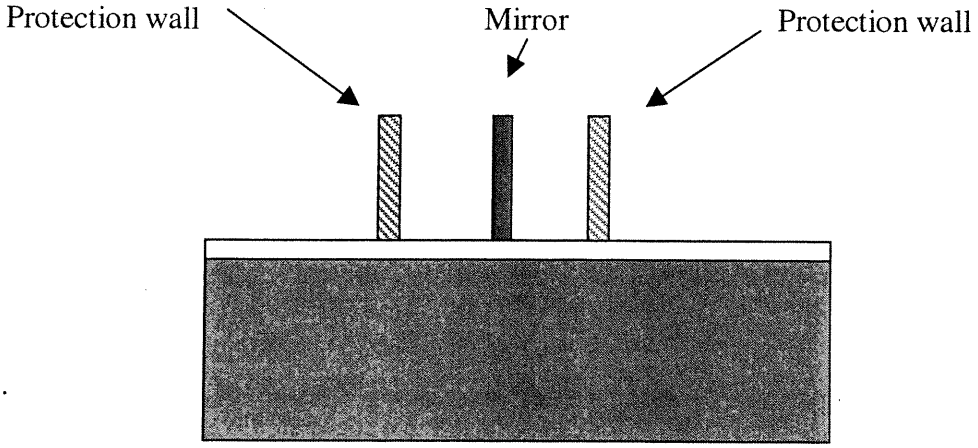

Figure 3.12 Protection wall for mirror deep etching profile and etch rate control.

3.2.3 *Uniformity*

Etching uniformity is very important because it is directly related to device yield and performance. Besides a balanced design helps to obtain a uniform etching as mentioned above, controlling processing parameters has even greater impact on the uniformity. The etch uniformity with modified Bosch is measured on a 4 inch wafer scale and the variation on the whole wafer is about ±5%. Figure 3.13

shows an etching uniformity testing map, and on the far top right corner the etching tends to be faster than the rest of the region. That is possibly caused by the uneven-gas-flow during the etching process. In addition to the overall etch rate uniformity, some specific uniformity issues also have to be addressed, such as the etch sidewall and trench bottom. For the sidewall, some surface variations due to the etch and passivation cycles are observed. The surface roughness will be discussed in detail at the following section. Here the trench bottom uniformity after deep etch is shown. Figure 3.14 is the SEM photo taken during the mirror development process. Picture (a) shows heavy vertical striations and mirror over-cutting on the chip. In fact, the over-cutting is so severe that the micro-mirror is completely etched away. The insufficient passivation cycling causes this phenomenon. If the passivation cycle time is too short, especially with increasing trench depth, the trench bottom does not get enough polymers to fully protect the sidewall so that in the next etching cycle the uncovered part of the sidewall is bombarded by the particles and create the vertical striations. The insufficient passivation also leads to the over exposure of the micro-mirror to the etching particles even for the etching by using photoresist as mask. The photo (b) in Figure 3.14 shows a result after increasing the passivation cycle. The "grass" structures are improved. The photo (d) is the etching result by increasing passivation time from 3 seconds to 5 seconds and no vertical striations and mirror over-cutting is visible.

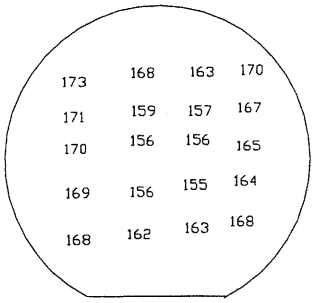

Figure 3.13 Etching uniformity measurement data map. (unit:μm, Etching time: 140 minutes, Uniformity: ±5%)

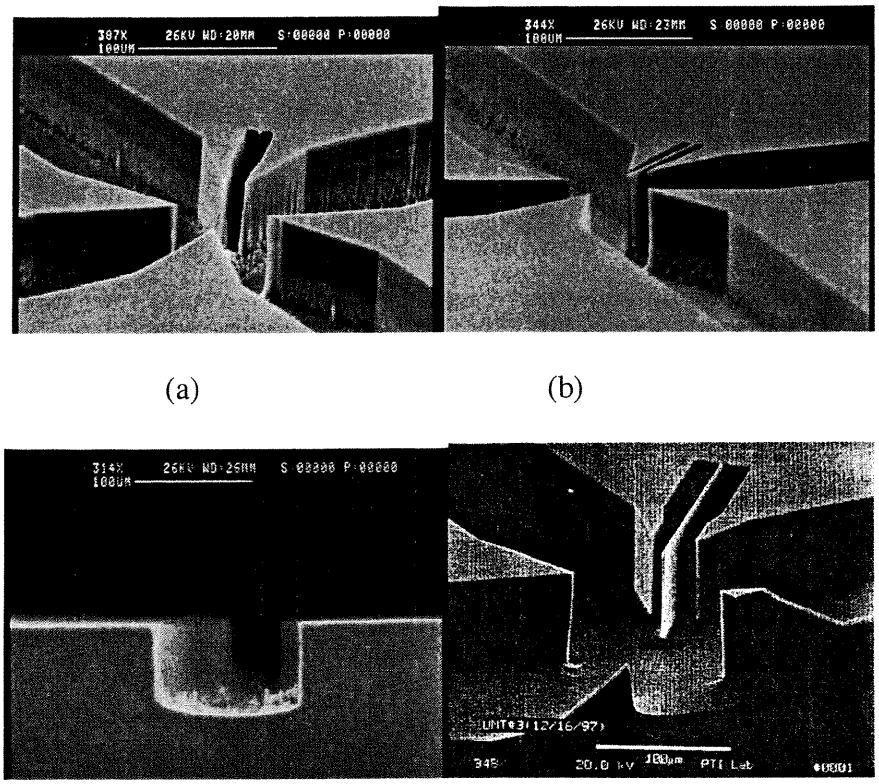

(a) (b)

(c) (d)

Figure 3.14 Etching uniformity experimental results: (a) trenches at passivation time of 3 seconds; (b) trenches at passivation time of 4 seconds; (c)trench bottom cross section view; and (d) optimal trench etch results at passivation time of 5 seconds.

3.3 Processing Summary

To optimize the deep etching processing, various experiments have been carried out for development including: using photoresist as deep etching masking material, balanced designing the open trenches (protection walls), and modification of Bosch process.

The processing parameters of modified Bosch as discussed in the previous section is summarized in Table 3.2.

Table 3.2 The Parameters of Modified Bosch Processing (Argon 40 sccm).

	Step 1	Step 2	Step3
Etching/passivation Time	5 seconds	4 seconds	3 seconds
Gas Flow	C_4H_8 70 sccm SF_6 0.5 sccm	C_4H_8 0.5 sccm SF_6 50 sccm	C_4H_8 0.5 sccm SF_6 100 sccm
Pressure	23 mTorr	23 mTorr	23 mTorr
DC Bias	6 W	60 W	60 W
RF Power	RF1: 1 W RF2: 825 W	RF1: 9 W RF2: 825 W	RF1: 9 W RF2: 825 W

4. CHIP LEVEL PERFORMANCE CHARACTERIZATION

In this section some device performance testing at chip level, i.e., testing the mirror and actuator performance, are carried out, respectively.

4.1 Micro-mirror Surface Roughness – AFM

A surface roughness measurement of the mirror is critical to the switch design because it has direct impact on light reflectivity and scattering. Light scattering or interferometer method has been used to determine roughness with sub-nanometer height precision; however, lateral resolution has been limited to the micron scale with these methods. The invention of the atomic force microscopy (AFM) in 1986[23] provide a new high resolution profilometry tool to access lateral dimensions down to the nanometer scale, with atomic resolution reported [24]. The principle of AFM involves tracing the sample topography with a sharp stylus and generating a three-dimensional topographic map of the surface, with resolution primarily limited by the diameter of the stylus tip.

4.1.1 *Experimental*

The sample used for AFM measurement is prepared by deep trench etching developed in section3. In order to get the data as close to the real switching-mode situation as possible, the silicon is etched down to 75 μm deep. The protection

wall late is etched away so that the mirror sidewall can be exposed for AFM measurements.

AFM is measured with contact mode. Digital Instruments Multimode Microscope systems are available that can perform AFM or STM. NanoScope III controllers, controlled by 486 PC and digital signal processor, are used to run the microscopes. The microscopes have Angstrom level lateral resolution and sub-Angstrom level vertical resolution and are capable of scanning areas as large as 150 x 150 μm with a vertical range of 5 μm. Figure 3.15 is the schematic drawing of the AFM measurement setup. The difficulty for this setup is that the measurement area is very limited and the cantilever tip has to be adjusted so that the light from laser source incident onto the cantilever tip and then reflected off from the tip back to the detector. Figure 3.16 shows laser beam hit on the cantilever tip in contact mode measurement.

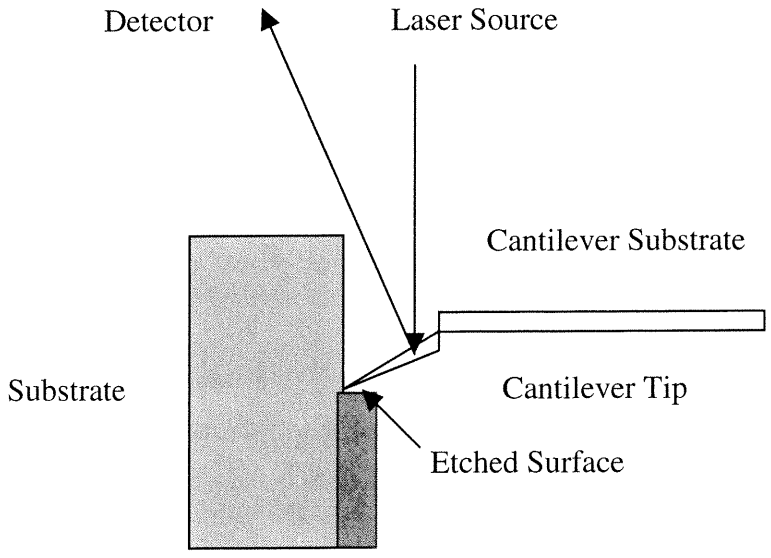

Figure 3.15 Schematic drawing of the AFM measurements.

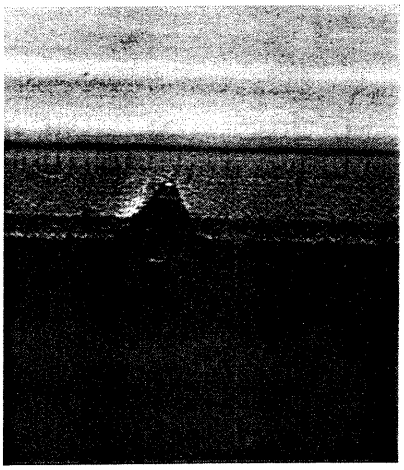

Figure 3.16 Laser beam reflected off cantilever tip in contact mode measurements.

4.1.2 *Results and discussions*

Figure 3.17 is the mirror surface measured by AFM. Very clear etching and passivation cycles can be observed that is introduced during deep etching, which is the main cause of the surface roughness. Figure 3.18 is the 3-D view of the measured AFM surface roughness. Besides the etch/passivation cycle, several strips are also observed from this photo. Those vertical strips are probably caused during photolithography processing. Figure 3.19 gives out the SEM photo of the etched sidewall which shows the more clear vertical strips. Figure 3.20 is the section analysis of the roughness. In an area of 10 x 10 μm^2, the measured roughness (RMS) is 15 nm. The arrow in the diagram shows the peak to peak distance. The calculation curves also show an notable etch/passivation cycle period.

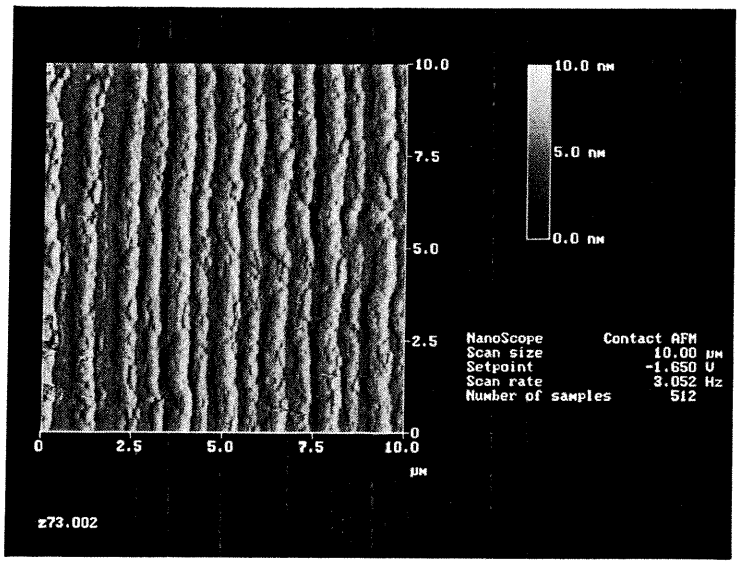

Figure 3.17 The mirror etch/passivation cycle (Passivation time: 5 ms; Etching cycles: 4 ms and 3 ms).

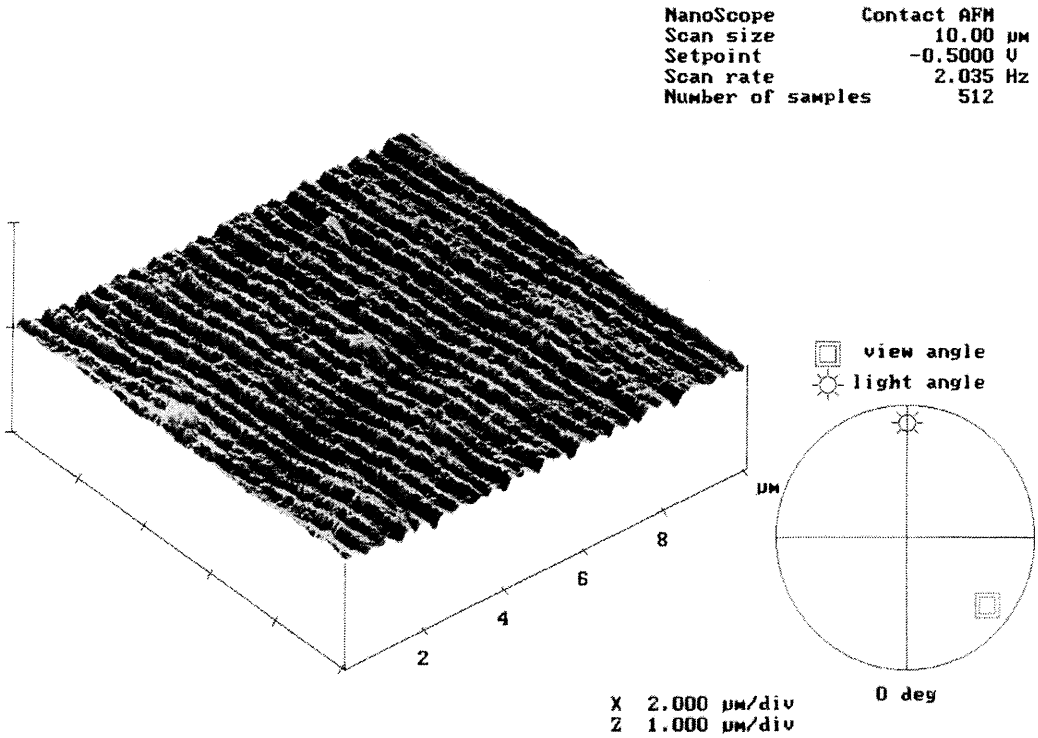

Figure 3.18 The roughness measurement result (Passivation time: 5 ms; Etching cycles: 4 ms and 3 ms).

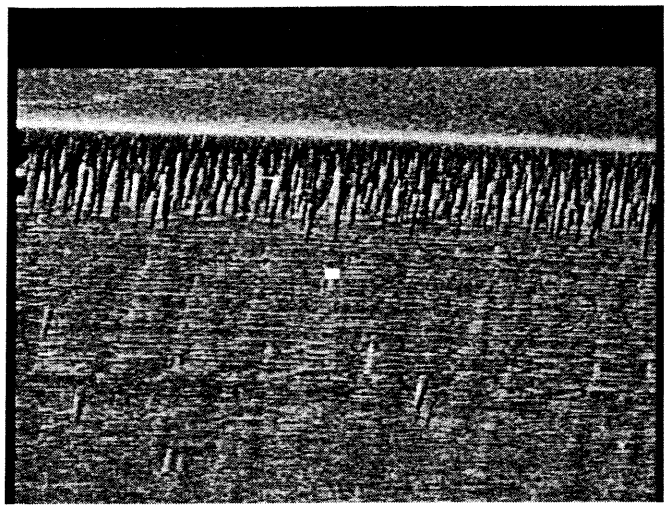

Figure 3.19 SEM of the etched sidewall (Passivation time: 5 ms; Etching cycles: 4 ms and 3 ms).

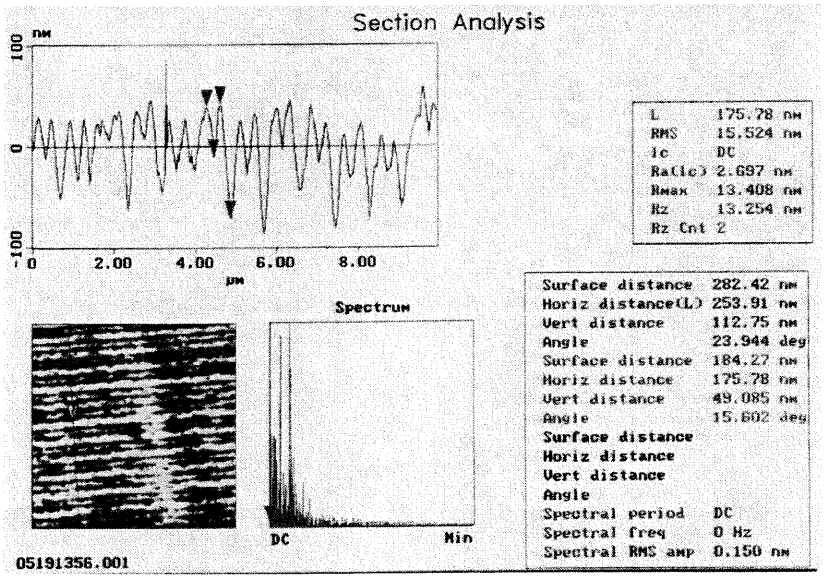

Figure 3.20 The section analysis of the surface roughness (Passivation time: 5 ms; Etching cycles: 4 ms and 3 ms).

Figure 3.21 is the surface profile that shows both the etch/passivation cycle and the transferred vertical strips. The vertical strips can be improved after adjusting hard bake time in photolithography processing to reduce the vertical strips transfer [25]. Figure 3.22 shows the roughness variations with different calculated area. The larger the area taken into account, the larger the RMS roughness. For instance, the RMS, which is 21 nm in an area of 10 x 10 μm^2, will increase to 35 nm when an area of 20 x 20 μm^2 is counted. Those measurements are done without any release processing involved. During structure releasing, the etching chemicals might attack the surface of the mirror. So the surface roughness variations with different release processing are also studied. Figure 3.23 is the measurement result with different release time. The HF used for release, in fact, does not attack much of the surface. With the measured area of 10 x 10 μm^2, for a release time from 10 minutes to 100 minutes, the RMS ranges from 23 nm to 27 nm.

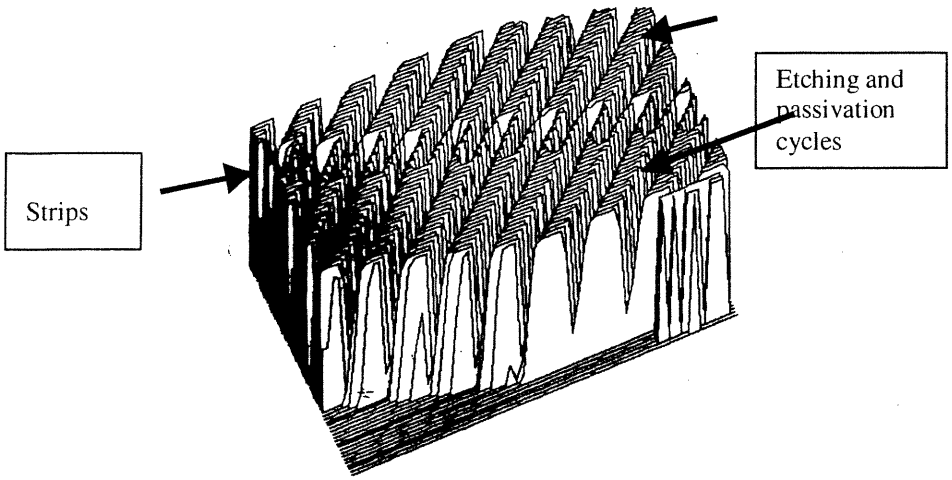

Figure 3.21 Mirror surface profile. (Passivation time: 5 ms; Etching cycles: 4 ms and 3 ms).

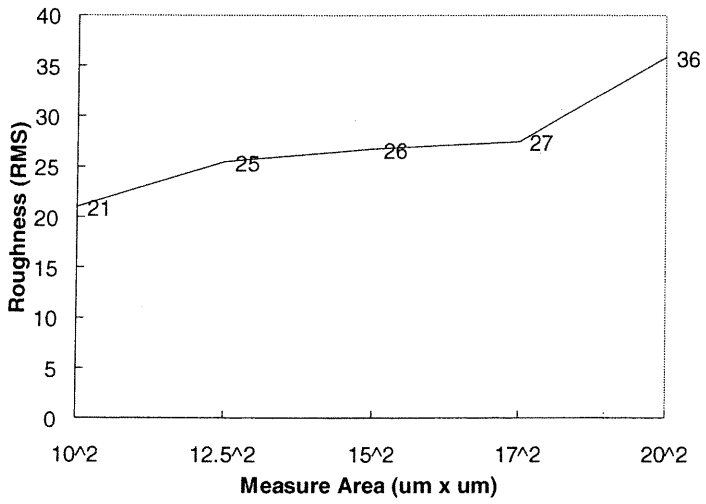

Figure 3.22 The roughness varies with calculated area (Etching time: 20 minutes).

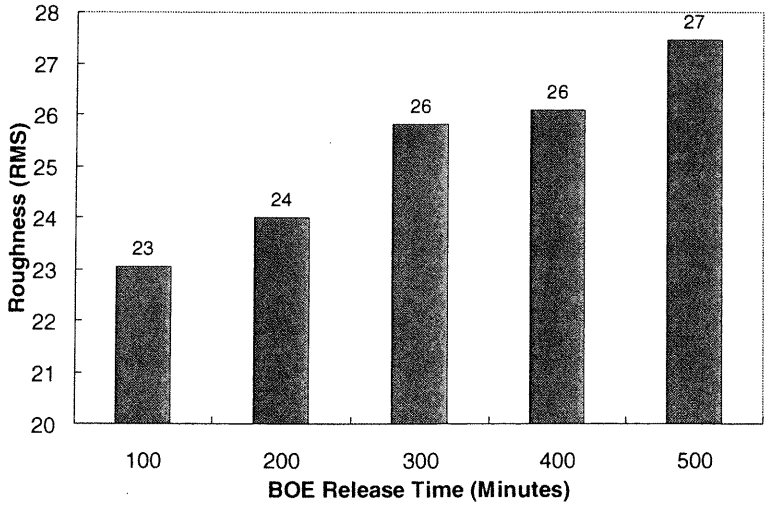

Figure 3.23 The roughness varies with structure release time (Measured area: 10 μm^2).

Figure 3.24 is scattered light at 1300 nm as a function of surface roughness[26]. The light loss maintains less than 0.1 dB (light scattered 2.9 %) when the roughness is around 20 nm. The loss will go up dramatically after the roughness is over 40 nm at 1300 nm wavelength. Therefore, a roughness of 30 nm or less is preferred for operating wavelength of 1300 nm.

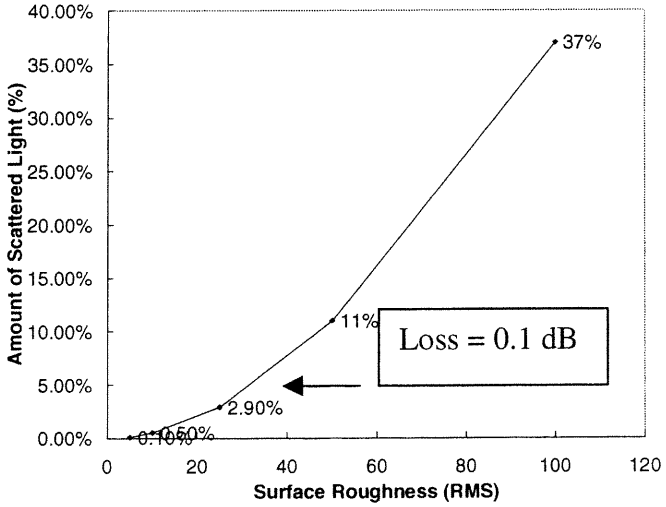

Figure 3.24 The light loss varies with surface roughness calculated at 1300 nm.

4.2 Actuation Testing

The displacements as a function of driving voltages are measured to compare with ANSYS simulation results.

4.2.1 *Experimental setup*

The testing equipment used is the Signature Probe Station (Figure 3.25). The chip is mounted on the sample stage by vacuum. Two probes touches two electrode pads of the chip, one is grounded, and another is connected with signal in. Hewlett Packard E 3615 0.25 A DC Power Supply is used to ramp up voltage from 0 to 120 Volt. MicroZoom II High Performance Microscope is used to capture micro images. A scaled objective lens is used to measure the displacement. For fast switching frequency response, an AC pulse generator simply replace the DC power supply.

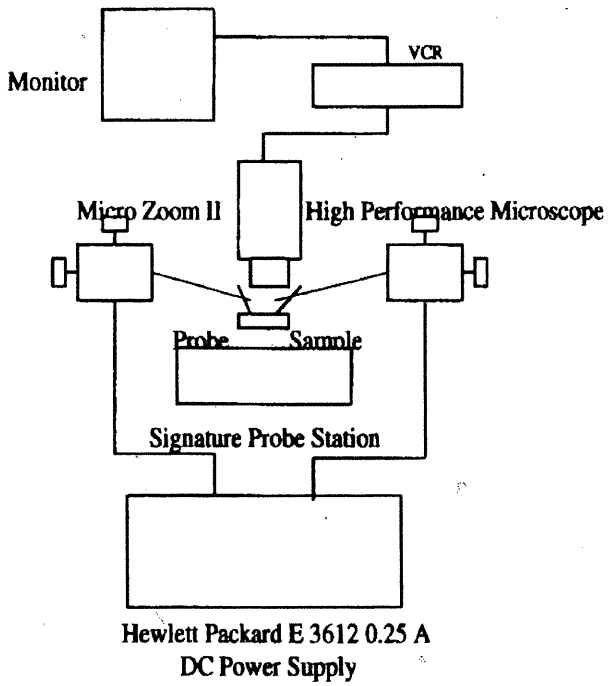

Figure 3.25 The actuation testing equipment setup.

4.2.2 *Testing results*

Figure 3.26 is the actuation measurement results for different actuator designs. The measurements demonstrates that narrowing the beam width will drastically increase the displacement (comparing D14 and D5); the longer the beam length the larger the displacement is (comparing D4 and D14); and the finger gap will reduce the driving voltage requirement for a larger displacement (comparing D14 and D1).

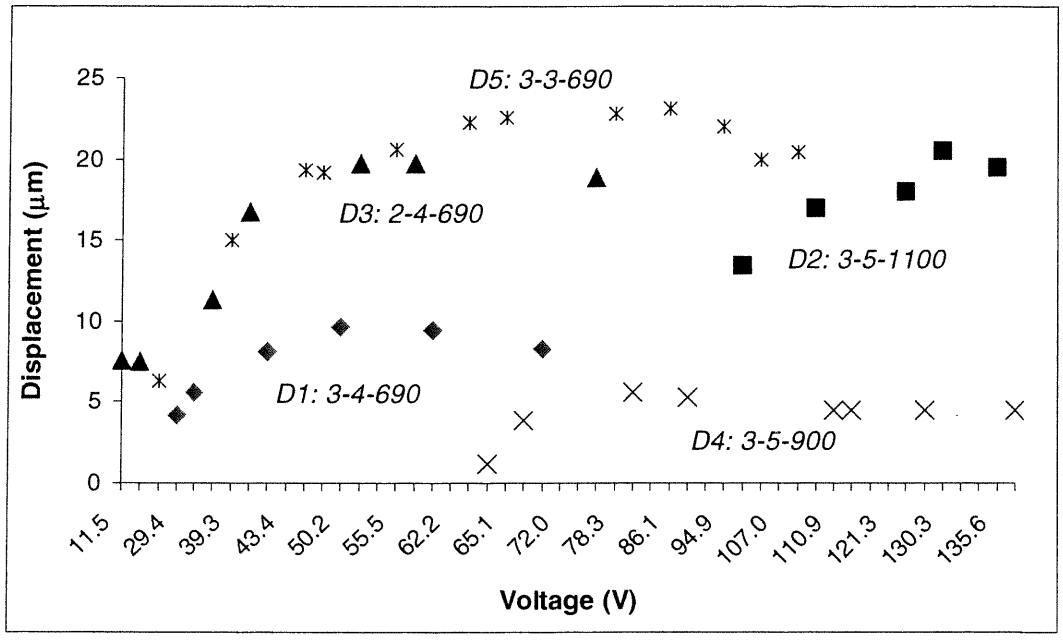

Figure 3.26 Actuation testing results with different designs (for gap=3 μm: D1: BW =4 μm, BL= 690 μm, FN=140; D5: BW=3 μm, BL= 690 μm, FN=140; D2: BW= 5 μm, BL= 1100 μm, FN=140; D4: BW= 5 μm, BL = 900 μm, FN=140; and for gap=2μm: D3 other parameters are same to D14).

The comparisons between experimental data, ANSYS simulations and theoretical calculations are described in Figure 3.27. The tested actuator starts to move when 6 volts are applied. The maximum displacement of 55 μm is achieved when 60 volts are applied. The ANSYS simulations represent well the actual testing results in comparison to theoretical calculations.

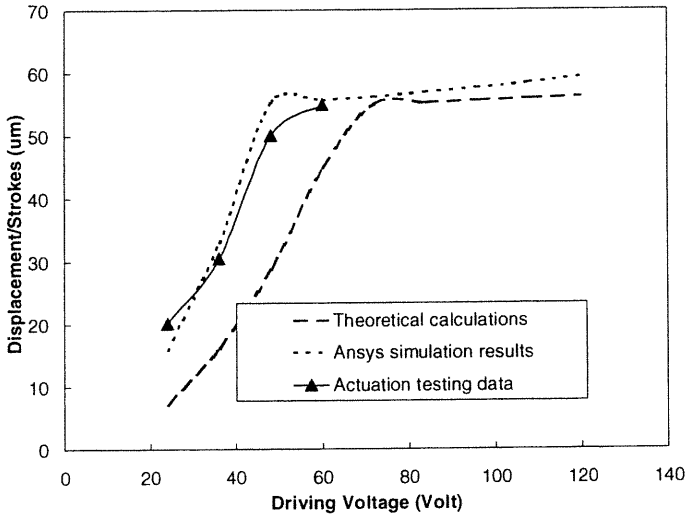

Figure 3.27 Comparisons between experimental data and ANSYS simulations (BW= 3 μm, BL=1000 μm, FG= 3 μm, and FN= 140).

5. SUMMARY AND DISCUSSIONS

The 2 x 2 switching chip is fabricated with SOI wafers by bulk micro-machining technology. The diced chip size is 8 x 8 mm, including electrostatic comb actuator, four built-in alignment grooves, electrode pads and micro-mirrors. Deep ICP etching is extensively studied to assure high quality etching results. The mirror verticality

can be 90 ° ± 0.1°, and roughness is less than 30 nm. After design optimization, the final 2 x 2 design parameters are listed in Table 3.3. The actuator testing shows that the displacement of 55 μm can be obtained when 60 volts are applied. A displacement of 55 μm driving at 40 volts is observed in the experiments.

Table 3.3 Optimized chip design, fabrication and testing results.

Chip dimension	8 x 8 mm
Alignment groove dimension	Width: 128 μm, length: 4000 μm
Mirror dimension	120 x 75 x 5 μm
Actuator parameters	Refers to Table 2.11
Maximum displacement	55 μm
Roughness	Less than 20 nm
Driving voltage	40 volts (minimum)

In addition, stability is another key characteristic to evaluate the actuator performance. As observed through the actuation testing, the actuator with smaller gap is more likely to be unstable and fail to operate with smaller displacement. Here," unstable" means the situation in which the teeth of the electrode move in the direction perpendicular to the stroke direction and touch the stationary electrode [26]. In this case, a short-circuit occurs and the actuator stops operating. See Appendix A for detail theoretical consideration on the comb actuator stability. From Appendix A, it is apparent that limiting the maximum applied voltage is quite important. Also, it

is important to reduce the overlap length. Hence, it is advantageous to design initial overlap length as small as possible to get a long stroke. Obviously, increasing the spring constant of the suspension k_y is the most effective way to stabilize the actuator. The ideal suspension is the suspension with a low k_x and at the same time with quite high k_y.

REFERENCES:

1 **Howe, R.T.**, **Boser, B.E.**, **Pisano, A.P.,** *Polysilison Integrated Microsystems: Technologies and Applications* Sensors Actuators, (1996), A 56, 167-77.

2 **Linder, C., Paratte, L.**, *Surface Micromachining* J. Micromech. Microeng., (1992), 2, 122-32.

3 **Kloeck, B.**, *Design, Fabrication and Characterisation of Piezoresistive Pressure Sensors, Including the Study of Electrochamical Etch Stop* , PhD Dissertation University of Neuchatel, (1989).

4 **Buser, R.A.**, *Theoretical and Experimental Investigations on Silicon Single Crystal Resonant Structures*, PhD Dissertation University of Neuchatel.

5 **Tschan, T.**, *Simulation, Design and Characterization of Silicon Piezoresistive Accerometer, Fabricated by a Bipolar-compatible Industrial Process*, PhD Dissertation University of Neuchatel, (1992).

6 **Muller, R.S., Howe, R.T.,** *Microsensors*, (1991) (New York: IEEE)

7 **Gardner, J.W.**, *Microsensors: Principles and Applications* , (1994) (Chichester: Wiley).

8 **Sze S.M.**, *Semiconductor Sensors* (1994) (New York: Wiley)

9 **Bau, H.H. de Rooij, N.F., Kloeck, B.**, *Mechanical Sensors* (Sensors-a Comprehensive Survey 7) (1994) (Weinheim).

10 **Ristic, L.,** *Sensors Technology and Devices*, (Boston: Artech)

11 **Linder, C., Tschan, T., de Rooij, N.F.,** *Deep Dry Etching of Silicon:* a Novel Micromachining Tool , Sensors Mater., (1992), 3, 311-24.

12 **Lee, K.Y., LaBianca, H., Rishton, S.A.**, *Micromachining Applications of a High Resolution Ultrathick Photoresist,* J. Vac. Sci. Technol., (1995), B13, 3012-6.

13 **Esashi, M.** *High-rate directional Deep Dry Etching for Bulk Silicon Micromachining*, J. Micromech. Mircoeng., (1995), 5, 5-10.

14 **Jansen, H., de Boer, M., Elwenspoek, M.**, *The Black Silicon Method VI: High Aspect Ration Trench Etching for MEMS Applications*, Proc. 9th IEEE Workshop on MicroElectro Mechanical Systems, MEMS'96 (San Diego, CA, 1996), 250-7.

15 **Zhang, N.**, *Method of Etching a Wafer Layer Using Multiple Layers of the Same Photoresistant Material and Structure Formed Thereby*, S/N 09/372,428.

16 **Linder, C., Tschan, T., de Rooij, N.F.**, *Deep Dry Etching Techniques as a New IC Compatible Tool for Silicon Mircomachining,* Proc. Int Conf Solid State Sensors and Actuators TR (1991), 524-527.

17 **McVittie, J.P., Gonzalez,C.**,*Anistropic Etching of Si Using SF_6 with C_2ClF_5 and Other Mixed Halocarbons*, Proc 5th Symp Plasma Processing-Electrochem Soc, (1985) 85-1, 552-567.

18 **Bhardwaj,** J.K., **Ashraf**, H., Advanced Silicon Etching Using High Density Plasma, Proc SPIE, 2639, (1998), 224-233.

19 **US Patenet #5501893:** *Method of Anisotropically Etching Silicon.*

20 **Temermeister, I., Blayo, N., Klemens, F.P.**, *Comparison of advanced*

plasma sources for etching applications, J. Vac. Sci. Technol. B 12(4), (1994), 2310-2321.

21 **Coburn, J.W., Winters H.F.**, *Conductance considerations in the reactive ion etching of high aspect ratio features*, Appl. Phys. Lett. 55(26), (1989), 2730-2732.

22 **Zhang**, N, *Method of Etching a Wafer Layer Using a Sacrificial Wall and Structure Formed Thereby*, U.S. Patent Application S/N 09/372,700.

23 **Binnig, G., Quate, C.F.**, *Gerber,C., Phys.Rev.Lett.,* 56, (1986), 930.

24 **Ohnesorage, F., Binnig, G.,** Science, 260, (1993), 1451.

25 **Pang**, C., *Dry Etching*, Short course at SPIE micromachining, 1999.

26 **Hirano,H.**, **Furuhata, T.**, **Gabriel, K.J.**, *Design, fabrication, and operation of submicron gap comb-drive microactuators,*J. Microelectromechanical system, 1(1), (1992), 52-58.

CHAPTER 4 : EFFICIENT COUPLING BETWEEN SINGLE-MODE FIBERS WITH TAPERED HEMISPHERE ENDS

1. INTRODUCTION

Single mode fiber has a small core size on the order of 5-10 μm. A switch constructed using single mode fibers, where two cores or light source and core have to be aligned, is inherently very sensitive to axial and transversal (lateral) displacements; these displacements can be induced mechanically or thermally. These problems can be greatly alleviated, if not theoretically eliminated, by the introduction of beam expansion optics. In this approach, components, which could consists of spherical lenses[1-2], Grin lenses[3], cylindrical lenses [4], and combinations thereof [5], are used to increase the single-mode spot size and thus reduce sensitivity to alignment. These discrete elements, however, introduce problems of their own. They require critical and difficult alignment, which must remain stable, and in addition they possess aberrations which limit performance[6]. Moreover, for MOEMS switch application, the beam diameter of the conventional micro ball lens and collimators are all larger than 50 μm, which is not small enough to suit micro-mirror design needs. One exception is that by utilizing the built-on-chip silicon or silica waveguide expander, a 30 μm beam spot can be achieved[7] at 1310 nm. This element is highly wavelength dependent with high loss because it uses optical diffraction mechanisms and it is not suitable to be used in the interconnection of DWDM network.

Tapered fibers have frequently been used for the interconnection of optical waveguide communications. One example is coupling laser diode output into a single mode fiber[8-13]. This coupling technique is attractive because of the relative ease of tapered fiber fabrication, reasonable coupling efficiency and relatively reduced influence of reflective light. A method for obtaining the tapered region by etching has been reported[14]. However, the etching process uses HF solution and is troublesome. Moreover, the etching process makes the fiber fragile [15]. By using a simple, robust splicing process technique a tapered fiber with a hemispherical lens (TH fiber) has been developed with good reproducibility. To our knowledge, this is the first use of TH fiber in an optical switch module.

For switching applications, the followings are criteria for the TH fiber performance. First of all, the coupling efficiency has to be high and coupling loss has to be low, while maintaining a reasonable return loss. Secondly, the optimized separation, that is the distance between the launching and receiving fiber where the coupling loss is minimum, has to be in a workable range for assembly (This range is specified as 50 microns to 200 microns taking the switch design into account). Lesser distances will be hard for assembly (easily damaging lens and mirror), too long a distance will cause material waste and additional insertion loss. Thirdly, the beam focus diameter created by TH fiber must be smaller than 30 μm so that there is no light scattering and crosstalk due to light striking the edge of the mirror or passing over it. Lastly, the TH fiber has to be tolerant to misalignment during assembly processing.

In section 4.2, the TH fiber fabrication, reproducibility control and measurements are described. In section 4.3, light propagation and beam profile (light intensity distribution) are investigated with theoretical simulations compared to experimental data. Measurements of coupling scheme and coupling loss with different TH fibers are carried out experimentally. Furthermore, the alignment tolerance issues on TH fibers are studied and some comparisons are made. Conclusions about the TH fiber are given in section 4.

2. TH FIBER PROCESSING

The fabrication process developed with Vytran machine for TH fiber is rather simple, however, controlling the process to achieve a consistent product needs extensive research. In this section, the TH fiber fabrication sequence is described and TH fiber dimensions are measured for a better control of fabrication parameters in the processing. The reproducibility is studied and some results are reviewed.

2.1 Fabrication Sequences

The equipment to fabricate the TH fiber is Vytran FFS-2000 Automated Fusion Splicing Workstation with advanced imaging capabilities and programming flexibility. It consists of a soaking station (solvent pre-soak station available for "hard" coating), a coating stripper (thermal mechanical stripping process for high strength coating removal), a fiber cleaner (ultrasonic cleaning maintains fiber strength) and a fiber cleaver (tension & scribe method with automated diamond cleaving wheel).

Table 4.1 lists the steps for the fabrication sequences. The method is using filament of 0.23 x 0.15 inch to fuse the fibers. Alignment is done automatically by true core imaging. Stepper motors control the X-Y fiber position with resolution of 0.01 μm, and Z fiber feed resolution of 0.125 μm.

Table 4.1 TH fiber fabrication sequences.

Number	Steps	Method
1	Coating Removal	Thermal Stripper
2	Cleaving	Tension and Scribe
3	Cleaning	Acetone with ultrasonic
4	Alignment	X-Y alignment mechanism
5	Splicing	Fusion technique
6	Tapering	Filament heating and pull
7	Lensing	Setback and heat

The single-mode fibers used for tapering are Corning's SMF-28^{TM} manufactured using the Outside Vapor Deposition (OVD) process, which produce a totally synthetic, ultra-pure fiber. The parameters are listed in Table 4.2 for later references. The tapered fiber is fabricated by splicing two single-mode (SM) fibers first, then drawing the spliced fiber within the heated filament. Finally the tapered fiber is setback to the filament and heated at certain temperature. The hemispherical tip of the fiber is formed by the surface tension of the molten glass. The tip of the TH fiber is covered with cladding glass. To optimizing the TH fiber for high efficient coupling in a desirable

coupling range, TH fibers with varying shapes and geometry have been examined by running different scrip files programmed for tapering and lensing processing. With those programs, the tapers have been fabricated with different lengths, drawing angles and lens of different radii.

In Figure 4.1, the right photo is a typical TH fiber, while the left photo shows the tapering fiber before finished up with lens. Heating and pulling fibers with certain speed, distance and time can control the taper geometry. Figure 4.2 presents a typical variation of the taper diameter and angle as a function of taper length as measured by Vytran machine. First the image is taken on screen by Vytran advanced image capture

Table 4.2 SMF-28^{TM} parameters.

Core Diameter	8.3 μm
Cladding diameter	125.0 ± 1.0 μm
Core-Clad Concentricity	≤ 0.5 μm
Cladding Non-Circularity*	≤1.0 %
Numerical Aperture	0.13
Refractive Index Difference	0.36%
Cutoff Wavelength	< 1260 nm
Mode-Field Diameter	8.0 to 9.80 μm at 1310 nm; 9.50 to 11.50 at 1550 nm

* Defined as: $\left[1-\frac{Min.CladdingDiameter}{Max.CladdingDiameter}\right]\times 100$

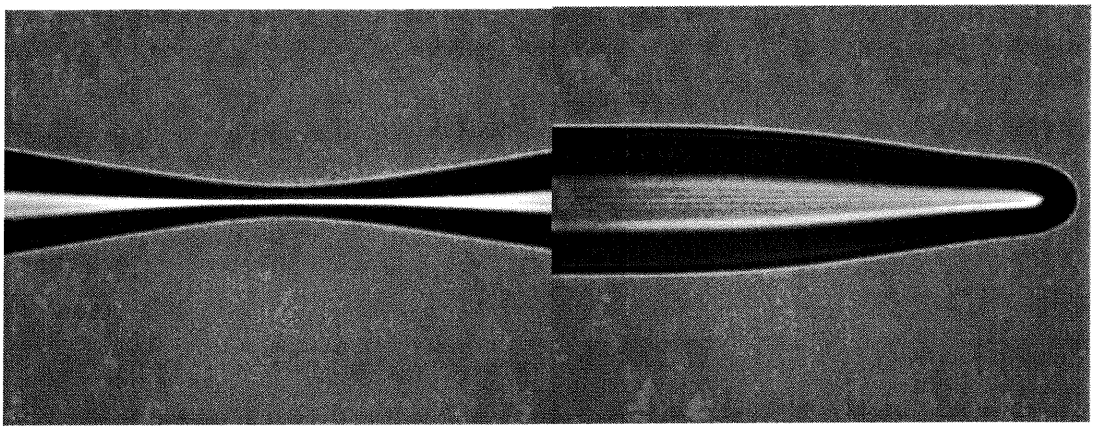

(a) (b)

Figure 4.1 TH fiber: (a) during tapering; (b) finish with hemisphere lens.

system, then the dimensions are measured by counting the CCD pixel on screen. The calibration value for each pixel is: *Px=0.66 μm, Py=0.61μm*. For the TH fiber in Figure 4.1, the taper length is 458 μm, and the narrowest core radius measured is 4 μm. The taper outer-cladding pulling angle is 16.2°. Figure 4.2 (a) presents a clear taper shape in comparison to the core diameters in Figure 4.2(b) which shows some errors along the line. This is because the core image on screen does not have a clear edge definition and that will result in the measurement errors shown on the curve. Figure 4.2(c) illustrates that in the tapered region the core and cladding thickness decrease in a very consistent ratio. Again, the errors shown are brought in by core diameter measurements.

Figure 4.3 shows the radius as a function of filament power. Increasing the power leads to the larger lens radii due to the more molten materials for lens formation. Likewise, the more setback steps, the larger the lens radius. However, at certain power

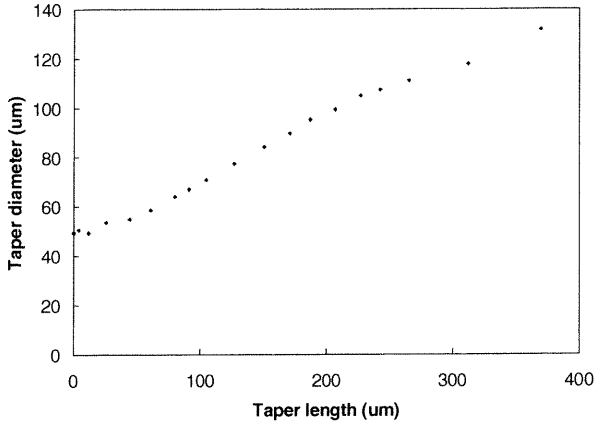

(a)

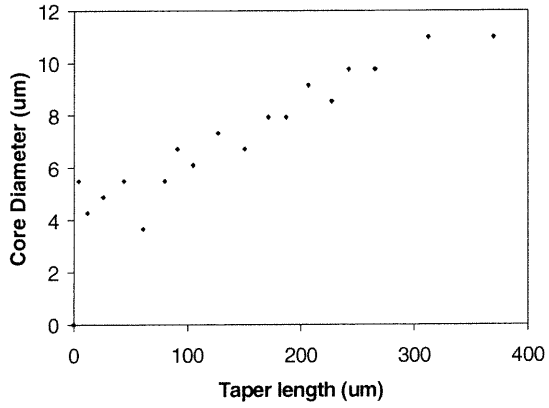

(b)

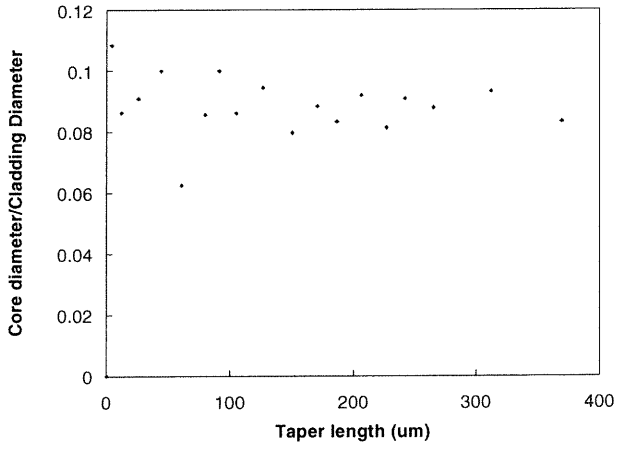

(c)

Figure 4.2 Tapered fiber dimension measurements: (a) cladding diameter vs. taper length; (b) core diameter vs. taper length; (c) pulling ratio of core and cladding.

, the setback steps are limited, which means the lens diameter will not increase anymore when setback steps reach to certain amount under this power. This is because filament will not be able to melt anymore materials to form lens with larger diameter. Curve (a) in Figure 4.3 presents this saturation phenomenon. The range of curvature radius extends from 23 μm to 56 μm with the increasing setback steps up to 1800. Figure 4.4 is one of the lens shapes measured on Vytran machine. The lens radius is about 48 μm.

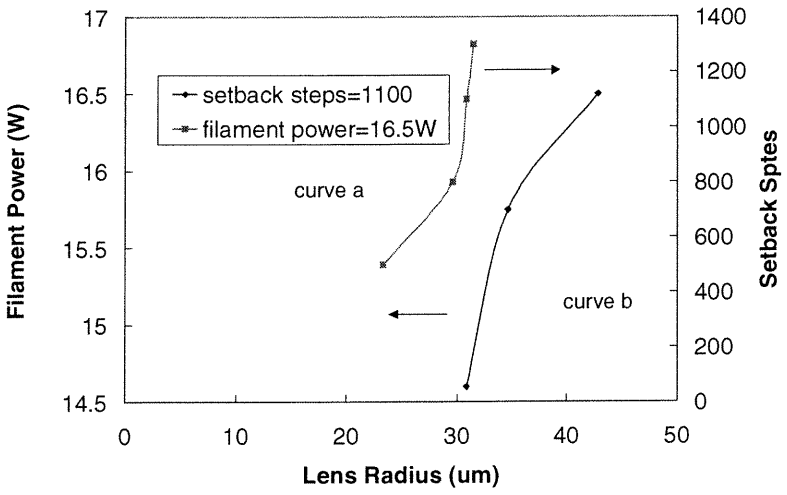

Figure 4.3 Lens radius vs. filament power/setback steps. Curve (a) is the lens radius as a function of setback steps at filament = 16.5 W; Curve (b) is the lens radius as a function of filament power where setback steps = 1100.

With the processing programs for splicing, tapering and lensing, and using Vytran machine the tapers have been obtained with the length from 100 μm to 500 μm, the drawing angles from 30° to a small angle of less than 10°, and lens radius from 23 μm to 56 μm Table III lists the various lenses fabricated under different lens finish conditions.

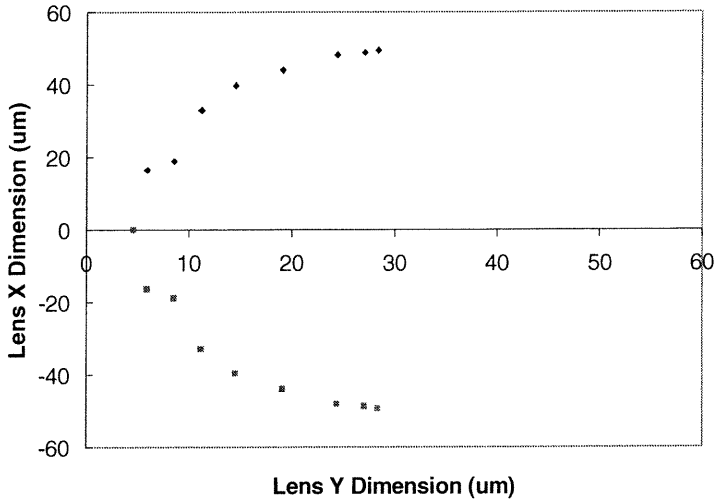

Figure 4.4 Hemisphere lens shape measured with Vytran machine.

Table 4.3 The various lens finish conditions and corresponding lens diameters.

Groups	Power (W)	Setback Steps	Lens Diameter (μm)
I	14.6	1300	31.5
	14.6	1100	30.87
	14.6	800	29.61
	14.6	500	23.31
II	16.5	1100	42.84
	16.5	1500	46.62
	16.5	1700	49.14
	16.5	1800	50.4
III	14.6	1100	30.87
	15.75	1100	34.65
	16.5	1100	42.84
IV	15.75	1500	50.00
	16.5	1500	46.62
	17	1500	55.44

2.2 Reproducibility

Both the radius of the end hemisphere and pulling taper dimensions are highly reproducible if the conditions maintain constant, such as filament dimension, feed back steps, and heat power. The TH fiber dimensions are measured under one control condition, that is using the same splicing, tapering and lensing program. The dimension variations are given out in Figure 4.5. The tolerance for lens radius is 1 μm, and the tolerance for taper length is about 16 μm.

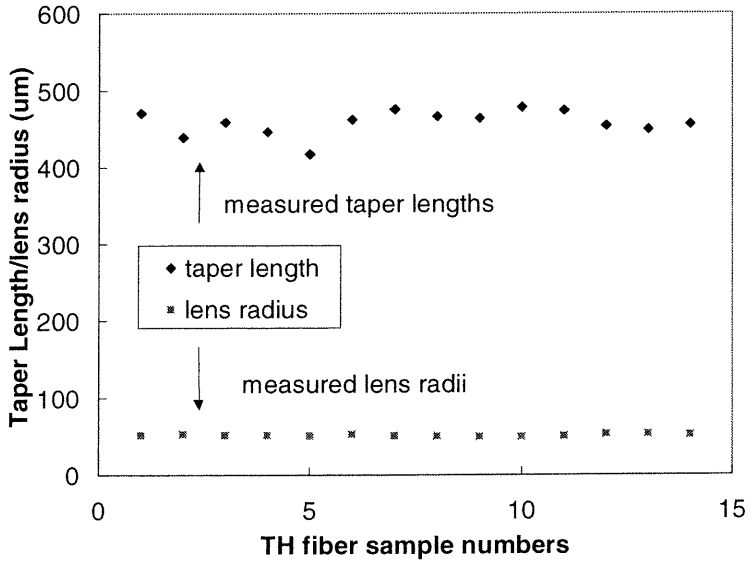

Figure 4.5 Geometry reproducibility of TH Fibers.

Another fact that will influence the TH fiber reproducibility is the shape of filament. The filament position, dimension and shape play an important role for TH fiber processing controlling. If the filament does not centralize in the fusion area, the right TH fiber will have different geometry (lens radius, taper length, etc.) from the left one. That is because the offset of the heating zone will provide an uneven heating for the right and

left fiber during pulling and lens finishing. Whenever a new filament is installed, careful adjustments of the filament to the center of the heating zone is an essential part of the tapering procedures. Meanwhile, if the filament does not have a good symmetrical round shape, the TH fiber will have perturbations along its length that could give rise to mode coupling between the core and cladding and result in additional losses.

Coupling losses with different filaments are measured. Corresponding filaments are shown in Figure 4.6 (a) and (b). TH fibers that are fabricated with # 3 filament have higher losses comparing with those by # 4 filament (see Figure 4.7). Figure 4.6 (a) and (b) show that the # 4 filament holds an almost perfect round shape, while # 3 has some distortions along its round shape. This distortion will create the perturbations along the tapered fiber and lead to the mode couplings. This is the reason that the TH fibers fabricated by filament #3 generally suffer more losses during coupling measurements (Figure 4.7). The coupling measurement setup and experiments will be discussed in section 3.

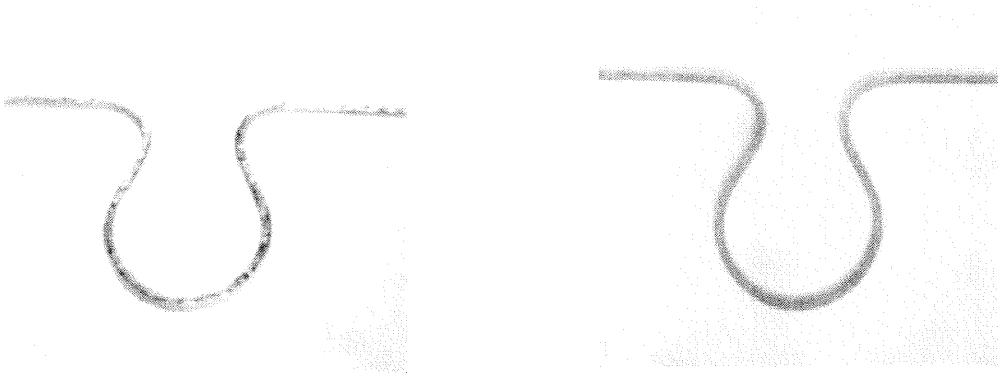

(a) (b)

Figure 4.6 Slight different shape of filament: (a) filament #3; (b) filament #4.

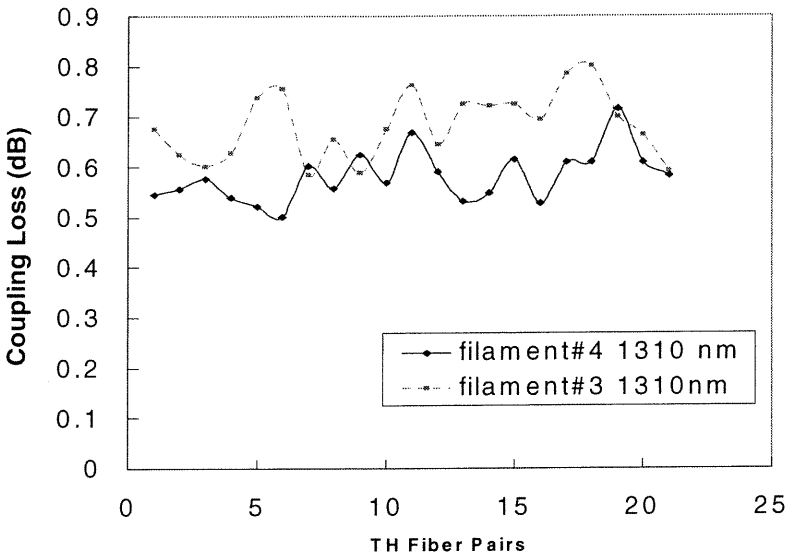

Figure 4.7 The coupling loss of Th fiber fabricated with filament #3 and #4.

Figure 4.7 also shows that some fluctuations occurred using the same filament on different fiber pairs. This is because even with the same filament, an adjustment period is needed to set the filament right in the center heating position. During this adjustment processing, the right and the left TH fiber could be finished unevenly that result in slightly different lens radius and core diameter, and thus coupling loss measurement will be different.

3. LIGHT PROPAGATION AND COUPLING WITH TH FIBERS

In this section, the light propagation and coupling issues associated with TH fibers are studied. First, the transmissions and distributions of the beam in free space after leaving a TH fiber will be discussed, and then the beam profile in free space will be measured to compare with theoretical calculation. Second, the beam properties in

tapered region are studied, as well as the lens effect on the beam transformation. The measurements with different lens radii are carried out to verify the theoretical predictions. Finally, the TH fiber coupling scheme is given with the discussions of the coupling efficiency and misalignment tolerance.

3.1 Light Propagation in Free Space

3.1.1 *Gaussian beams*

Let us assume that we have somehow generated a light beam with Gaussian intensity distribution that happens to have a plane phase front at the plane $z=0$. This light can be described by the equation

$$\varphi(x, y,0) = Ae^{-(x^2+y^2)/\omega_0^2} \tag{4.1}$$

The parameter ω_0 is the beam half width at $z = 0$. It is the distance from the peak of the field distribution at which the function decays to $1/e$ of its maximum value.

The field at any given distance z can be written as [16]

$$\psi(x', y', z) = \frac{2i\pi\omega_0^2}{\lambda(2z + ik\omega_0^2)^2} Ae^{-ikz} \exp\left[-i\frac{2kzir'^2}{4z^2 + (k\omega_0^2)}\right] \exp\left[-\frac{(k\omega_0 r')^2}{4z^2 + (k\omega_0^2)^2}\right] \tag{4.2}$$

with

$$r'^2 = x'^2 + y'^2$$

Where $k=2\pi/\lambda$, and λ is the wavelength of the propagation media. The first exponential factor describes the phase of a plane wave. The second exponential factor is responsible for phase front curvature. The last exponential factor determines the field intensity in transverse direction.

We introduce the beam width parameter again by the definition that it is equal to the distance (in transverse direction) at which the field amplitude decays to *1/e* of its maximum value. The square of the beam half width is thus given by

$$\omega^2(z) = \omega_0^2\left[1+\left(\frac{2z}{k\omega_0^2}\right)^2\right] \tag{4.3}$$

Using $k=2\pi/\lambda$, we can write this equation also in the following form

$$\omega^2(z) = \omega_0^2\left[1+\left(\frac{\lambda z}{\pi\omega_0^2}\right)^2\right] \tag{4.4}$$

Remember that the beam at $z=0$ has a plane phase front and half width ω_0. From that point, it propagates toward increasing values of z, with an increase in its width. We could have used the diffraction integral to find the field to the left of the point $z=0$, and would have found that its behavior is exactly the same. In fact, (4.4) holds for positive as well as negative values of z, and describes the beam width throughout all space. It is thus

apparent that the point $z=0$, at which the Gaussian beam has a plane phase front, is also the point at which it assumes its narrowest half width ω_0. The minimum beam half width ω_0 is apparently arbitrary. However, the spread of the field past its narrowest point depends on the minimum beam width. We can define a half angle of the beam far from $z=0$ by the equation

$$\theta = \lim_{z\to\infty} \frac{\omega(z)}{Z}$$

This beam half angle is thus given by the expression

$$\theta = \frac{\lambda}{\pi\omega_0} \tag{4.5}$$

A Gaussian beam at a given point in space is not completely determined by its beam width alone. To describe the beam completely, we need to know one more parameter, for example, the radius of curvature of its phase front. We obtain it from the phase front curvature term of (4.2). The radius of curvature of the field can be obtained with the help of Figure 8. The phase of the wave is constant on the spherical surface. The phase shift from the curved surface to the plane that touches this surface at $r'=0$ is given by

$$kd = \frac{2kzr'^2}{4z^2 + (k\omega_0^2)^2} \tag{4.6}$$

where d is the distance between two phase front (see Figure 4.8). Using (4.6), we obtain for the radius of curvature of the Gaussian beam

$$R(z) = z\left[1+\left(\frac{\pi\omega_0^2}{\lambda z}\right)^2\right] \tag{4.7}$$

Beam width and radius of curvature of the Gaussian beam completely at a given point along the axis. Equation (4.7) holds also for positive as well as negative of z. The change of sign of $R(z)$ that occurs for a change of the z indicates the reversal of the curvature of the phase front as we pass the beam waist.

If we define the quantity

$$Z_R = \frac{\omega_0^2}{\lambda} \tag{4.8}$$

Known as the Raleigh Range [17], then (4.4) and (4.7) can be written as

$$\omega = \omega_0\sqrt{1+\left(\frac{z}{Z_R\pi}\right)^2} \tag{4.9}$$

and

$$R(z) = z\sqrt{1+\left(\frac{Z_R\pi}{z}\right)^2} \tag{4.10}$$

Raleigh Range is an important parameter for any Gaussian beam propagation. We are particularly interested in it because the larger the Raleigh Range, the longer the Gaussian Beam "collimating" range. Within this range, a quasi-collimating beam can be achieved so that the optical alignment loss could be reduced if the micro mirror is located in this

range. Therefore a Gaussian beam with a larger Raleigh Range number could give us a good alignment tolerance.

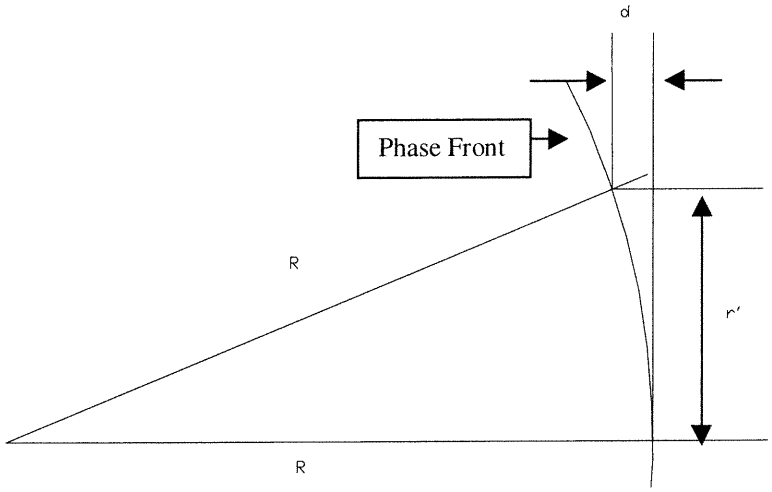

Figure 4. 8 A Spherical wave front is compared with a plane wave. The phase shift for the distance *d* between the two phase fronts is *kd*.

Through the discussions, we are using the width parameter ω of the field distribution. Experimental observations of the light field of a single-mode fiber detect the light power instead of the field intensity. The power may also be approximated by a Gaussian distribution of the form [18]

$$P = P_0 \exp(-r^2/\omega_p^2) \tag{4.11}$$

The power width parameter ω_p is related to the field intensity width parameter by the expression

$$\omega_p = \frac{\omega}{\sqrt{2}} \tag{4.12}$$

In the following experimental measurements, all the width parameters detected are power widths and are converted into field width with the above relation shown in the experimental results.

3.1.2 *TH fiber far and near-field mode measurements*

From section 3.1.1, we predict theoretically how a Gaussian beam distributes along its propagation. In this section, we measure the actual intensity distributions of the light coming from a TH fiber and traveling in a free space.

Newport PM 500 automation alignment system is used for measuring the far and near-field mode of the TH fiber. The setup is depicted on Figure 4.9. The TH fiber under measurement is driven by a x-y-z positioner and the receiving fiber is connected with a detector for data acquisitions. The laser sources are HP 1299.4 nm and 1553 nm power supply. The incident power of 1299.4 nm and 1553 nm characterized in Figure 10 will be used through the testing and measurements in this chapter. The positioner drives the testing fiber scanning at x and y direction at a step of 0.5 μm. The scanning repeats along z direction at a step of 5 μm.

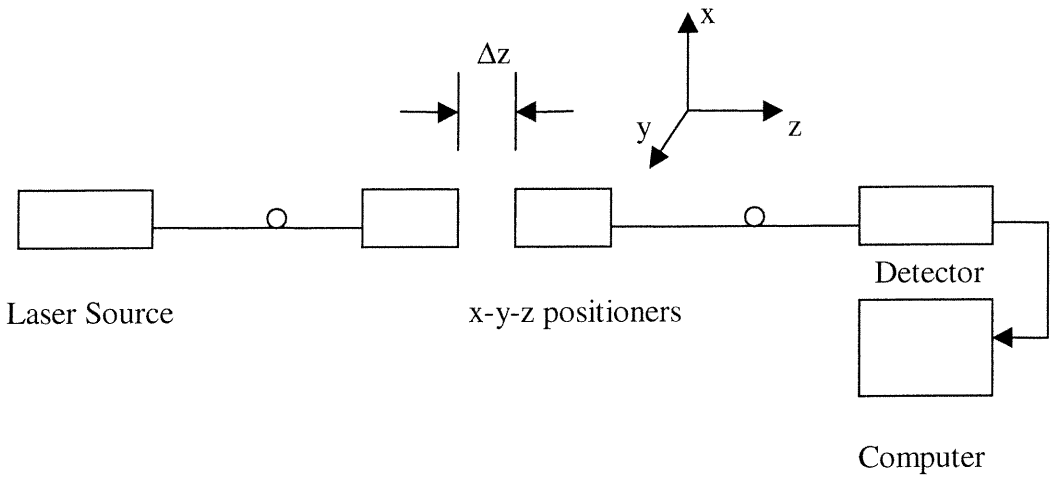

Figure 4.9 Far and Near-field mode measurement setup.

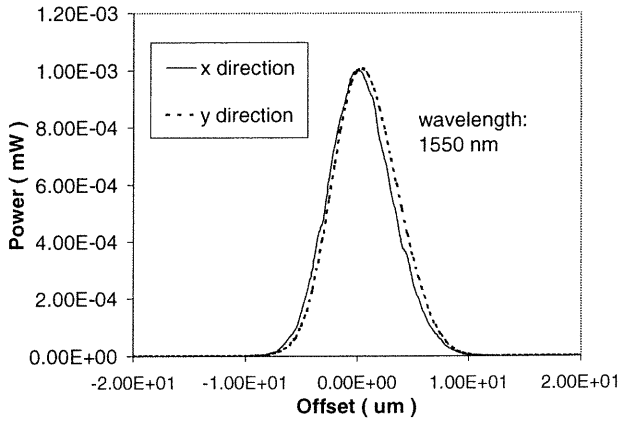

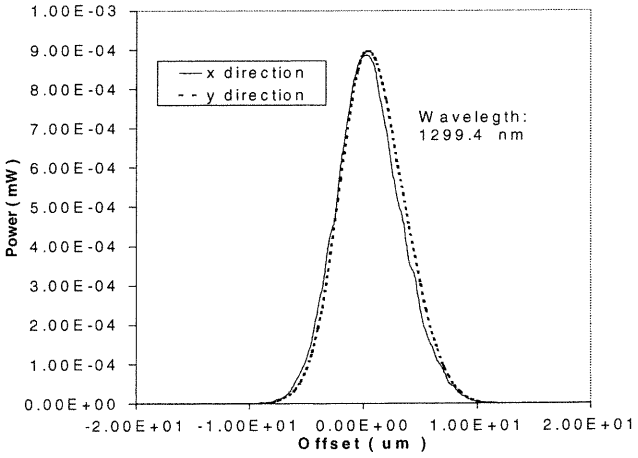

Figure 4.10 The power output of 1299.4 nm and 1553 nm laser.

Figure 4.11 is the measured beam profile for 1553 nm wavelength. The receiving fiber is 3M low-mode field single-mode fiber. The numerical aperture is 0.26 and the core diameter is 4.3 μm. The measured beam waist is 5.3 μm (field mode width if not specified). We simulated the Gaussian beam by taking w_o=*5.3* μm into equation (4.4) (see Figure 4.12). Comparing the measured beam profile with the Gaussian beam, it is obvious that the light propagation in the free space after the TH fiber follows the Gaussian beam distribution as described in 3.1.1.

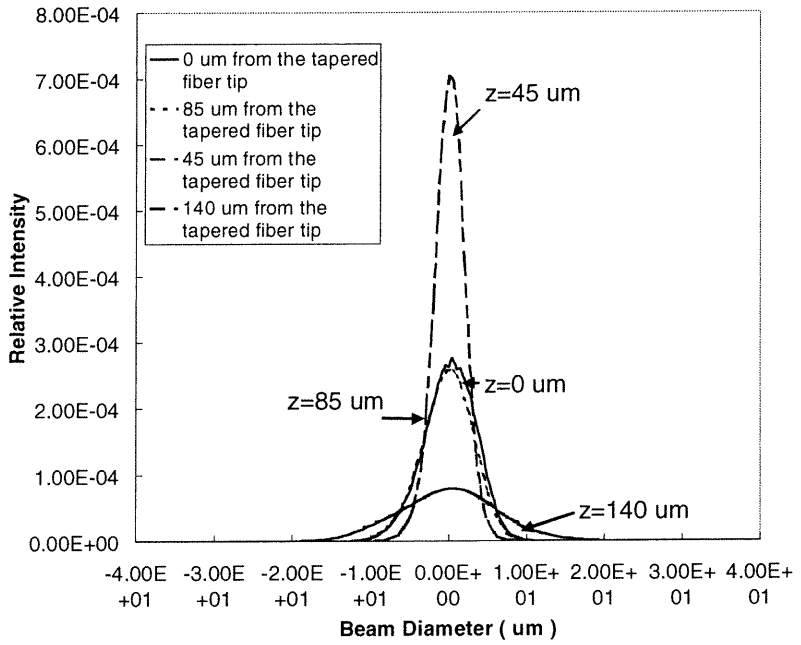

Figure 4.11 The beam profile from TH fiber measured at different z positions at wavelength of 1553 nm (z=0 um is located at TH fiber tip).

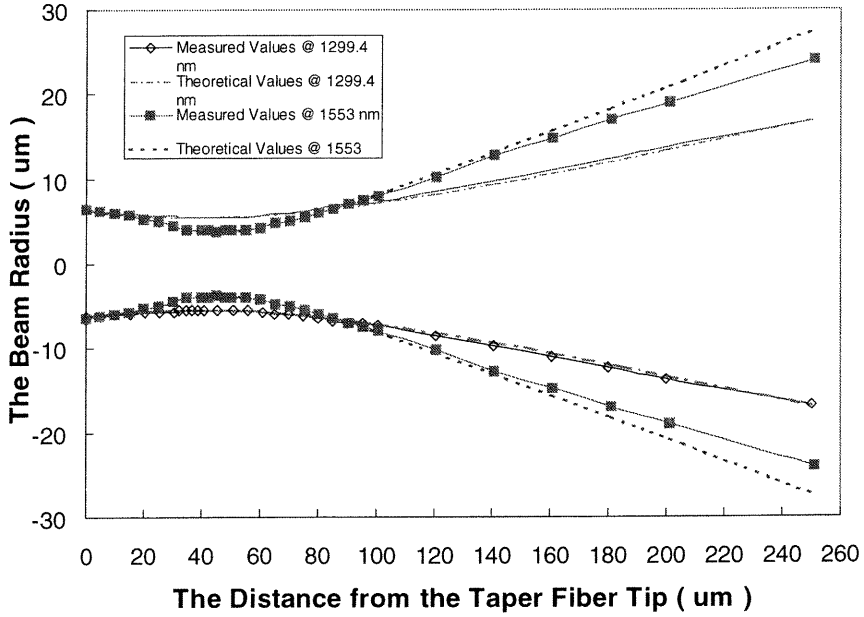

Figure 4.12 The beam profile comparison between experimental and Gaussian simulation.

For 1299.4 nm beam profile measurement, the receiving fiber is corning single mode fiber SMF-28$^{TM.}$ With a core diameter of 8.3 μm. It also abides by the Gaussian beam distributions, and the beam waist is 7.7 μm. Comparison of the beam profile between 1299.4 nm and 1553 nm and their parameters are listed in Table 4.4. Using equation (4.12), the measured power widths are transferred into mode field widths in Table IV, and there are 7.7 μm and 5.3 μm for wavelength 1299.4 nm and 1553 nm, respectively. The beam half angle of 3.04 ° at 1299.4 nm can be obtained from equation (4.5), and 5.43 ° at 1553 nm. In Figure 13, a clear 3-D view of Gaussian beam distribution is present for 1553 nm of TH fiber. At beam waist position ($z=0$), beam

curvature *R(0)=0*, which means it is a plane front wave and you can obtain a collimating light at this point.

Table 4.4 Gaussian beam parameters from TH fiber end (length=458 μm, lens radius = 48μm and pulling angle = 16.2 °).

Wavelength (nm)	W (0) (μm)	Focal distance* (μm)	Half angle (deg)	R (Zc)** (μm)	W (Zc)** μm)	Z_R (μm)
1299.4	7.77	38.6	3.04	82.70	8.04	46.46
1553	5.30	45.2	5.34	53.44	6.77	18.08

* The distance from the tip of the launching TH fiber to the position where $\omega = \omega_0$.

** The input end of receiving fiber is located at $Z = Z_c$. In this case, $Z_c = 38.6\ \mu m$ for 1299.4 nm and $Zc = 45.2\ \mu m$ for 1553 nm.

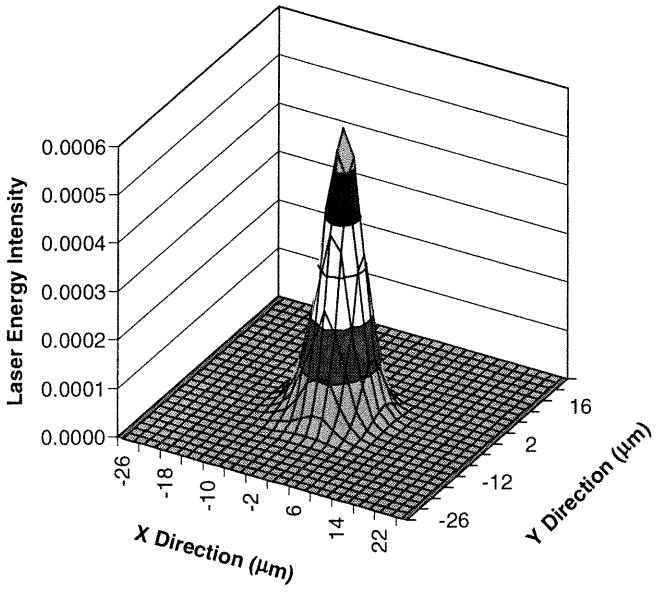

Figure 4.13 3-D view of Gaussian Beam from TH fiber.

The larger the R value, the more the light divergent. Since R is proportional to λ, the light gets a larger scattering at 1553 nm than 1299.4 nm. The focal point is at 45.2 μm from the tip of TH fiber for 1553 nm and 38.6 μm for 1299.4 nm. The Raleigh Range is 18.08 μm for 1553 nm and 46.46 μm for 1299.4 nm, which is in a reasonable range for us to get quasi-collimating during assembly.

The coupling efficiency is also measured between two TH fibers, and coupling efficiency varies with the distance between the launching and receiving TH fibers as shown in Figure 4.14. The graph shows that the coupling efficiency reaches a maximum when the separation between the two TH fibers is about 85 μm. When the spacing becomes greater than 85 μm, the coupling efficiency decreases. If this result is compared with the one obtained from beam profile measurements in Figure 4.10, the beam mode field distribution matching can be observed between the mode at $z=0$ (from the tip of the TH fiber) and that at $z=85\ \mu m$, which simply means if the launching TH fiber is placed at $z=0$ μm and another receiving TH fiber is at $z=85$ μm, and the two TH fiber have the same mode field diameter, the coupling efficiency will be maximum . However, if the receiving fiber is placed at $z=45\mu m$, there will be a big mode field mismatch between launching and receiving fiber. Therefore, the coupling efficiency will drop dramatically. More theoretical considerations about coupling scheme will be discussed in section 3.3. From Figure 4.12 and Figure 4.14, a conclusion can be drawn that with this type of TH fiber design, the optimized coupling separation between launching and receiving fibers is about 85 μm.

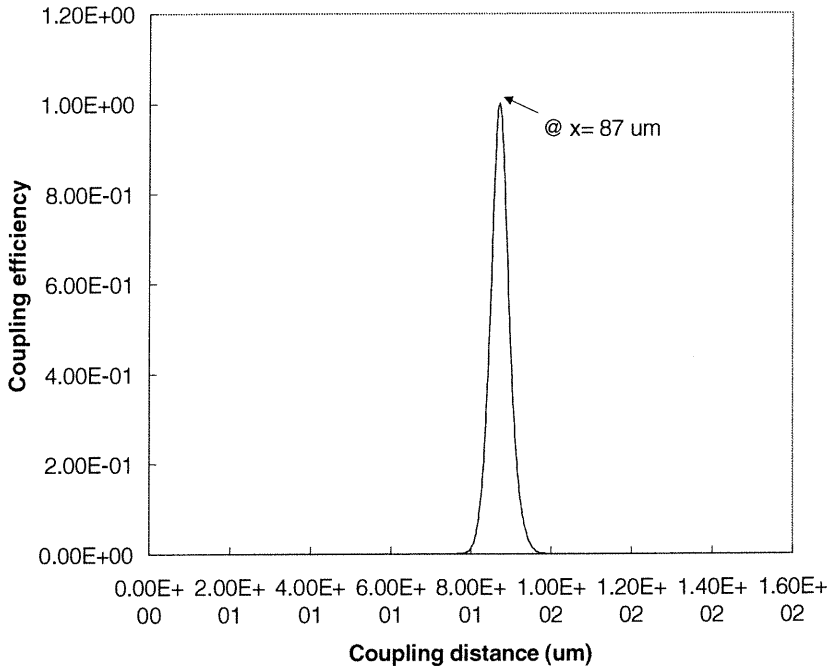

Figure 4.14 The coupling efficiency as a function of coupling distance between two TH fibers.

3.1.3 *TH fiber and flat-end fiber comparison*

The flat-end SMF-28 fiber is also measured to compare with the TH fiber results. Figure 4.15 shows that the beam coming from a flat end fiber is divergent quickly and there is no focal point like the case for TH fiber. Therefore for flat-end fiber, the closer the receiving fiber to the launching fiber, the better the coupling efficiency. Figure 4.16 is the beam profile comparison of flat-end file at its tip end ($z=0$ μm) and a TH fiber at $z= 25$ μm. This graph shows that the optimized coupling position for a flat-

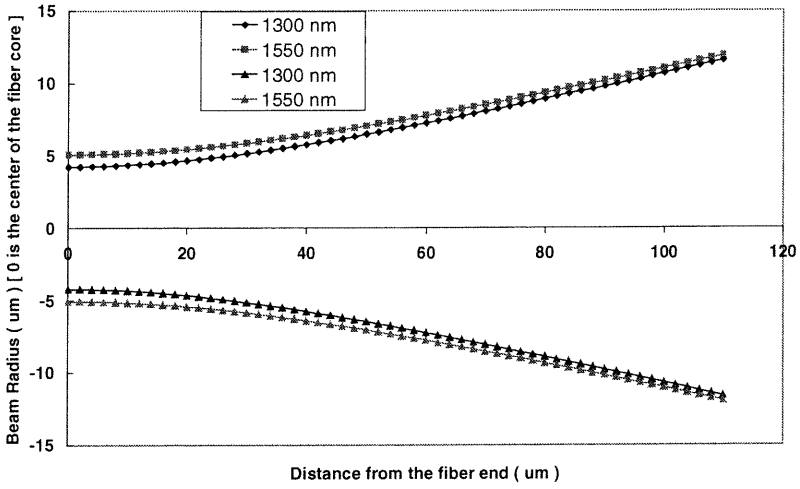

Figure 4.15 Beam propagation after flat-end fiber.

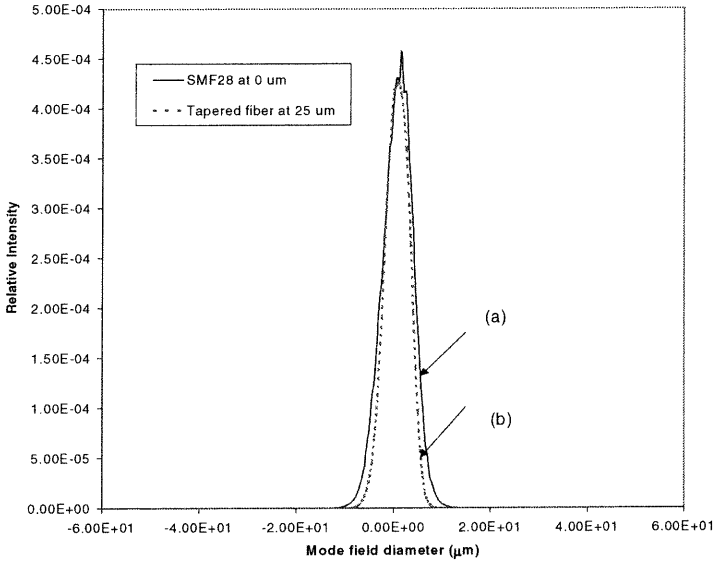

Figure 4.16 Flat-end fiber beam profile at tip position. Beam profile of flat end fiber at z=0 μm (curve (a)) matches with TH fiber at z=25μm (curve (b)).

-end launching fiber with a TH receiving fiber will be 25 μm. The coupling efficiency measurements (Figure 4.17) further prove that the optimized coupling separation between flat-end and TH fiber is 25 μm, not zero, which is far smaller in comparison with 85 μm between two TH fibers.

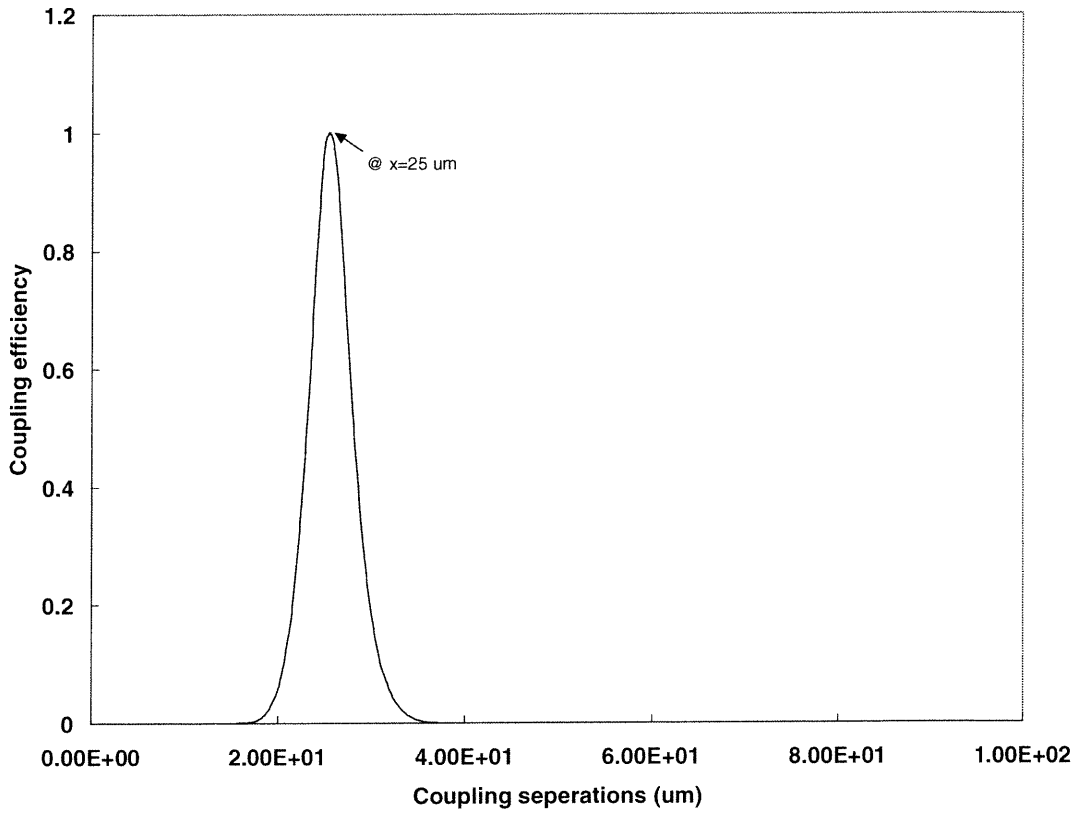

Figure 4.17 The coupling efficiency as a function of coupling separation between flat-end and TH fiber.

A setup (Figure 4.18) is built to capture the light distribution from TH and flat-end fibers in free space to obtain a visual comparison of the light propagation after those two different types of fibers. A He-Ne laser is used as the laser source. The fiber

under test is fixed on an x-y-z stage. The stage can be adjusted so that the light from the TH fiber end is cut through by a ground glass plate. Beam propagation images are captured by a video camera.

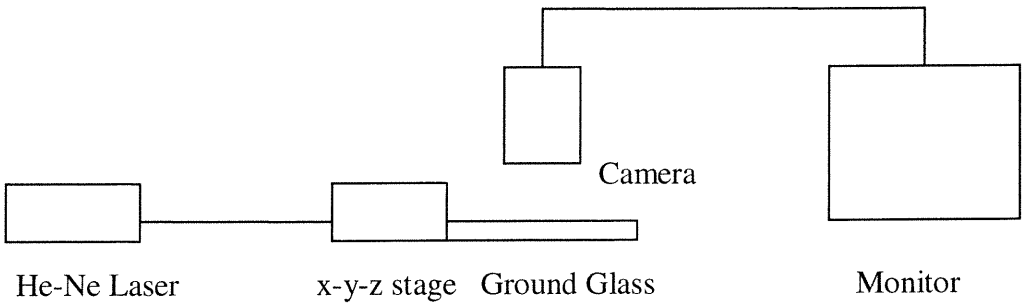

Figure 4.18 Light distribution image capture setup.

Figure 4.19 (a) is the light distribution from TH fiber and (b) is from flat-end fiber. These photos show that after leaving TH fiber, the focus point of divergent light is at 40-60 μm away from TH fiber tip. However, same light after leaving the flat-end fiber, light quickly diverges and there is no focal point captured along the light propagation. This result is consistent with the previous beam profile measurements. Figure 4.15 shows that the beam profile of flat end fiber at $z=0$ μm matches with TH fiber at $z=25$μm, which means the optimized separation between TH fiber and flat-end fiber is 25 μm in comparison to 85 μm between TH fibers. Figure 4.15 also shows that the measured mode diameter of SMF by this technique is about 10 μm in comparison to

mode field diameter of 9.5 to 11.50 μm at 1553 nm in Table 2. Therefore, using this technique to measure beam profile is accurate.

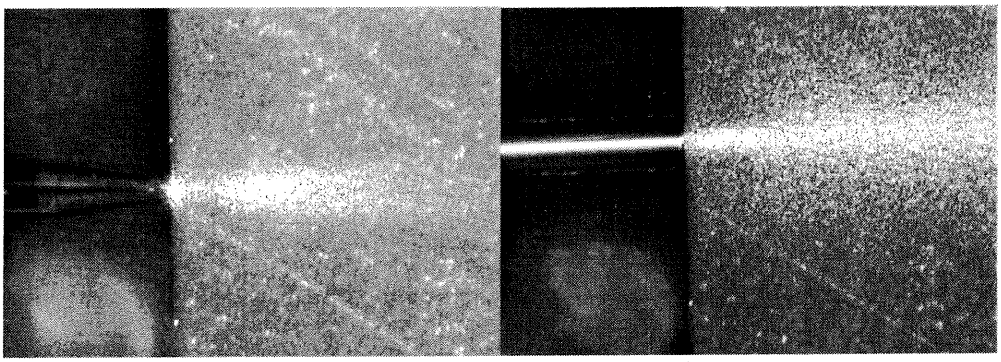

(a) (b)

Figure 4.19 Light distribution after: (a) TH fiber; (b) flat-end fiber.

3.2 Light Transmission in Tapered Region

The free space propagation of light coming from TH fibers has been discussed in the last section as well as the beam profile measurements. However, the beam propagation in the tapered region still reminds unknown. In this section the beam properties in tapered area will be described, such as mode field diameter and its relationship with core diameter. Furthermore, the effect of the taper lens on the beam propagation and transformation will be discussed. Eventually, the comparisons between theoretical calculation and some experimental results will be given.

3.2.1 *Beam profile*

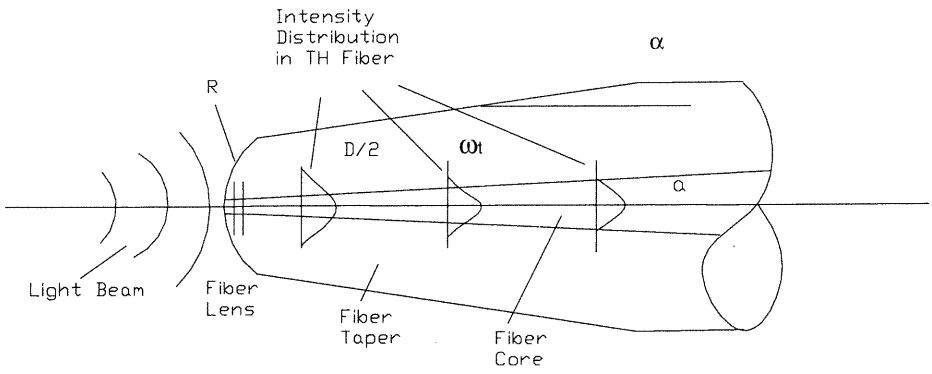

Figure 4.20 Schematic representation of the coupling diagram.

Figure 4.20 shows a schematic representation of the coupling diagram in a receiving TH fiber. It is assumed that in the tapered region the cladding and the core radii decrease with the same ratio while drawing the fiber. Actually, from section 2.1, it is already proven that the ratio of cladding and core diameter keeps a very good constant. Under this condition, according the theory [16], as the core radius decreases an enlargement of the spot size radius of the fundamental Gaussian mode along the tapered section should occur. As efficient coupling requires phase matching the lens radius has to be chosen appropriately. For step-index single-mode fibers the dependence of the spot size radius w_t on the core radius can be well approximated for a V-number larger than one by using equation [18]

$$\omega_t = a\left(0.65 + \frac{1.619}{V^{3/2}} + \frac{2.879}{V^6}\right) \tag{4.13}$$

For the lower V-number ($0.75 \leq V \leq 4$) typical for tapered fiber ends, an even better agreement with the exact theoretical expression is obtained when the following empirical equation is used[19]

$$\omega_t = a(0.85 + \frac{3.04}{V^3} + \frac{1.28}{V^9}) \tag{4.14}$$

Where V is refereed to as the fiber parameter, and it is defined as [13]

$$V = \frac{2\pi a}{\lambda}(n_2^2 - n_1^2)^{1/2} \tag{4.15}$$

where λ is the propagation wavelength, n_1 is the refractive index of the fiber core, n_2 is the value of the cladding index and a is the core radius. This equation holds, only for step-index fibers. Figure 21 gives out the V number as a function of the ratio of beam width and core radius when $0.75 \leq V \leq 4$.

Using the above relation, the change of the spot size radius w_t against core radius a is shown in Figure 4.22. This curve indicates that for small core radii, and their smooth change, an appreciable spot size radius enlargement should take place as compared with the intrinsic spot size radius w_t of the fiber itself (with a = 8.3 μm, Δn =

0.0036). It is obvious that both the optimum coupling separation between TH fibers and the optimum lens radius R increase as the spot size radius at the taper end also increases. The experimental results are depicted in Figure 4. 23.

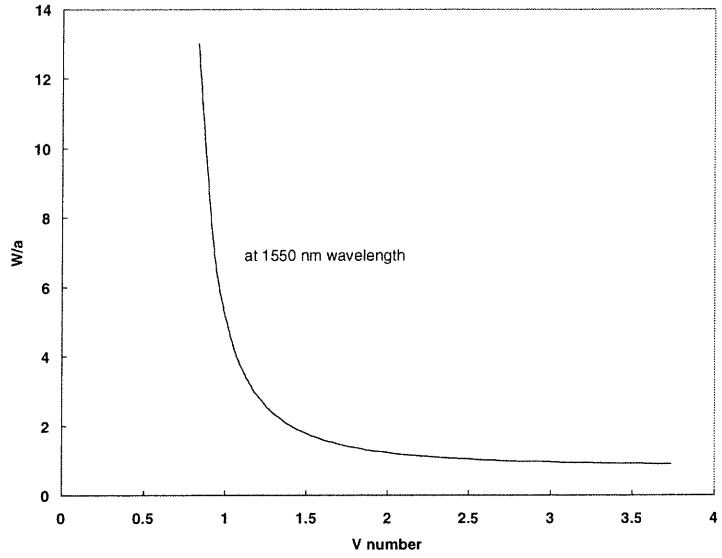

Figure 4.21 V number as a function of w/a.

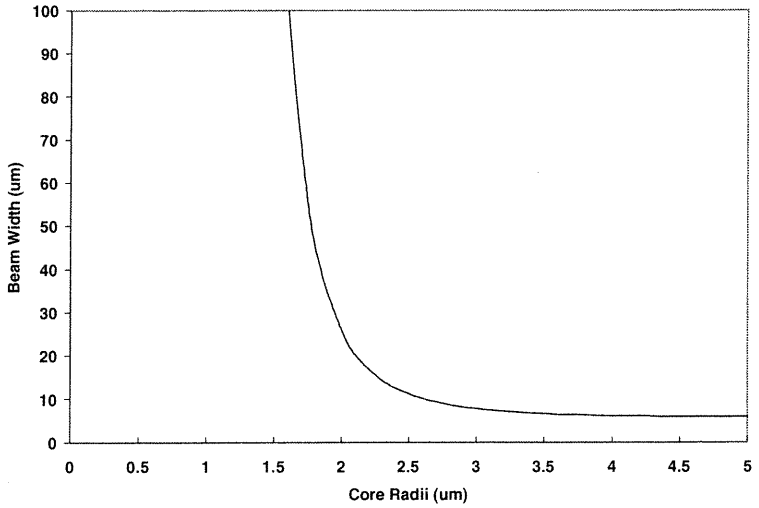

Figure 4.22 Spot size radius vs. TH fiber core radius.

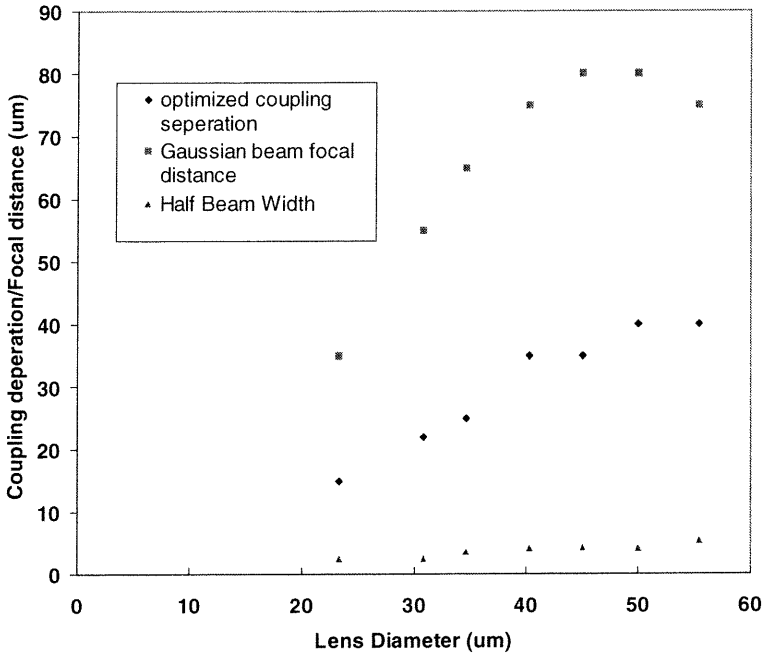

Figure 4.23 Optimum coupling separation as a function of lens radius.

Figure 4.23 shows that the optimized coupling distance is about twice of the focal point. The optimized coupling distance is decided by the mode matching between launching and receiving fibers, that is 85 μm with the designed TH fibers for switching. And hence, a lowest coupling loss is achieved when the distance between two coupling fibers are at 85 μm. Theoretical considerations will be discussed further by coupling scheme in section 3.3. Meanwhile, the light focal point is decided by locating the position of the beam half width ω_0.

Therefore, a conclusion can be drawn that the small core radius in tapered end region will result in a wider beam diameter. A wider beam diameter requires a hemisphere lens with larger diameter to focus the light. The larger the lens diameter the

longer the optimized coupling distance between launching and receiving fiber. A detailed explanation on TH fiber coupling scheme will be given in section 3.3.

However, TH fiber fabrication results show that the maximum lens diameter that can be processed is 50 μm. The optimized coupling distance will not vary in proportion to the lens diameter any longer after 50 μm. This is because when longer taper tips are feedback to get a larger diameter lens, the taper core radius naturally turns out to be larger with this processing. While a large core radius creates a smaller mode field diameter and this smaller mode field diameter will result in a short coupling distance even though the lens diameter became larger. A saturation phenomena is observed as shown in Figure 4.23, and thus, the optimized coupling distance is determined by not only the lens diameter but also the tapered core radius.

3.2.2 *Propagation of beams through TH fiber hemisphere lens*

In this section the effects of hemisphere lens on the propagation of the beam from TH fiber to free space will be determined. In the derivations the assumption were made that the modal field profile of the fiber is well described by a Gaussian field [19] and the hemispherical lens acts as a thin lens [18], that is the fiber core is present up to the apex of the lens. The configuration shown in Figure 4.24 is to be used for the discussions. Assuming that the beam width ω_1 and the radius of curvature R_1 are known at the plane $z=z_1$, and the lens is placed at $z=z_2$. ω_2, *and* R_2 are the beam width and radius of the wave curvature immediately after the thin lens, respectively. The lens has a

focal length of f, and the beam half width in free space, w_{0f}, after lens transformation is to be determined.

Actually for an ideal thin lens, it simply changes the phase of the beam but does not influence its width. The beam width parameter ω is thus unchanged, i.e. $\omega_1 = \omega_2$, while the phase front curvature changes. If equation (3.2) represents the field immediately to the left of the lens, we obtain the field immediately to its right by multiplication with the phase shift term[16]

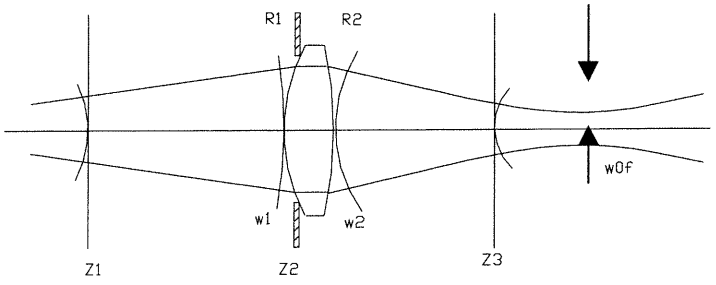

Figure 4.24 Effect of a thin lens on a Gaussian beam.

$$e^{i\gamma} = e^{i(\pi / \lambda f) r^2} \tag{4.16}$$

An unimportant constant phase shift $e^{i(\pi / \lambda f) R^2}$ (R is the radius of lens) was omitted. The product of (4.2) with (4.16) must again result in a Gaussian beam with a different radius of curvature R_2. Thus

$$\frac{1}{R_2} = \frac{1}{R_1} - \frac{1}{f} \tag{4.17}$$

Equation (4.14) together with $\omega_1 = \omega_2$ represents the transformation law of a Gaussian beam that is passing through a thin ideal lens. A nearly parallel beam propagates in the TH fiber tip region so that we can assume $R_1 \rightarrow \infty$, i. e. $R_2 = f$. A taper lens with a radius of curvature R and refractive index n transforms a spot size radius w_t to a Gaussian beam with beam half width of w_{0f} according to the relation [16]

$$\omega_{0f} = w_t \left[1 + \left(\frac{\pi (n-1) \omega_t^2}{\lambda_0 R} \right)^2 \right]^{-1/2} \tag{4.18}$$

The far-field angle θ_{FWHM} (if Gaussian like in the shape) is related to the spot size radius by the expression[19]

$$\theta_{FWHM} = (2 \ln 2)^{-1/2} \tan^{-1} \left(\frac{\lambda_0}{\pi \omega_t} \right) \tag{4.19}$$

In order to do near-field measurements, TH fiber is shortened to the length of 29.6 μm, then the tips of which are polished to optical quality. The mode field width immediately after the tip of the shorten fiber is measured and it is 10.6 μm. The same technique described in 3.1.2 are used for the measurements. Taking measured near-field beam profile results, , $\omega_f \cong 10.6\ \mu m$, into equation (4.15), the free space half beam width ,w_{0f}, is obtained, which can then be compared with the theoretical and experimental results in

section 3.1.2. The ω_{0f} calculated from near-field tapered region beam profile measurement is 4.70 μm at 1553 nm, while the far field measured value is 5.30 μm. This differentiation probably comes from the near-field measurement, ω_f (used in calculations) , of a fiber, which only can be shorten for 29.6 μm. Nevertheless, the result from far-field measurement is quite consist with the theoretical calculation result in the tapered regions.

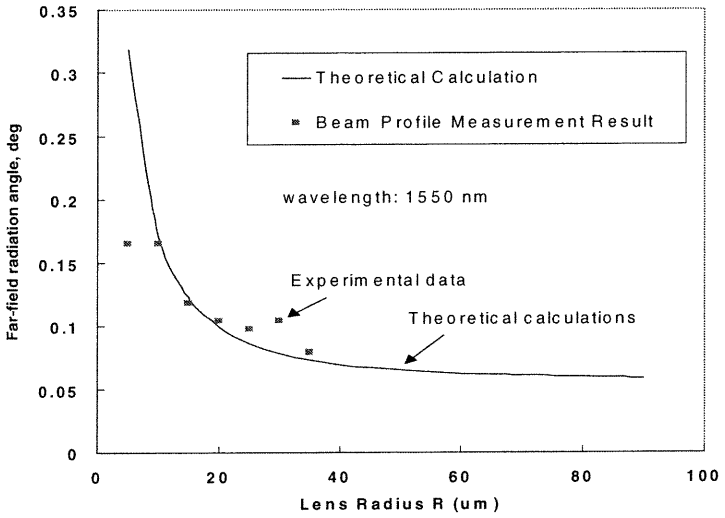

Figure 4.25 Far field radiation angle θ_{FWHM} plotted as function of the radius of curvature of the hemisphere lens. Experimental data was obtained by using the measured beam width with different lens radius in section 3.2.1.

Since shortening the taper length with optical flat end is rather difficult to achieve, an alternative approach can be used to determine the spot size radius widening at the taper end by measuring the far-field intensity profile of the TH fiber, the technique of which is described in section 3.1.2. Using these results and measuring the

lens radii it is then straightforward to calculate the spot size radius enlargement at the taper tip. The calculated variation of the far-field angle θ_{FWHM} as a function of the lens radius R_L is plotted in Figure 4.25 above.

3.3 TH Fiber System Coupling

Generally, the hemispherical lens at its end focuses the diverging light coming from the single-mode-tapered fiber at reflective micro-mirror. The diverging light emission from mirror is converged by the hemispherical fiber tip of the receiving TH fiber. A nearly parallel beam propagates in the tapered region of the TH fiber, while the width of the characteristic field in the tapered core region decreases as the core radius increases. Therefore the converted light beam radius matches the field radius of the fiber at a certain point in the tapered region where strong coupling occurs. In this part, firstly, coupling scheme between TH fibers and among TH fiber-mirror-TH fiber are presented. Secondly the different coupling efficiencies are described and alignment tolerances are discussed. Lastly, the coupling between core and cladding mode are investigated.

3.3.1 *Coupling scheme*

Although the fiber coupling efficiency problem is similar in many respects to the classical optical imaging problem, there is an important difference. This difference is that the single-mode source fiber, mirrors, and receiving fiber together comprise a coherent system, rather than an incoherent system with a Lambertian source

as is most often encountered in classical optics. In our discuss we limit to "weakly guiding: fibers [20,21] defined by the relation $n_1/n_2-1<<1$.The incident electric field E at the input end of the fiber can then be expressed in terms of fiber modes as follows [22]

$$E = \sum_{\nu} c_{\nu} E_{\nu} \tag{4.20}$$

The summation symbol indicates symbolically summation over guided modes (only one for single mode fibers) and integration over radiation modes. The symbol ν labels the modes and $\nu=0$ for guided mode of single mode fiber. Mode orthogonality allows us to obtain c_0 from (4.17)

$$c_0 = \frac{1}{2P} \int_0^{2\pi} d\phi \int_0^{\infty} (E \times H_0) e_z r dr \tag{4.21}$$

H_0 is the magnetic-field vector of the guided mode, e_z is a unit vector in the direction of the fiber axis, and r and ϕ are cylindrical coordinates in the planet at right angles to the axis of the fiber. E represents the field that the launching fiber generates at the input end of the receiving fiber, i.e. the Gaussian beam mode.

The power transmission coefficient is obtained from (4-21) by the relation

$$T = |c_0|^2 \tag{4.22}$$

For misalignment types shown in Figure 4.26(a), the axial offset, the power transmission coefficient becomes [18]

$$T = \frac{4\left[4Z^2 + \frac{\omega_1^2}{\omega_2^2}\right]}{\left[4Z^2 + \frac{\omega_2^2 + \omega_1^2}{\omega_2^2}\right]^2 + 4Z^2\frac{\omega_2^2}{\omega_1^2}} \tag{4.23}$$

where the ω_1 and ω_2 are the half beam width of the two coupling lights, and Z is the normalized fiber separation distance defined as

$$Z = \frac{D}{n_2 k \omega_1 \omega_2} \tag{4.24}$$

where D is the fiber separation and n_2 is the refractive index of lens. The power transmission coefficient through TH fibers shown in Figure 4.26 (b), the lateral offset, assumes the form,

$$T = \left(\frac{2\omega_1\omega_2}{\omega_1^2 + \omega_2^2}\right)\exp\left[-\frac{2d^2}{\omega_1^2 + \omega_2^2}\right] \tag{4.25}$$

where d if the offset from the alignment in the x or y direction (see Figure 4.26 in detail). The amount of offset that reduces the transmitted power to *1/e* of its maximum value can be defined as

$$d_e = \left(\frac{\omega_1^2 + \omega_2^2}{2} \right)^{1/2} \tag{4.26}$$

For the fiber tilt shown in Figure 4.26 (C), the power transmission coefficient is,

$$T = \left(\frac{2\omega_1\omega_2}{\omega_1^2 + \omega_2^2} \right)^2 \exp\left[-\frac{2(\pi n_2 \omega_1 \omega_2 \theta)^2}{(\omega_1^2 + \omega_2^2)\lambda^2} \right] \tag{4.27}$$

where θ is the tilt angle (Figure 4.23). The tilt angle that made the transmitted power decreases to *1/e* of its maximum value is given by the expression,

$$\theta_e = \left(\frac{w_1^2 + w_2^2}{2} \right)^{1/2} \frac{\lambda}{\pi n_2 w_1 w_2} \tag{4.28}$$

When $\omega_1 = \omega_2 = \omega_0$, the mode field of launching and receiving fiber matching to each other, the coupling loss is given by $-10log_{10}T$, where T in (4.23,24,25) simplified as[23]

$$T_z = \frac{4Z^2 + 1}{(2Z^2 + 1)^2 + Z^2} \qquad \text{for axial misalignment} \tag{4.29}$$

$$T_{x,y} = \exp\left[-\left(\frac{d}{\omega_0} \right)^2 \right] \qquad \text{for lateral misalignment at } T_z = 1 \tag{4.30}$$

$$T_\theta = \exp\left[-\left(\pi\omega_0 \frac{\theta}{\lambda}\right)^2\right] \qquad \text{for angular misalignment at } T_z=1 \qquad (4.31)$$

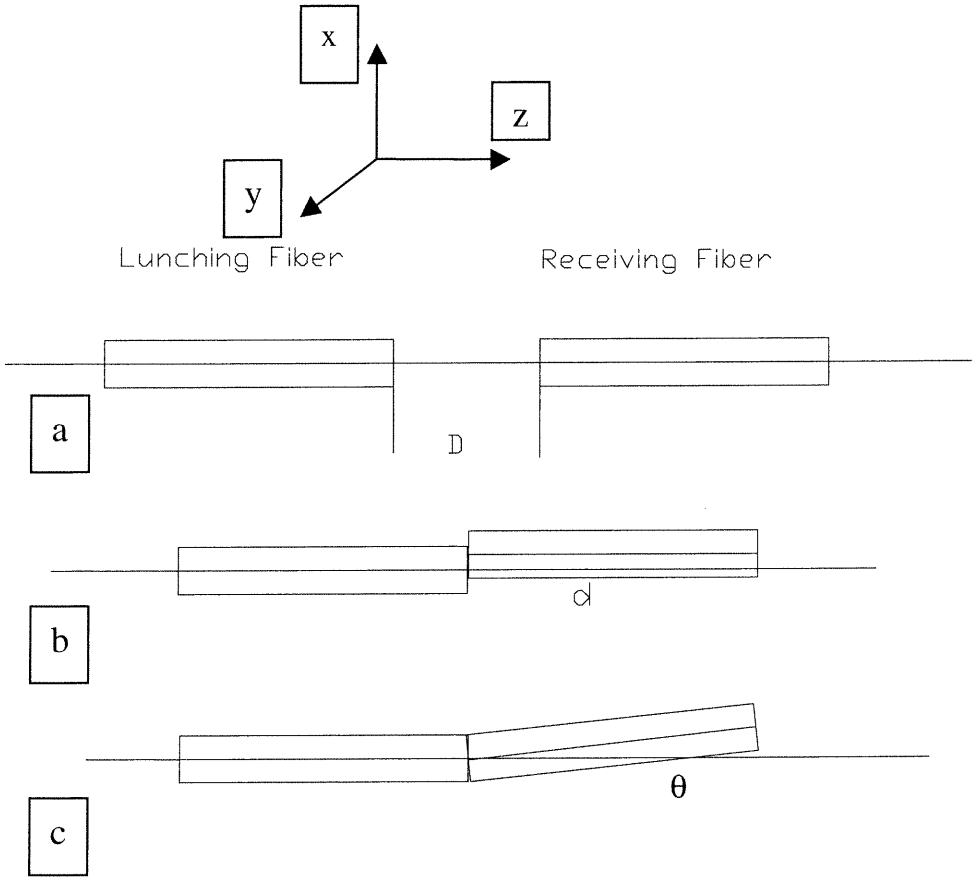

Figure 4.26 Three types of TH fiber misalignments: a) axial misalignment; b) lateral misalignment; and c) angular misalignment.

By combining (4.26) and (4.28) with $\omega_1 = \omega_2$, we obtain a very useful and interesting relation as

$$d_e\theta_e = \frac{\lambda}{n_2\pi} \tag{4.32}$$

This expression states that as one of two variables becomes smaller, the other must become larger. If a single mode fiber is designed with a small value of Δ (the refractive index difference between core and cladding materials), to allow the field to spread out in the transverse direction, the beam width (ω) becomes large and, consequently, d_e may be large indicating that a large lateral misalignment can be tolerated. Equation (4.32) states that for a large value of d_e, the tilt tolerance decreases. A TH fiber that is tolerant of large lateral misalignment is intolerant with respect to tilts and vice versa.

Figure 4.27-28 give out the theoretical curve of coupling coefficient vs. the misalignment calculated from equation (4.25), (4.26) and (4.27) respectively.

Figure 4.29 shows a plot of the power transmission coefficient as a function of ω_1/ω_2. When $\omega_1=\omega_2$ the power transmission equals to 1, the coupling efficiency theoretically could reach 100 percent, that is when the beam field mode at the input end of receiving fiber matches with the one at the output end of the launching fiber. A ratio $\omega_1/\omega_2=1.4$ causes a power loss of 10 percent.

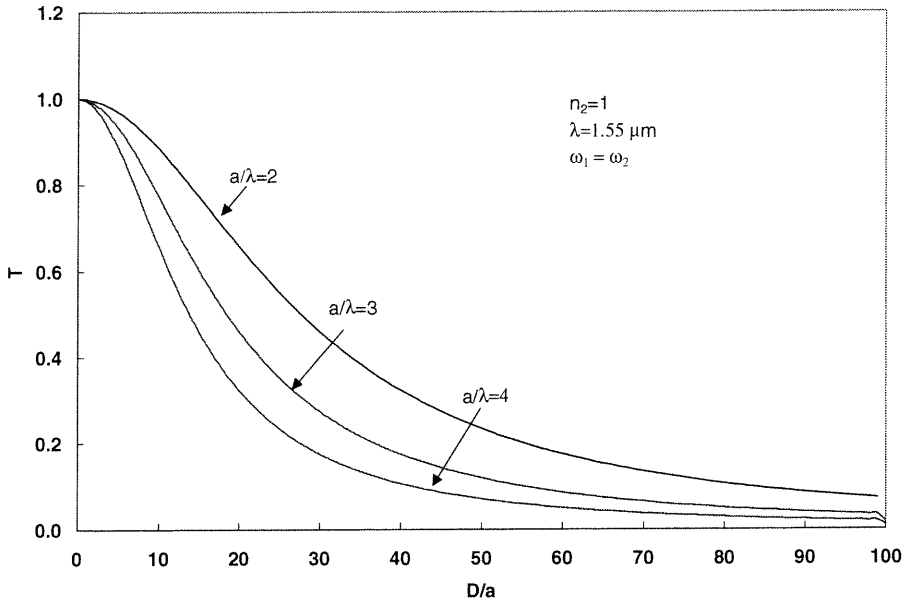

Figure 4.27 Transmission coefficient vs. the axial misalignment when $\omega_1=\omega_2$.

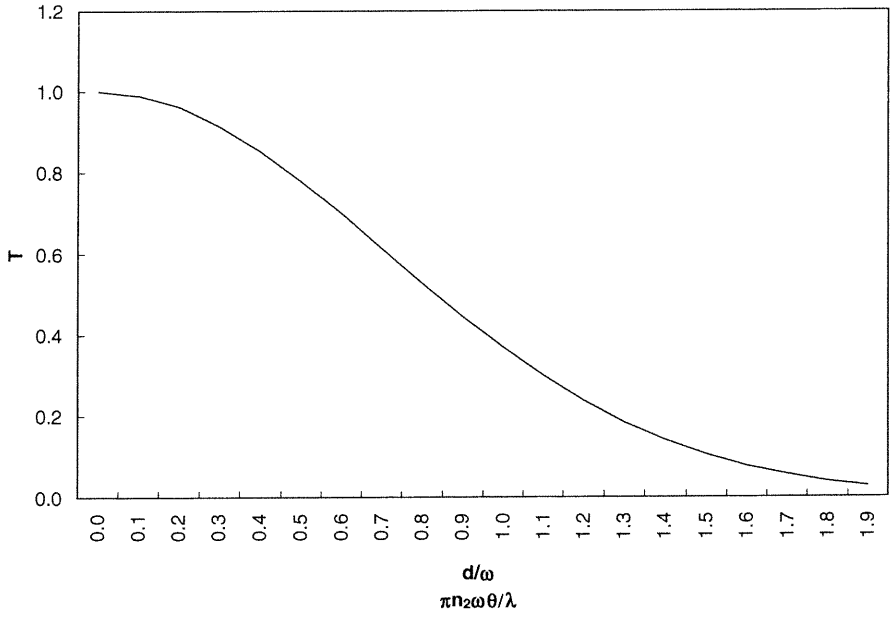

Figure 4.28 Transmission coefficient vs. the lateral offset when $\omega_1=\omega_2$.

In section 3.1.2, when the beam profile at the tip of the launching fiber matches with that at the input end of the receiving fiber, a maximum coupling efficiency is reached. The separation between those two fibers is defined as the optimized coupling distance. The theory in this section further verifies the experimental results. Combining with the results from section 3.2.1, the optimized coupling distance for TH fiber with certain lens diameter and tapered shape can thus be predicted.

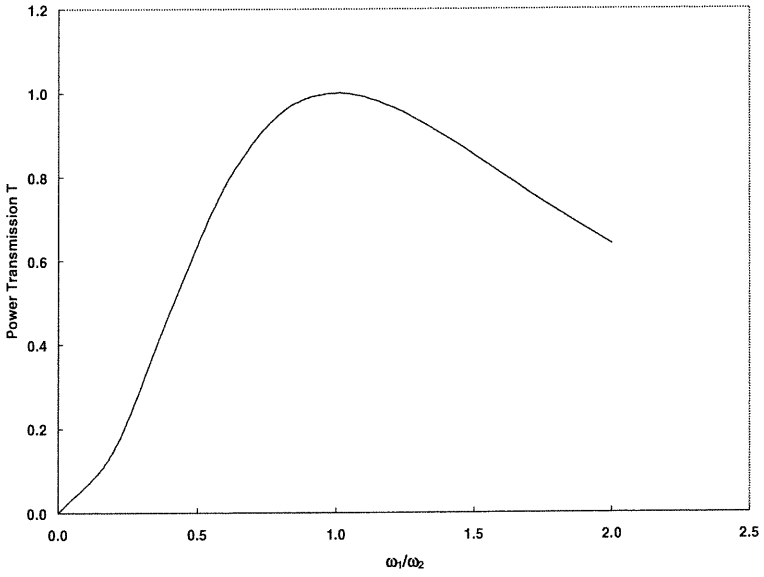

Figure 4.29 Power transmission coefficient as a function of ω_1/ω_2.

3.3.2 *TH fiber coupling measurements*

A coupling loss measurement set-up is illustrated in Figure 4.30. 1310nm and 1550 nm are used as power sources. Cutback technique is used for the

coupling loss testing. Figure 4.31 is the coupling loss vs. different pair of TH fiber that is fabricated in the same conditions. In this case the setback steps is 1500 and filament power is 15 W. Finished TH fiber lens diameter is 48 μm, the tapered length is about 458 μm and the pulling angle is about 16°. Figure 4.31 shows that the coupling losses measured from those TH fibers are all concentrated in a range between 0.5 dB to 0.7 dB. The lowest coupling loss with TH fiber is 0.44 dB. Therefore, both TH fiber fabrication and coupling loss keep a very consistent result, which will benefit to the switching assembly.

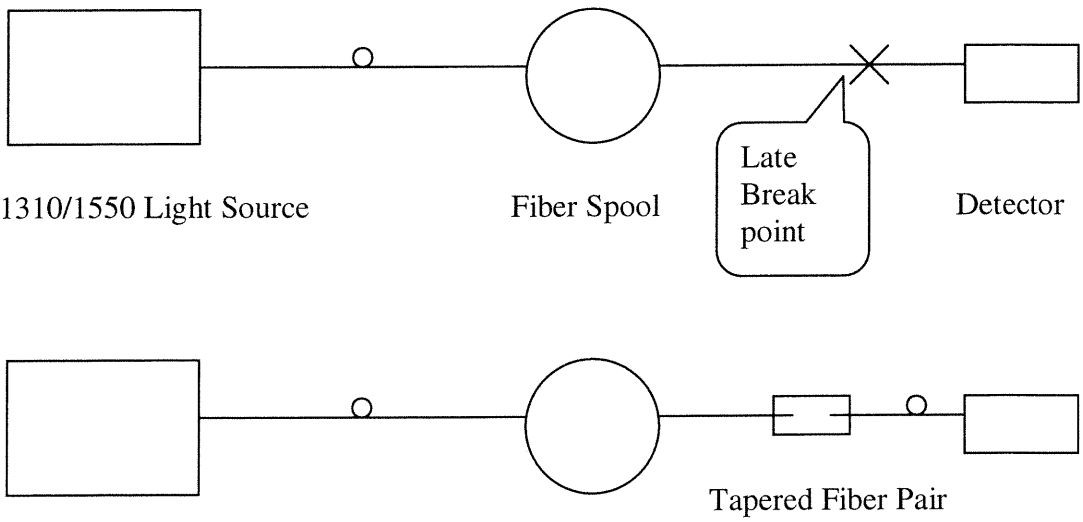

Figure 4.30 Coupling loss measurement setup.

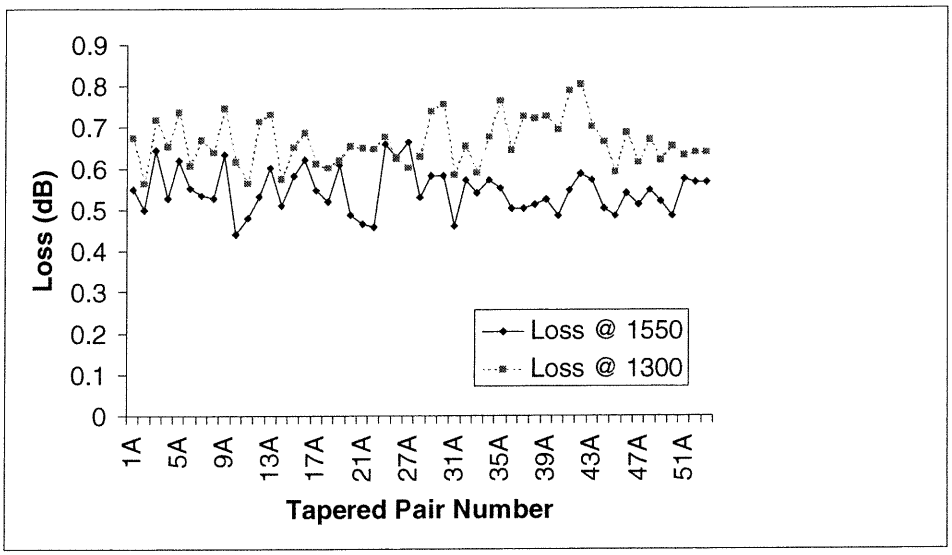

Figure 4.31 The coupling loss measured from different TH fiber pairs.

3.3.3 *Alignment tolerance measurements*

In this section, the sensitivity of the coupling loss of two tapered is measured, as shown in Figure 4.26, to axial and lateral displacement by using tapers with fiber pigtail designed to single-mode at λ=*1229.4 nm*. The experimental setup depicted in Figure 4.10 is used in the alignment tolerance measurements.

In the assembly process, the permissible tolerance for coupling is as important as the coupling efficiency. Typical data for coupling loss vs. fiber displacement as shown in Figure 4.32 (a) and (b) for parallel and perpendicular to the junction plane and separation from the each other. The results show that when two TH

fibers are moved away or misalign from their optimized coupling distance, the extra

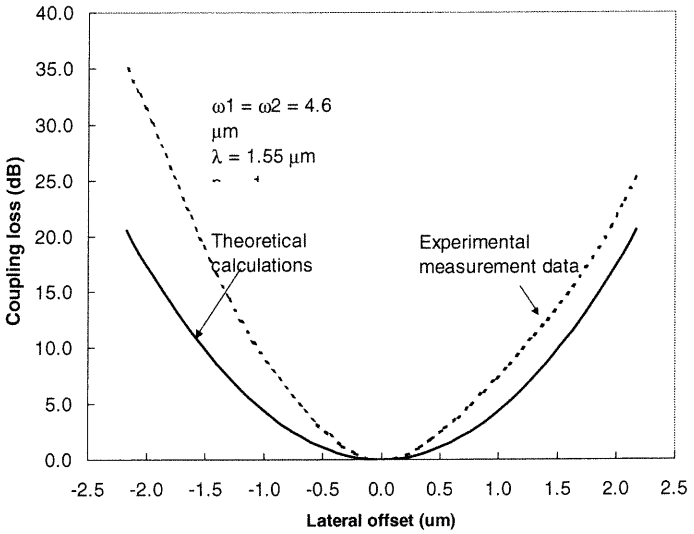

(a)

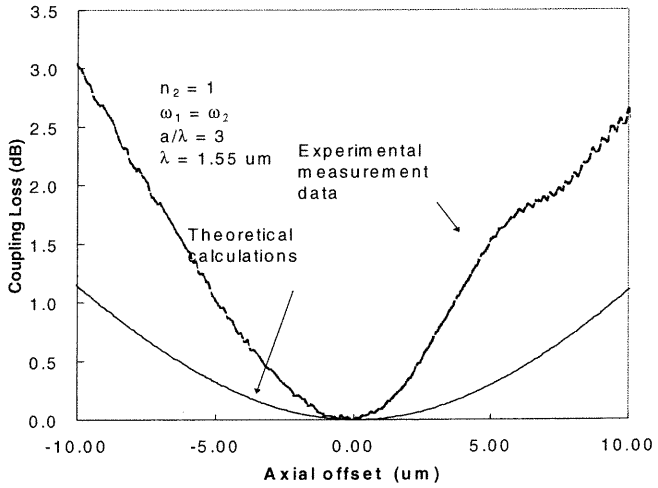

(b)

Figure 4.32 The coupling loss as a function of misalignment: (a) coupling loss vs. axial misalignments; (b) coupling loss vs. lateral misalignments .

losses star to be brought in by this axial offset. When the axial offset reaches to 10 μm, an additional loss of about 2.5 dB is occurred. For lateral offset or misalignment from its optical axis, an additional loss of 2 dB occurred by an offset of 0.5 μm. Clearly, as predicted by theoretical calculations, the TH fiber has more axial misalignment tolerances than lateral misalignments. In comparison experimental measurement data to the theoretical calculations in Figure 4.32 (a) and (b), a higher experimental loss is observed in both cases (lateral and axial offsets). The possible causes could be that in actual measurements return loss in from the tip of the TH fiber is counted in coupling process, and moreover, when the offset became larger, the field modes for two TH fibers begin to mismatch with each other and more loss will occur in the coupling due to this mismatch (see Figure 4.29). However, in the theoretical curve, $\omega_1 = \omega_2$ is assumed in calculations. Nevertheless, the theoretical calculations present the trend in terms of both axial and lateral misalignment effects on coupling loss.

3.3.4 *Mode coupling discussions*

The tapering has a significant effect on the optical field as it propagates along the taper. Initially the field guided by, and substantially confined to, the core. As the core diameter decreases the field spreads out, its spot size increasing as described by equation (4.12) in section 3.1. Eventually a point is reached when the field is no longer guided by the core but is effectively guided by the waveguide consisting of the cladding and the surrounding medium[15]. This fact accounts for the discrepancy between the

experimental measurement and the theoretical prediction (assuming infinite cladding) of spot size by the authors of reference 18. The cladding waveguide is highly multimoded and, if the taper rate is large, coupling to higher-order modes will occur, resulting in power loss from the output of the taper.

The mode will be guided by the core until its local angle of the incidence at the core cladding boundary equals the critical angle. This occurs when [24]

$$\frac{\beta^2 - n_2^2 k^2}{\left(n_1^2 - n_2^2\right)k^2} = \frac{2\alpha_c n_2}{\left(n_1^2 - n_2^2\right)^{1/2}} \tag{4.33}$$

where α_c is the core taper angle, n_1 and n_2 are core and cladding refractive index, β is the light propagation constant.

The condition for a taper to remain adiabatic is [23,25]

$$\left|\frac{da}{dz}\right| \le \frac{a}{z_b} \qquad z_b = \frac{2\pi}{\beta_1 - \beta_2} \tag{4.34}$$

where β_1 and β_2 are the propagation constants of the LP_{01} and LP_{02} cladding modes. A taper satisfying this condition will suffer negligible loss through mode coupling.

The coupling losses of different tapered shapes have been measured (see Figure 4.33) and the results are summarized in Table 4.5. Table 4.5shows that a tapered fiber with a sharp pulling angle, short tapered length suffers a high coupling loss, while

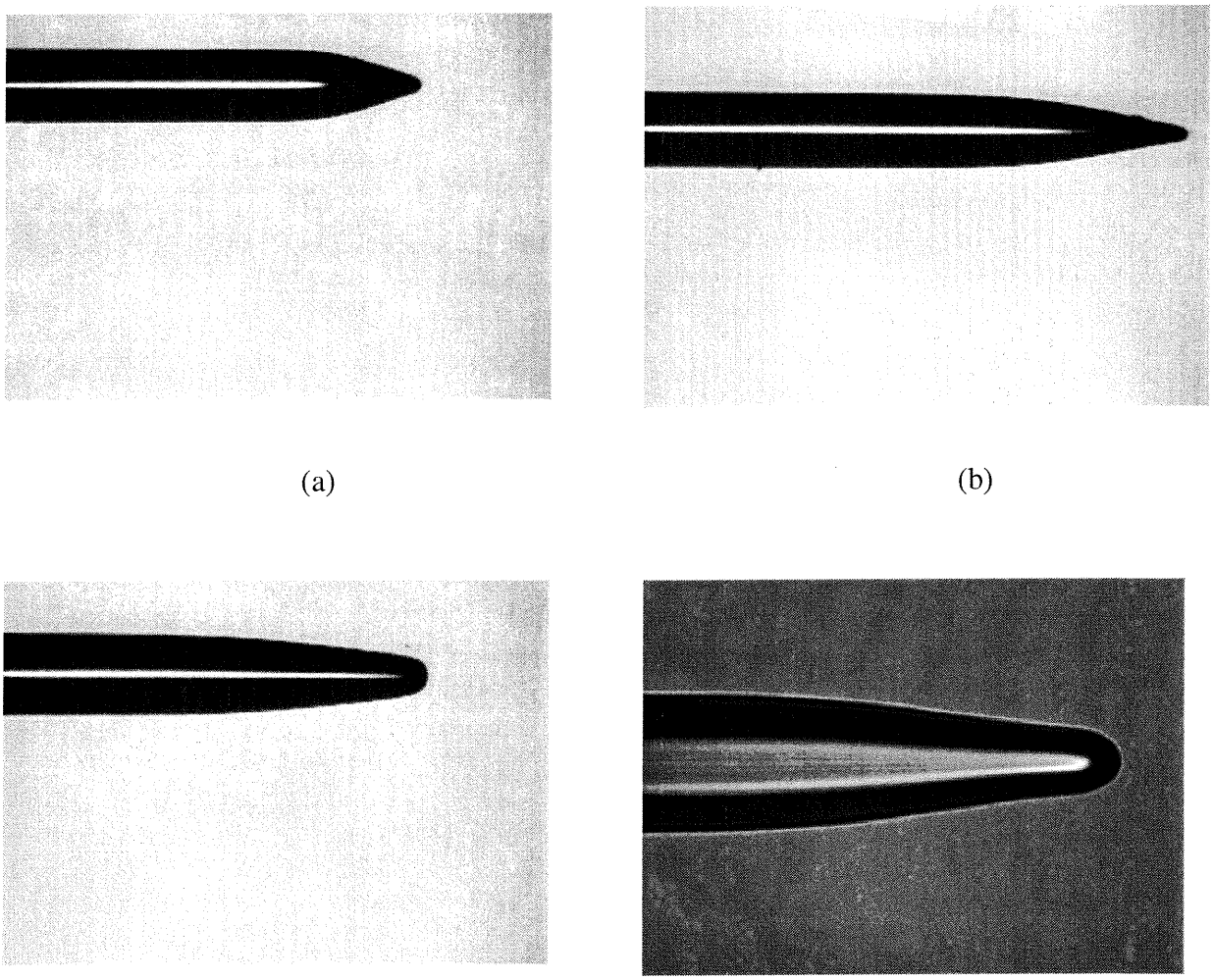

(a) (b)

(c) (d)

Figure 4.33 Different shapes of tapered fibers. (a) Kyocera (b) Amherst (c) Ericsson (d) Vytran.

those with slower pulling angle, longer tapered length offer a low coupling loss. This is because the tapered fibers with sharp slope and short length will not meet adiabatic condition and will result in additional losses from mode coupling. More modes coupling theory has been discussed in Reference 17, 21 and 22.

Table 4.5 Coupling Loss measurement results from different types of tapered fiber.

	Kyocera	Ameherst	Ericsson	Vytran
Coupling Loss (dB)	3.5	2.5	2.0	0.5

4. SUMMARY

In this chapter we explored the fabrication, light propagation, coupling loss due to misalignments and mode mismatch issues with TH fibers, theoretically and experimentally.

With Vytran fusion splice machines, TH fibers with varying hemisphere lenses are carried out. The diameters of the lens are in the range from 23 μm to 55 μm with this Vytran machines setup. However, the potential of this technique is not limited in this range of lens diameter. With a slower motor feedback speed and a high power to tolerated by a wider filament, the larger lens diameter might be achieved. Table 4.6 summarized the optimized TH fiber parameters.

Table 4.6 TH fiber parameters.

Taper length (μm)	Tapered angle (deg)	Lens diameter (μm)	Core/cladding ratio
458±16	16.2	51±1	0.09±0.01

The reproducibility of TH fiber fabricated with this technique is very high. The tolerance of TH fiber lens diameter is about ±1 μm, while the tolerance for tapered length is about ±16 μm. The coupling losses of the TH fibers fabricated under the same filament and conditions are all concentrated in a range between 0.75 dB to 0.5 dB. The lowest coupling loss we are able to measured with TH fibers is 0.44 dB. To our knowledge, this is so far the lowest coupling loss ever reported with tapered fibers. Also it is the only micro component developed that does the collimating and signal coupling with such a low loss and such a high reproducibility.

In order to make the TH fiber work for switch, not only a low coupling loss is desirable but also some other parameters are very crucial for switch alignment and assembly. Those include optimized coupling separation, Raleigh Ranges, and beam width (beam spot). For the TH fiber we developed, the optimized coupling separation between two TH fibers is about 85 μm, the Raleigh Ranges are 46.46 μm at 1299.4 nm and 18.08 μm at 1553 nm, the beam spot for 1299.4 nm and 1553 nm are 7.77 μm and

5.30 μm, respectively. Those results show that TH fiber with those parameters can be very well adopted in the switch alignment and assembly processes.

Another important feature of the TH fiber is the increasing the misalignment tolerant. It has been demonstrated that , in the axial direction, after misalignment of 10 μm from its optimized position, a 2.5 dB extra loss will be added on to its coupling loss, while in the lateral direction the misalignment suffers a tight tolerant. An extra 2 dB will be seen after a misalignment of 0.5 μm. The angular misalignment has not been measured since it is less important to pre-defined alignment groove assembly.

The beam propagation properties have been characterized both inside, outside the TH fiber, and in free space. The effect of hemisphere lens on the beam transformation has also been described. Several equations have been given out to discuss the light propagation with TH fibers. The beam propagation in free space abides the Gaussian distributions, while inside the tapered region a Gaussian beam approximation also can be deployed. The beam width is inverse proportional to the core diameter. The hemisphere lens can be viewed as a thin lens which will change the phase properties of the Gaussian beam while keep its amplitude. The beam profile measurement results are well following the theoretical predictions.

In conclusion, varieties of TH fibers in terms of lens diameter and taper length are developed after controlling the Vytran machines parameter and process, with low coupling loss and good misalignment tolerant. Deployments of the TH fiber in the

optical device alignment will largely easy the assembly processing with high coupling efficiency[26].

REFERENCES:

1 **Nicia, A.,** TE KADE, Tech. Mitt., (1981), 40-46

2 **Tamura, Y., Maeda, H., Shikii, S., Yokoyama, B.**, *Single Mode Fiber WDM in the 1.2/1.3 Micron Wavelength Region*, IOOC-ECOC'85, (1985), 579-582.

3 **Khoe**, G.D., *Practical Low-loss Lens Connector for Optical Fibers*, Electro. Lett., (1978), June 30, 163-164.

4 **Khoe, G.D., Kock, H.G., Kuppers, D., Poulissen, J.H.F.M., DeVrieze, H.M.,** *Progress in Monomode Optical-fiber Interconnection Devices,* J. Lightwave Techno., (1984), LT-2(3), 217-227.

5 **Weidel, E.,** *New Coupling Method in GaAs-laser-fiber coupling*, Electro. Lett., (1975), 11, 436-437.

6 **Odagiri, Y., Schikada, M., Kobayashi, K.,** *High-efficiency Laser to Fiber Coupling Circuit Using a Combination of a Cylindrical Lens and a Seltoc Lens*, Electron. Lett., (1977), 113, 345-396.

7 Private conversation

8 **Oliver, G.P.,** *The Integrated Services Digital Network,* IEE Conf. Publ., (1982), 209, 8-13.

9 **Hirth, P., Knodel, D.,** *Ein Digital Fernsprechanschlub Fur Lichtwellenleiter und Kupferkabel,* TE KADE, Tech. Mitt., (1981), 40-46.

10 **Verhoeckz, N.A.M., Van Den Elzen, H.C., Snuders, W.A.M., Van Gerwen, P.J.,** *Digital Echo Cancellation for Baseband Data Transmission*, IEEE Trans., (1979), ASSP-27, 768-781.

11 **Amitay, N., Presloy, F.V.,** *Optical Fiber Tapers-A Novel Approach to Self-*

aligned Beam Expansion and Single-mode Hardware, J. Light. Tech., (1987), LT-5(1), 70-76.

12 **Jin, X.** *Optical Fiber Index Taper-Theoretical Analysis and Experiment Demonstration,* International J. Infrared and Millimeter Waves, (1998), 19(6), 875-886.

13 **Wagner, R.E., Tomlinson, W.J.,** *Coupling Efficiency of Optics in Single-mode Fiber Components,* Appl. Optics, (1982), 21(5), 2671-2688.

14 **Ladany,I., Wdkstein, H.J., Botez, D.**, in the Processing of the IEDM,IEEE, New York, (1978).

15 **Kuwahara H., Sasaki, M., Tokoyo, N.,** *Efficient Coupling from Semiconductor Lasers into Single-mode Fibers with Tapered Hemispherical Ends.*, Appl. Opt. (1980), 19(15), 2578-2583.

16 **Marcus, D.,** *Light Transmission Optics*, Van Norstrand Reinhold, New York, N.Y. (1982).

17 **Harris, F.S.Jr., Tavennel, M.S., Mitchell, R.L.,** *Single-Slit Fresnel Diffraction Patterns: Comparison of Experimental and Theoretical Results*, J. Opt. Soc. Am., (1969), 59(3), 293-296.

18 **Marcuse, D.**, *Loss Analysis of Single-mode Fiber Splices,* The Bell System Technical Journal, (1977), 56(5), 703-719.

19 **Keil, R., Kiement, E., Mathyssek, K., Wittmann, J.,** *Experimental Investigation of the Beam Spot Size Radius in Single Mode Fiber Tapers,* Electronics Letters, (1984), 20(15), 621-622.

20 **Gloge, D.**, *Weakly Guiding Fibers,* Appl. Opt., (1971), 10(10), 2252-2258.

21 **Jedrzejewski, K.P., Martinez, F., Minelly, J.D., Hussy, C.D., Payne, F.P.,** *Tapered-Beam Expander for Single-Mode Optical-fiber Gap Devices*, Electronics Letters, (1986), 22(2), 105-106.

22 **Marcuse, D.,** *Theory of Dielectric Optical Waveguides*, (1974), Academic Press, New York.

23 **Stewart, W.J., Love, J.D.**, *Design Limitation on Tapers and Couplers in Single Mode fibers*, Technical Digest IOOC-ECOC, (1985), 1, 559-562.

24 **Payne F.P., Hussy C.D., Yataki, M.S.,** *Modeling Fused Single-Mode-Fiber Couplers,* Electronics Letters, (1985), 21(11), 460-462.

25 **Snyder, A.W, Love J.D.**, *Optical Waveguide Theory*, (1983), Academic Press, New York.

26 **Zhang, N.**, *An Efficient, Low Loss Technique for Coupling Fibers to Photonic Devices Thereby*. 2000.

CHAPTER 5: SWITCH ASSEMBLY, PACKAGING AND TESTING

This chapter is divided into three sections. The first section talks about the chip assembly including TH fiber inserting into the chip, assembly equipment setup and assembly procedure descriptions, as well as the device preliminary packaging. The second section presents the testing of switching primary parameters. The last section summarizes the assembly, packaging and switch characterization results.

1. SWITCH ASSEMBLY AND PACKAGING

The photonic package must serve two functions. It must protect the device from its surrounding environment, which can cause electrical or mechanical damage, and also provide for connections to other circuit elements. The degree to which the package protects the device from outside elements has a significant effect on the device's reliability. To this end, hermetic package has been considered to offer the greatest reliability, which is defined as the ability of a package to prevent penetration by environmental contaminants such as water vapor.

Therefore, when reliability is considered, the hermetically packaged device will have a much longer lifetime than the nonhermetically packaged device, particularly with reference to harsh environments.

Besides packaging, the switch assembly process has direct impact on its performance. There are three challenges involved in the assembly procedures. First is how to attach the four TH fiber into the chip with high repeatability and low insertion loss; Second is how to choose epoxy and correctly apply it onto chip without resulting in additional losses from coupling variation or temperature fluctuations; Third is how to design the overall packaging procedure that is very efficient and easily to achieve a consistently results.

1.1 Assembly Equipment Setup

The manufacturer of the equipment used for assembly setups is Newport, CA. As shown in Figure 5.1 (a), the system consists of sample mount stage, pneumatic epoxy dispensing and cure system, 4 manual micropositioners with dual coated fiber holders. The stacks have 4 inch travelling along X and Z and the one facing the operator has a 2 inch travelling along X and Y. This will allow a smaller distance for the operator to reach over. The set up also includes an accessory bridge and indexing rail to move the upper camera, epoxy dispenser and UV epoxy dispensing syringe around. Figure 5.1 (b) is a close look at the sample mount stage with epoxy dispenser.

1.2 Packaging and Assembly Processing

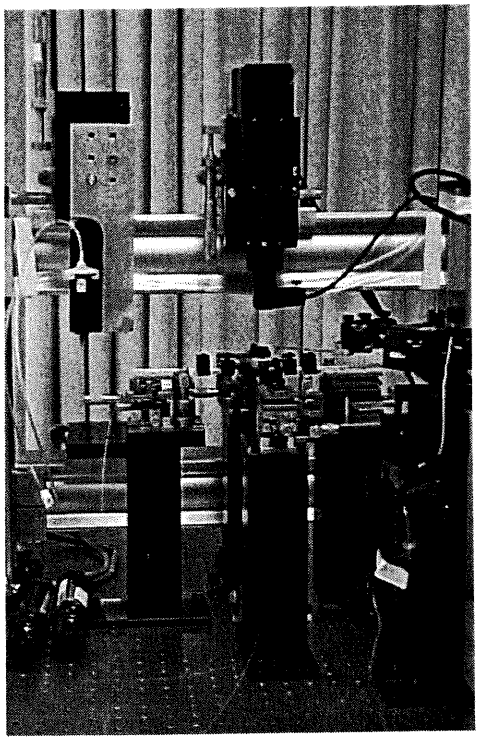

(a)

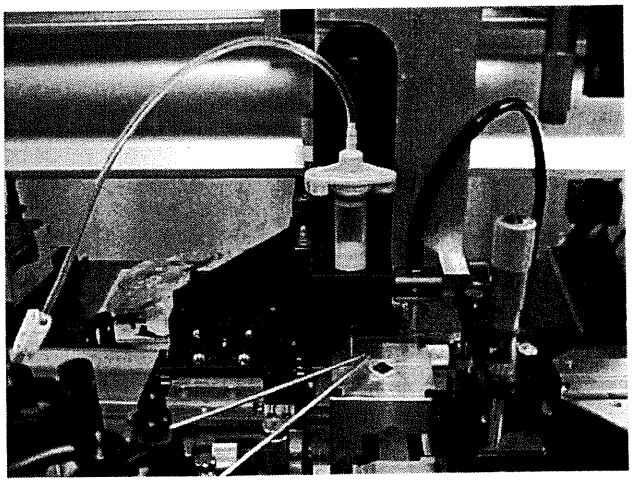

(b)

Figure 5.1 Assembly setups: (a) equipment setup layout.; (b) chip mount stage with epoxy dispenser.

Suitable packages for MEMS optical switch devices must meet a number of requirements, including ruggedness, stability, and adequate mechanical protection. Hermetic packaging is important for this MEMS switch, since the suspension structure might be stick with substrate when chip is in a high humidity environment. The reliability of MEMS devices can also be adversely affected by high humidity level, since water vapor enhances metallization failure mechanisms including corrosion and oxidation. The chips must be secured without the introduction of excessive strain which might impair the device characteristics. The fiber fixing method must allow optical fibers to be rigidly and securely fixed relative to the device

The overall assembly and packaging procedures starts with attaching the chip on ceramic board that is coated with Gold by laser thick film print. The next step is to wirebonding chip to ceramic board and then four TH fibers are inserted into chip-on-board with active optical alignment. The chip-on-board with TH fiber will then be attached with package body. The last step is to seal the lid onto the package with hermetic seam. Table 5.1 describes the packaging and assembly procedure details.

Figure 5.2 illustrates the packaging procedures in assembly drawings. Figure 5.2 (a) shows the packaging flow from chip to chip-on-board till the final hermetic sealed switch product. Figure 5.2 (b) is the cross section of the packaged switch. Initial evaluated hermetic sealed package parameters are listed in Table 5.2.

Table 5.1 Assembly and packaging procedures.

No.	Procedures	Descriptions	Materials
1	Chip Testing	Testing Actuation on probe station to ensure complete stroke (visual confirmation)	
2	Thick Film Printing	Laser Printing Ceramic Substrate with Gold of 500 um thickness	
3	Chip Cleaning	Oxygen Plasma, 400W, 250mTorr, 30minutes	
4	Chip-On-Board Epoxy	Epoxying cleaned chip on ceramic board, cure at 150°C for 1 Hour,	Epoxy part number:84-1 LMI Manufacturer: Ablesteik
5	Chip-On-Board wirebonding	Wedge bond (Less ultrasonic apply) from chip to ceramic. Travel distance is: ~5.5 mm	Gold (with Silicon impurity) Wire , diameter of 1mil (0.0254 mm)
6	Fiber assembly	Use 4 Newport Manual Micropositioner with dual coated fiber holders and a Pneumatic epoxy dispensing system (PSI: 30psi, 0.5 sec), cure: UV 30 sec (twice), then thermal cure (ramp up 125°C in 15-20 minutes)	Fiber: SMF28, tapered, lensed Epoxy part number: EMI OPTOCAST 3410
7	Package Cleaning	Argon Plasma, 400W, 250mTorr, 30minutes and IPA	Kovar with Nickel Plating from Olin Aegis
8	Glue Ceramic board on Package	Epoxying the ceramic board on cleaned substrate, cure at 150°C for 1 hour (or cure at 125°C for 2 hour and 100°C for 4 hour , for sleeve safety)	Epoxy part number:84-1 LMI Manufacturer: Ablesteik
9	Fiber	Slide in the 900 um sleeves to	

	Protection	protect the fragile SM fiber, support the weight of the fiber in all handing from now on	
10	Package wire bonding	Attach and wire bond the substrate into the package	4 Au/Si, I mil diameter wires
11	Lid Hole Drill	Drill a hole on lid for back-fill Nitrogen in hermetic seam. Diameter of hole is: 20 mil (0.508 mm)	
12	Lid Glue	1) Glue lid onto package and cure at 150°C for 1 hour (or 125°C 2 hour and 100 °C, 4 hour) 2) Apply epoxy on four lid slots and cure at 125°C for 2 hour and make sure no sharp edge stick out of epoxy before let it touch fibers	Epoxy part number:84-1 LMI Manufacturer: Ablesteik Epoxy Part number: 2420 (or 2440) Manufacturer: 3M Scottish
13	Hermetic Sealing	Put the whole package in a petrel dish, then put petrel dish into vacuum bake chamber and bake at 125°C, 20 mTorr overnight to remove all the moisture; then Nitrogen cavity purge, < 1psi, 10 sec	
14	Lid Hole Seam	Dispense sealant to both holes. UV exposure/cure.	

Table 5.2 The hermetic seal packaging evaluation.

Leakage	1×10^{-8} cc/sec^2
Du Point	-70 °C
Relative Humidity	98 %

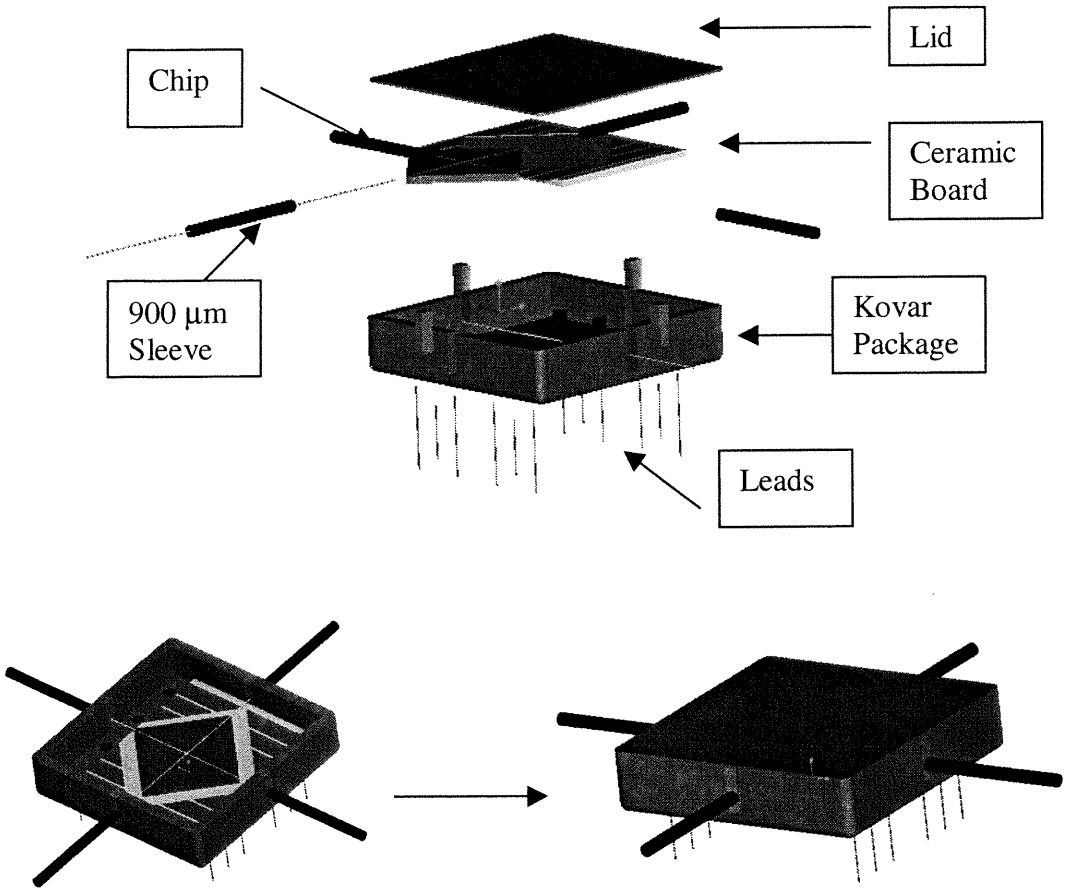

Figure 5.2 (a) The package procedures demonstrations.

Among package and assembly procedures, the active alignment, that is light signal is detected via laser detector through the alignment to monitor the alignment outcome prior to fixing, is the critical step for switch overall performance. The process control is essential and it has to minimize effects on coupling of small

movements during fixing operation. Figure 5.3 shows the last TH fiber is being inserting into the alignment grooves during active alignment.

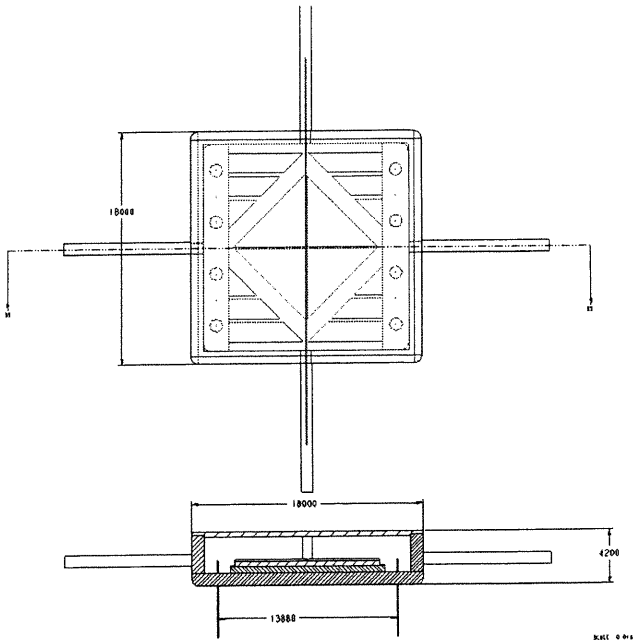

Figure 5.2 (b) The cross section view of the package.

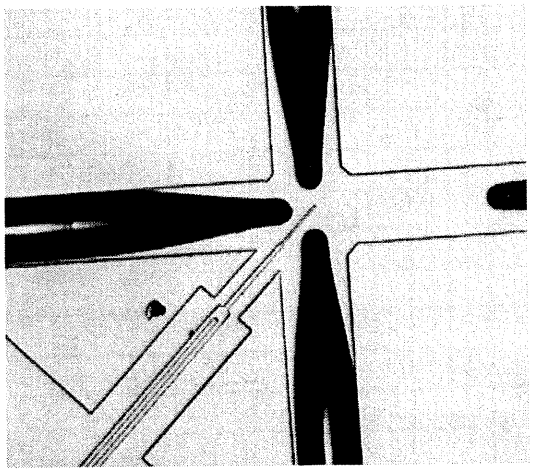

Figure 5.3 TH fiber insertion through active alignment.

In the active alignment, applying the epoxy is the key procedure. The epoxy used is Optocast 3410 from EMI. The dispensing force applied is about 30 PSI to ensure small enough drop of epoxy that can fix the fiber onto chip without covering the suspension structures. Figure 5.4 is the assembled chip after applied epoxy.

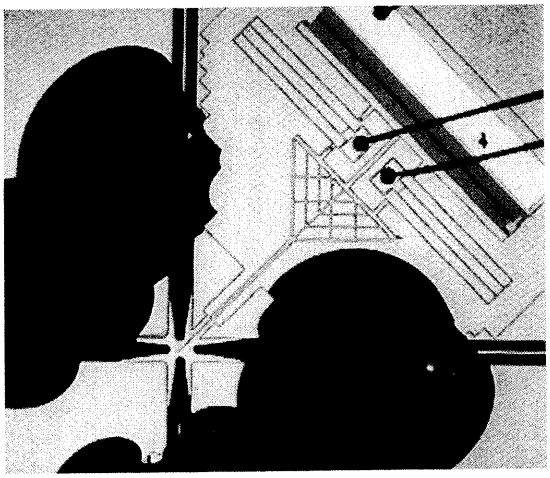

Figure 5.4 Assembled chip showing epoxy drops.

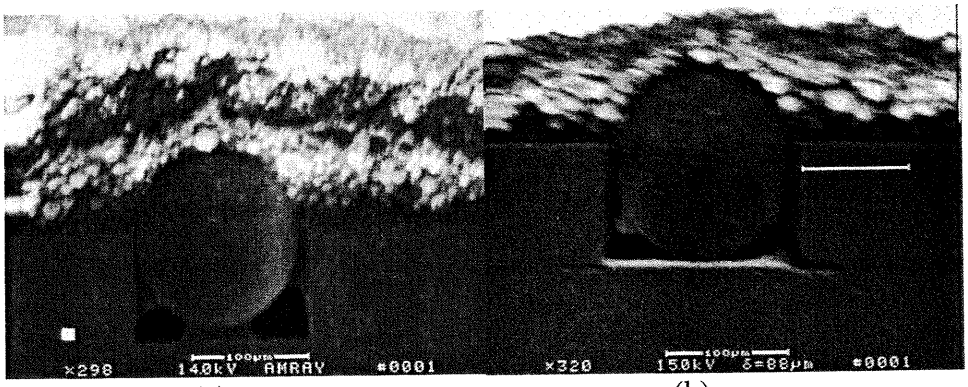

(a) (b)

Figure 5.5 The cross section of aligned TH fibers. (a) Lifted fiber. (b) Perfect fixed fiber.

If the fiber inserted is not fully attaches the alignment groove bottom, the epoxy will life up the TH fiber by filling in the trench so that the TH fiber can not be well aligned in Z direction. Figure 5.5 (a) shows the epoxy under the TH fiber, while Figure 5.5 (b) shows a TH fiber being fixed into the alignment trench nicely.

Figure 5.6 demonstrates the photos at two packaging stages such as the fabricated switch chip (Figure 5.6 (a)), and the chip-on-boards (Figure 5.6 (b)). The body of the package is made from Kovar (an iron-nickel-cobalt alloy) coated with gold through which 6 Kovar leads (with gold coating) penetrates. The lid is the last item to be sealed with soldering. The packaged switch performance will be tested in the next section.

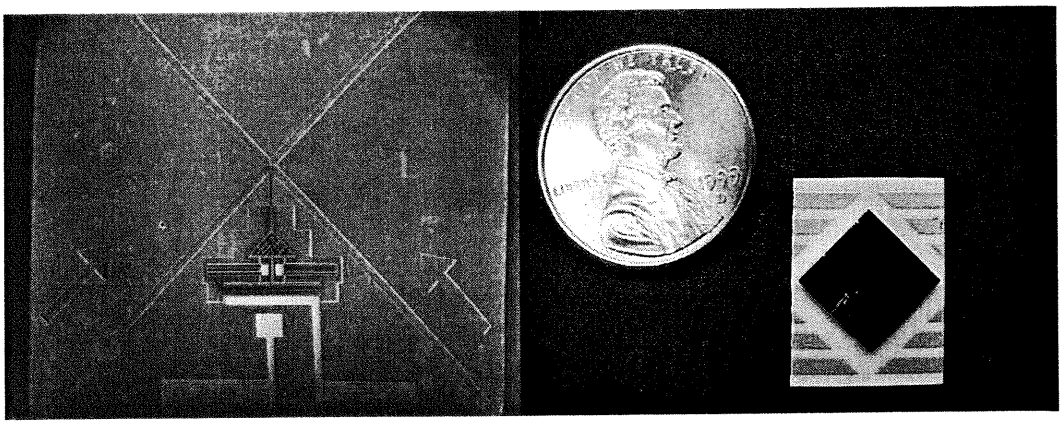

(a) (b)

Figure 5.6 The photos that are taken through packaging. (a) The switch chip (b) Chip on ceramic board.

2. SWITCH PERFORMANCE TESTING

The primary switching parameters are tested in this section including insertion loss, crosstalk, return loss, and directivity and switching speed.

2.1 Optical Properties

Insertion loss, return loss, directivity and cross talk are the primary optical properties that need to be tested to evaluate the switch performance.

The distribution of optical power through switch can be described, in an abridged form[1] , by two transfer matrices. The T matrix collectively represents the on-state paths (worse-case transmission), and the T° matrix collectively represents the off-state paths (worse-case crosstalk and return loss). For 2 x 2 switch the matrices can be written as below

$$T = \begin{bmatrix} t_{11} & t_{12} & \cdot & \cdot & \cdot & t_{1n} \\ t_{21} & \cdot & \cdot & \cdot & \cdot & t_{2n} \\ \cdot & \cdot & \cdot & \cdot & \cdot & \cdot \\ \cdot & \cdot & \cdot & t_{ij} & \cdot & \cdot \\ \cdot & \cdot & \cdot & \cdot & \cdot & \cdot \\ t_{n1} & \cdot & \cdot & \cdot & \cdot & t_{nn} \end{bmatrix} \qquad (5\text{-}1)$$

$$T^0 = \begin{bmatrix} t_{11}^0 & t_{12}^0 & . & . & . & t_{1n}^0 \\ t_{21}^0 & . & . & . & . & t_{2n}^0 \\ . & . & . & . & . & . \\ . & . & . & t_{ij}^0 & . & . \\ . & . & . & . & . & . \\ t_{n1}^0 & . & . & . & . & t_{nn}^0 \end{bmatrix} \tag{5-2}$$

Each coefficient t_{ij} is the worse-case (minimum) fraction of power transferred from port i to port j for any state with path ij switch on. Each t^0_{ij} is the worse-case (maximum) fraction of power transferred from port I to port j for any state with path ij switch off. The subscript $n = M + N$ is the total number of switch ports. Note that an $M \times N$ switch is described by an $n \times n$ square matrix having n^2 elements, and each element corresponds to the worst-case optical path (over all possible optical paths) through the switch.

The worse-case power at any output port, P_j, can be found by multiplying the power at any input port, P_i, by the transfer coefficient

$$P_j = P_i t_{ij} \tag{5-3}$$

All of a switches optical characteristics, such as insertion loss, L_{ij}, crosstalk, C_{ij}, and return loss, R_i and directivity, D_{ij}, can be defined in terms of its transfer coefficients as follows

$$L_{ij} = -10\log t_{ij} \qquad if\,(i \le M)and(j > M)or(i > M)and(j \le M) \tag{5-4}$$

$$C_{ij} = 10\log t_{ij}^0 \qquad if\,(i \le M)and(j > M)or(i > M)and(j \le M) \tag{5-5}$$

$$R_i = 10\log t_{ij}^{o} \qquad if\,(i = j) \tag{5-6}$$

$$D_{ij} = -10\log t_{ij}^{0} \qquad if\,(i \le M)and(j \le M)or(i > M)and(j > M) \tag{5-7}$$

If i and j are input and output ports in an on-state, respectively, then L_{ij} ((in positive dBs) is the insertion loss. If i and j are input and output ports in an off-state, respectively, then C_{ij} (in negative dBs) is the crosstalk. If both i and j are the same input/output port, the R_i (in negative dBs) is the reflectance of the port (return loss). Finally, if both i and j are input (or output) ports, then D_{ij} (in positive dBs) is the directivity between ports.

Uniformity is defined as,

$$\Delta L = \max\left|10\log(t_{ij}/t_{ik})\right| \qquad Here,(i \le M, j > M)and(k > M)or(i > M, j \le Mandk \le M) \tag{5-8}$$

For 2 x 2 switch, $M=2$, $N=2$ and $n=4$ (Figure 5.7 for switch ports configurations) so that T is a 4 x 4 matrix. Ignoring the off-state matrix and corresponding crosstalk coefficients, and assuming the reflectance and directivity coefficients are the same in both the on-state and off-state matrices, we can consider only the on-state matrix. The insertion loss coefficients in the on-state matrix correspond to crosstalk coefficients in the off-state matrix, which is not shown.

$$T = \begin{bmatrix} R_{11} & D_{12} & L_{13} & L_{14} \\ D_{21} & R_{22} & L_{23} & L_{24} \\ L_{31} & L_{32} & R_{33} & D_{34} \\ L_{41} & L_{42} & D_{43} & R_{44} \end{bmatrix} \tag{5-9}$$

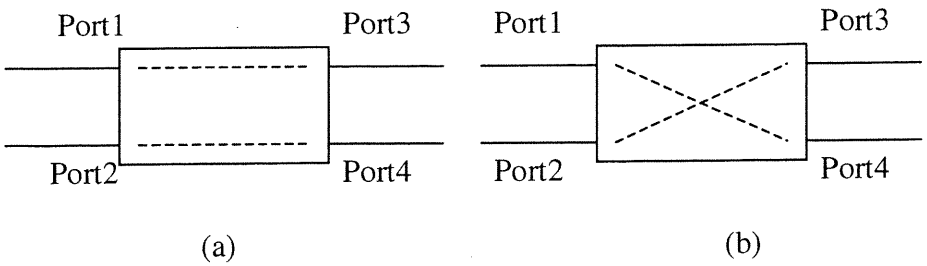

Figure 5.7 2x2 switch configurations. (a) Bar state: Port 1 to 3 and Port 2 to 4 on, while Port 2 to 3 and Port 1 to 4 off. (b) Cross state: Port 1 to 4 and Port 2 to 3 on, while Port 1 to 3 and Port 2 to 4 off.

The layout in Figure 5.8 is set for the insertion loss measurement.

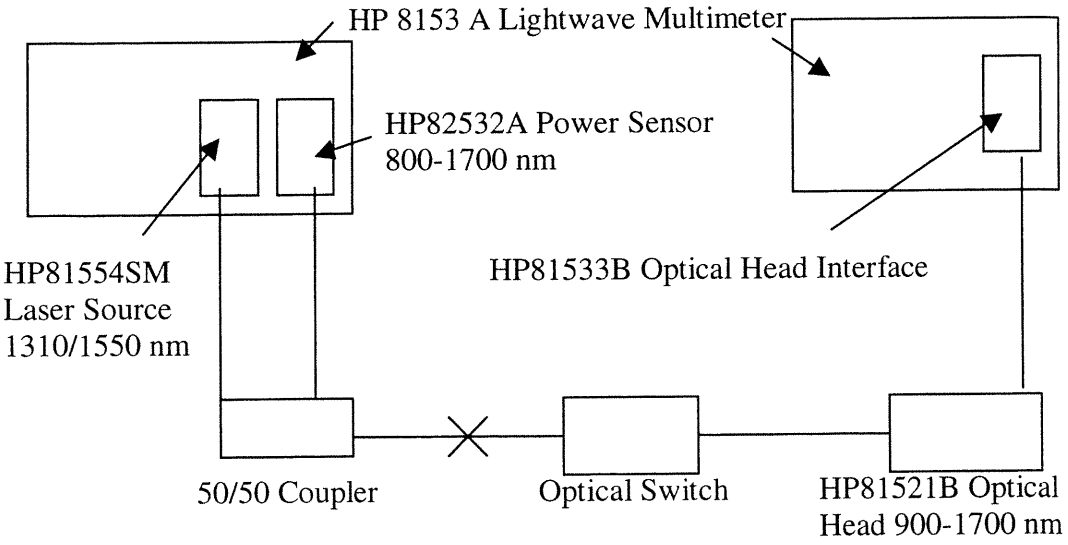

Figure 5.8 Optical property testing setup.

In Figure 5.8's setup, the HP82532 is used to detect the return loss signals, while the HP 8153A with HP 81533B optical head interface is used for insertion loss

meter. For crosstalk and directivity measurement, the fiber from corresponding measurement port needs to be spliced with the HP 81532B optical head input fiber and still the HP 8153A with HP 81533B optical head interface can be used as signal detector.

The optical property measurement results can be present in T matrix of equation (5-9) as follow

$$T = \begin{bmatrix} 10^{-5} & 10^{-5} & .85 & .56 \\ 10^{-5} & 10^{-5} & .56 & .85 \\ .85 & .56 & 10^{-5} & 10^{-5} \\ .56 & .85 & 10^{-5} & 10^{-5} \end{bmatrix} \qquad (5\text{-}10)$$

From above coefficients obtained from the measurements, the switch characteristics are calculated as:

The insertion losses for bar state (light pass straight through) , $L_{31} = L_{13} = 0.71\ dB$.

For cross state (light reflected off from the mirror), $L_{14} = L_{41} = L_{32} = L_{23} = 2.5\ dB$.

The return losses, $R_{11} = R_{22} = R_{33} = R_{44} = -50\ dB$.

The directivities, $D_{12} = D_{21} = D_{34} = D_{43} = -50\ dB$.

The cross talks, for cross state at off, $C_{14} = C_{23} = -34\ dB$, and for bar state at on, $C_{13} = C_{24} = -30\ dB$.

The uniformity, $\Delta L = 10log\ (0.85/0.56) = 1.8\ \Delta dB$.

To evaluate the packaging results, the insertion loss is monitored through the assembly and packaging process . The results show that the variation before packaging and after for the insertion loss is about 0. 3 dB. The causes of this variation are two folds, one is the epoxy applied on TH fiber will expand with heat during packaging, which will slightly change the TH fiber position; another is the refractive index of TH fiber itself also will change with temperature that can lead to the coupling efficiency variations. To avoid the loss variation, continuing to search for epoxy that have low CTE number (thermal expansion coefficient) with right viscosity and low evaporate rate is the key.

2.2 Switching Speed

The state transition time coefficients $S_{ij,}$ can be found by monitoring the switch's detected optical output using an oscilloscope triggered on the switch control signal. S_{ij} must be measured with a high-speed photodetector and a high bandwidth oscilloscope, such that the instrumental response is much (3 or 4 times) faster than the measurement time range. However, if not negligible, the transition time of the control signal or pulse used to switch path ij on or off, and the response times of the photodetector and oscilloscope, may have to be excluded from the measured results. In this case, the following approximate expression could be used

$$S_{ij} = \sqrt{t_{obs}^2 - t_{inp}^2 - t_{\det}^2 - t_{scope}^2} \qquad (5\text{-}11)$$

Where, t_{obs} is the transition time of optical output observed on scope, t_{inp} is the control signal transition time, t_{det} is the detector response time and t_{scope} is the oscilloscope response time.

In the measurements, the switching time is the observed time ignoring the rest of the instrumental response time that contributes on the switching delays. The switching measurement setup is despite in Figure 5.9 and Figure 5.10 demonstrates the switch in testing. (a) is at its initial position and (b) is at mirror retracted position when power is on. The switching speed measured by using established setups is 1 ms. Figure 5.11 is the signal response shown on oscilloscope. The switch on and off speed are both less than 1 ms, which is outperformed than all the current optical switch.

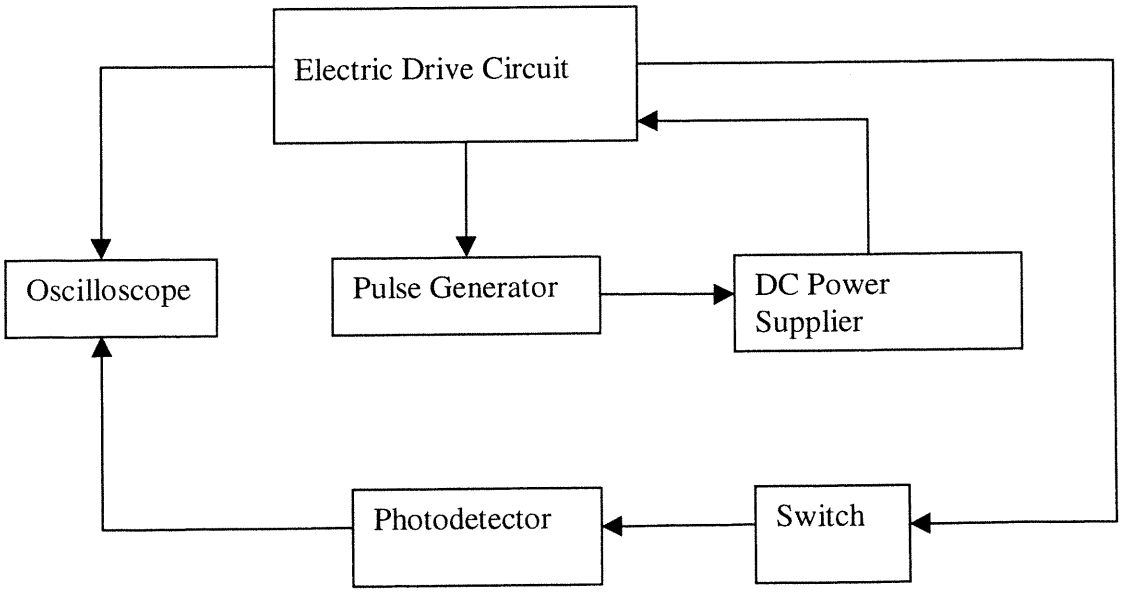

Figure 5.9 Switching time measurement layout.

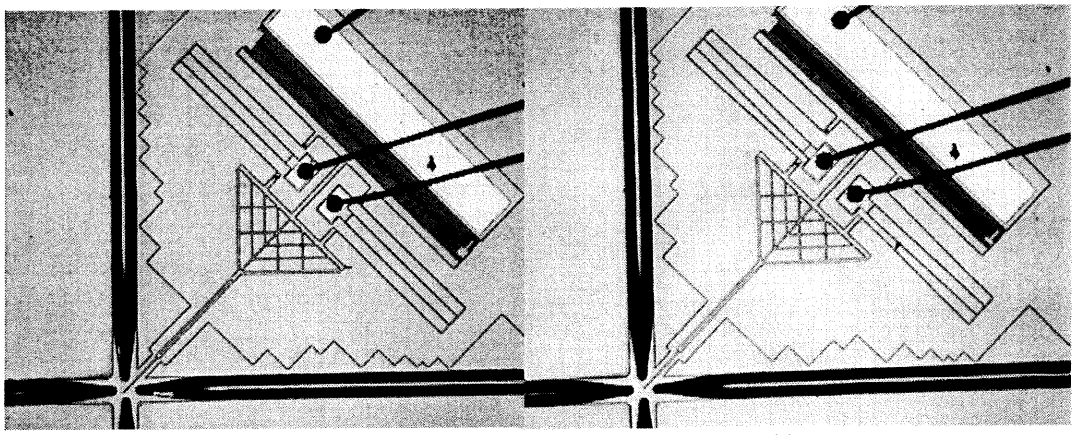

(a) (b)

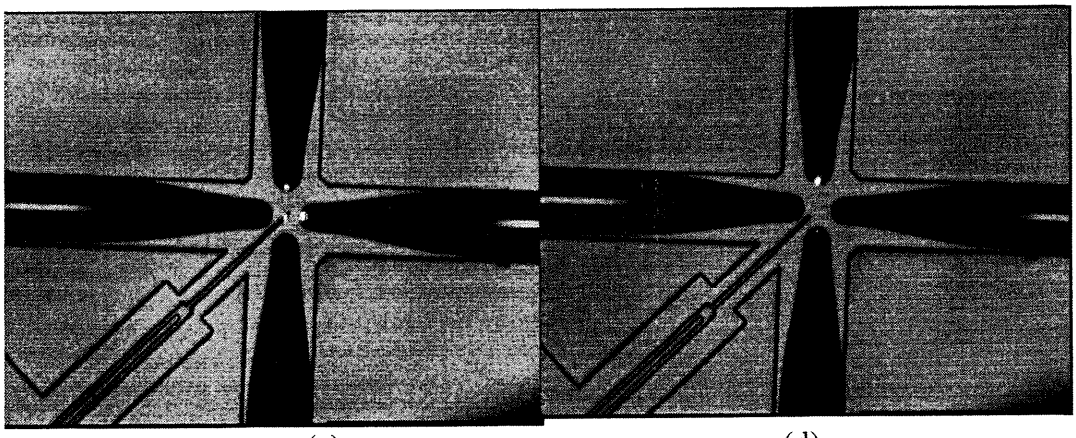

(c) (d)

Figure 5.10 The switch in testing: (a) when power off; (b) when power is applied; (c) when reflecting channel on; (d) when straight through channel on.

When the switch is driven up to 3 kHz, there is no structural damage, mechanical stickiness are observed. Therefore, the switch features the very fast switching speed and very durable mechanical structures. The lifetime cycling has not been done at this point.

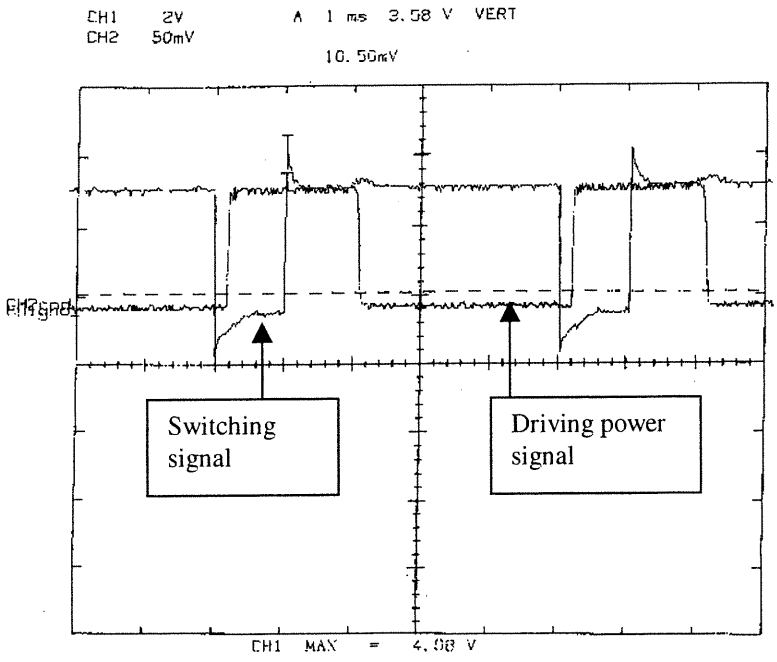

Figure 5.11 The switching response signals vs. the driving power signals.

3. SUMMARY

The key technique hurdles in the assembly and packaging process are overcome including the TH fiber insertion, active alignment, epoxy fixing and hermetic sealing. The hermetic sealing is still very preliminary and needs more testing data to prove its reliability and consistency.

After assembly the minimum insertion loss that can be obtained at bar state is 0.7 dB and 2.5 dB at cross state. The return loss is over 50 dB, cross talk is about 34

dB and switching speed is 1 ms. Those numbers can be drastically improved by applying AR coating on the tip of the TH fiber to reduce the insertion loss while minimize the reflectance on the fiber.

However, if comparing the switching speed results with transient analysis, the measured speed is much faster than the simulation data. This differentiation is probably resulted from the electric circuit design. In ANSYS simulation, the impact of the electric drive circuits on the switching transient behavior is ignored due to the software constrains. In reality, the driving power does influence on the switching performance, particularly the switching speed. Also, the damping ratio of 0.5% in the ANSYS transient simulation is only an estimated damping ratio from the literature research. The changing of the damping ratio have a big impact on transient behavior, too. Therefore, ANSYS current version is more suitable for coupled field transfer function simulation rather than the transient analysis. To solve transient analysis problem combine with electric drive circuit integration, the MEMSPro, a MEMS specific software for system simulation, has been implemented. The detail simulation work on the electric circuit design will not be covered in this thesis.

REFERENCES:

1 **BELLCORE,** *Generic Requirements for Fiber Optic Switches,* Bellcore, TR-NWT-001073, 1994.

CHAPTER 6: CONCLUSION

In this chapter a conclusion of the work through this thesis is given out. The future research directions are also discussed.

1. THESIS REVIEW

In this thesis, a MEMS 2 x 2 optical switch has been developed and demonstrated with strong performance in terms of the very large actuation displacement (> 55μm), high switching speed (1ms) and low insertion loss (0.7 dB min.) by using bulk micromachining technology.

The ANSYS FEM simulation tools have been employed to analyze the electrostatic comb drive actuator design and optimization. The coupled field Finite Element modeling (FEM) simulations of the comb drive actuator, including static stiffness analysis (spring constant), model analysis (resonant frequency), electrostatic analysis, and coupled-field simulation for transfer function (driving voltage) and model transient behavior analysis.

The optimized actuator has a double-folded beam suspension structure with 3 μm beam width and 790 μm beam length. The supported beams demonstrated a durable mechanical structure and stable driving motion. When the actuator is driven

by a pulse generator at a frequency of 3 kHz, there is no mechanical damage, fatigue or stickiness observed. The coupled-field simulations show a consistent result with the experimental measurements, and thus reduce the development cycle time. The force that required for a displacement of 55 μm with the designed actuator is 68 μN. With the designed comb fingers, a driving voltage of 68 volts will be needed for this 55 μm displacement.

A simple, high-yield, and IC compatible fabrication sequence has been developed for switch chip processing, in which the key process, deep dry ICP etching, has been studied extensively with varying characterization tools including SEM, AFM, Dektak and microscopies. The mirror fabricated with modified Bosch deep dry etching process has a surface roughness of 15 nm (20 nm typical) and vertical profile of 90 ° ± 0.1°. The fabrication sequence features one-step etching for mirror, actuator and alignment grooves as well, which ensures an optimized optical alignment and the processing simplicity and thus drastically improve the wafer yield and performance reliability. With the developed Deep ICP etching, a high aspect ratio of 1: 25 is achieved with very well controlled etching profile, such as, etching rate, undercutting, micro-loading effect, etc. Both double coating technique and protection walls, introduced in this thesis, contribute to this outstanding result.

The TH fiber is first introduced in this work for MEMS optical switching application. Vytran splicing machine has been utilized for TH fiber fabrication. The lenses with diameters of in the range from 23 μm to 55 μm are achieved. However,

the potential of this technique is not limited in this range of lens diameter. The reproducibility of TH fiber fabricated with this technique is very high. The tolerance of TH fiber lens diameter is about ±1 μm, while the tolerance for tapered length is about ±16 μm. The coupling losses between two the TH fibers are concentrated in a range of 0.75 dB to 0.5 dB. The lowest coupling loss of 0.44 dB has been achieved. To our knowledge, this is so far the lowest coupling loss ever reported with tapered fibers. Also it is the only micro component developed that does the collimating and signal coupling with such a low loss and such a high reproducibility. The parameters such as optimized coupling separation, Raleigh Ranges, and beam width are all characterized to meet the switching assembly requirement. The optimized coupling separation between two TH fibers is about 85 μm, the Raleigh Ranges are 46.46 μm at 1299.4 nm and 18.08 μm at 1553 nm, the beam spot for 1299.4 nm and 1553 nm are 7.77 μm and 5.30 μm, respectively. Those parameters are much desired by the switch alignment and assembly.

Another important feature of the TH fiber is the increasing the misalignment tolerant. The TH fiber, in the axial direction, after misalignment of 10 μm from its optimized position, a 2.5 dB additional loss is measured, while in the lateral direction the misalignment suffers a tight tolerant. An additional loss of 2 dB occurs after a misalignment of 0.5 μm.

The beam propagation properties are characterized both inside, outside the TH fiber, and in free space. The effect of hemisphere lens on the beam

transformation has been described. Several equations have been given out to discuss the light propagation with TH fibers. The beam propagation in free space abides the Gaussian distributions, while inside the tapered region a Gaussian beam approximation also can be deployed. The beam width is inverse proportional to the core diameter. The hemisphere lens can be viewed as a thin lens which will change the phase properties of the Gaussian beam while keep its amplitude. The beam profile measurement results are well following the theoretical predictions.

Finally the chip are assembled with developed TH fiber by a Newport optical alignment system. And then packaged with hermetic sealing. With the packaged MEMS switch, the 0.7 dB insertion loss with 1 ms switching speed has been achieved.

2. FUTURE WORK

Although this MEMS 2x2 optical switch has been completed from design to final package; many technical challenges involved have been overcome through the development; and it fulfilled the performance that other MEMS switch can not deliver, there are still a lot ahead that need to be extensively studied in the future.

Firstly, with the current design, when power off, the mirror is in the reflective position, when power on the mirror retried from the optical path and the light pass straight through. To save the power consumption, a reverse perform is

desired, i.e., when power on, the mirror move into the optical path and reflects the light, when power off it is in its initial retrieval position. Figure 6.1 is a design idea that can accomplish this functionality. However, further FEM simulation, and fabrication development needs to be carried out.

Secondly, with the current design the mirror thickness is 5 μm. This thickness will lead to the light offset when it reflects off the mirror so that it increases the insertion loss at the reflective state. To solve this problem, a possible solution is given out in Figure 6.2. With one built-in micro-mirror on each side of the moving mirror, the reflective light can be re-direct in the perfect alignment direction. Of course, this solution may cause some loss from the two more surface absorption. A more simple solution has been given out by author lately, the results of which has been described in a patent application [1].

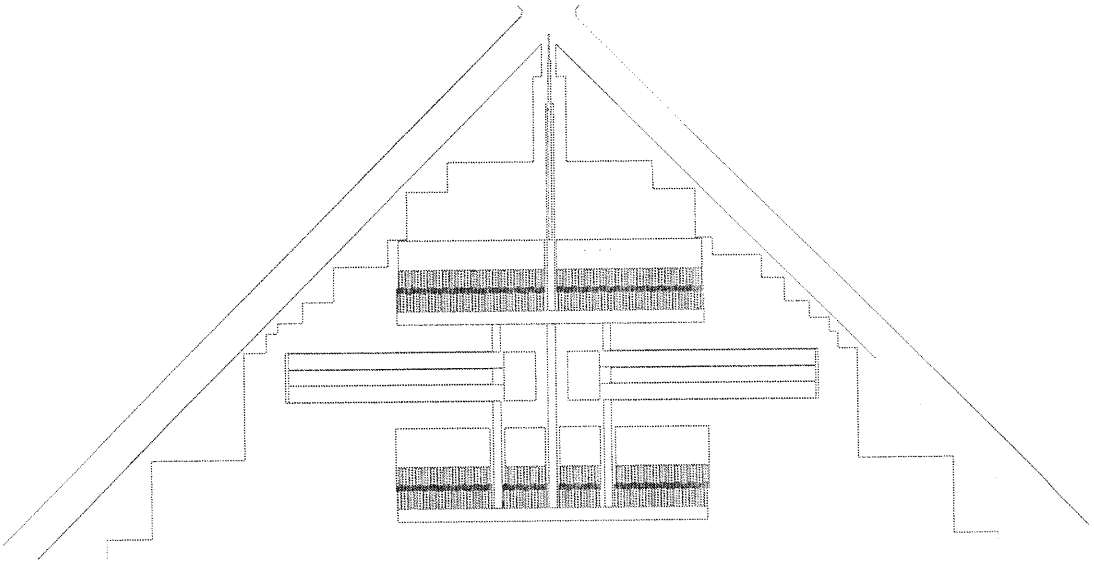

Figure 6.1 The Power consumption reduction design.

Thirdly, the return loss is largely due to the air gap between the launching and receiving TH fibers. To reduce improve the return loss, a refractive index matching oil needs to be filled in the gap. However, introducing the matching oil required the on-chip hermetic sealing. This will leave to the future work.

Lastly, 2 x 2 layout is only one of the possible configuration that can be carried out with this technology. There are more switching configuration needs to be explored, such as 1 x 3 (Figure 6.3 (a)), 1x 9 (Figure 6.3 (b), 1x 2, 1x 4 and 4 x 4 (Figure 1.3). Among them compact 1x 4 switch layout, which has been described in Ref 2, will not be shown in graphic. Large matrix switch is also possible to be built with this 2x2 design after implement the waveguide technique and the index matching oil to reduce the each stage insertion loss. Figure 6.4 the some matrix switch fabric configurations that can be made of this 2x2 switch design.

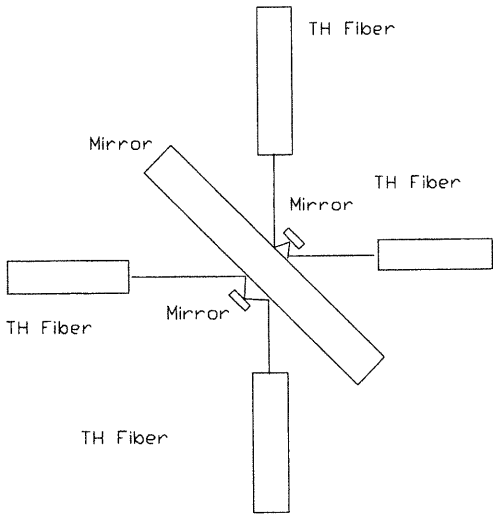

Figure 6.2 The schematic draw for reflective path correction.

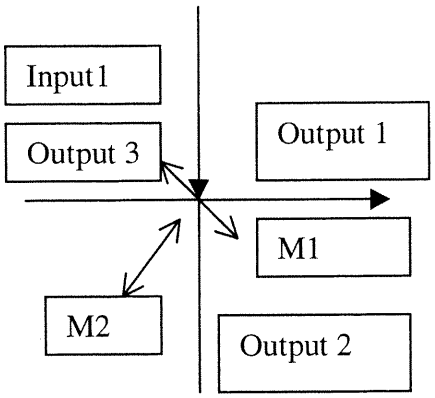

Input 1-to output2 as shown when mirror 1 (M1) is inserted.

(a)

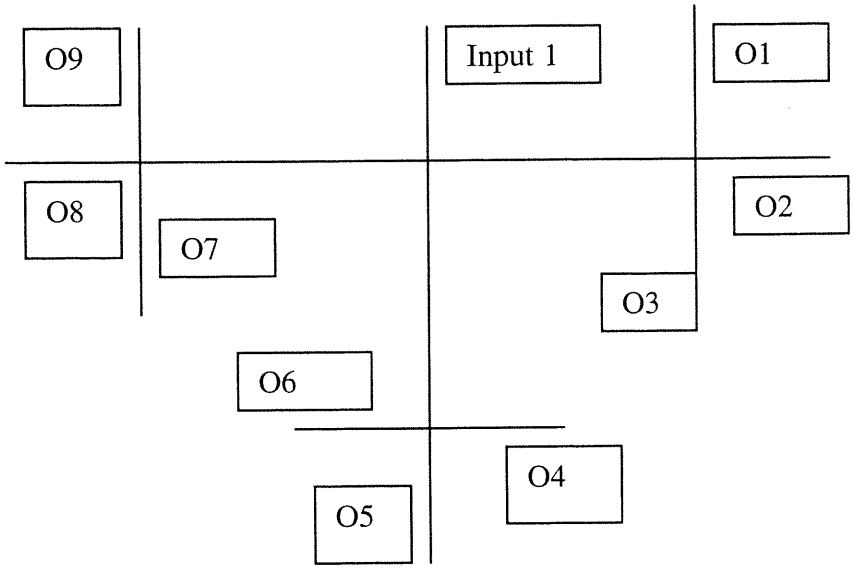

(b)

Figure 6.3 Two 1 x n switch configurations: (a) 1 x3 with two actuator on chip; (b) 1x9 switch built from 1x3 in (a) by cascading.

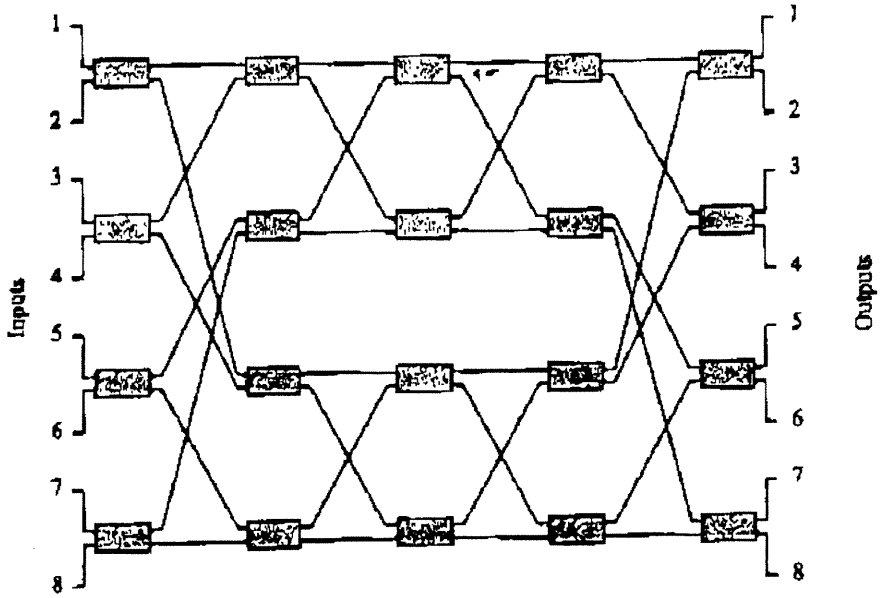

(a)

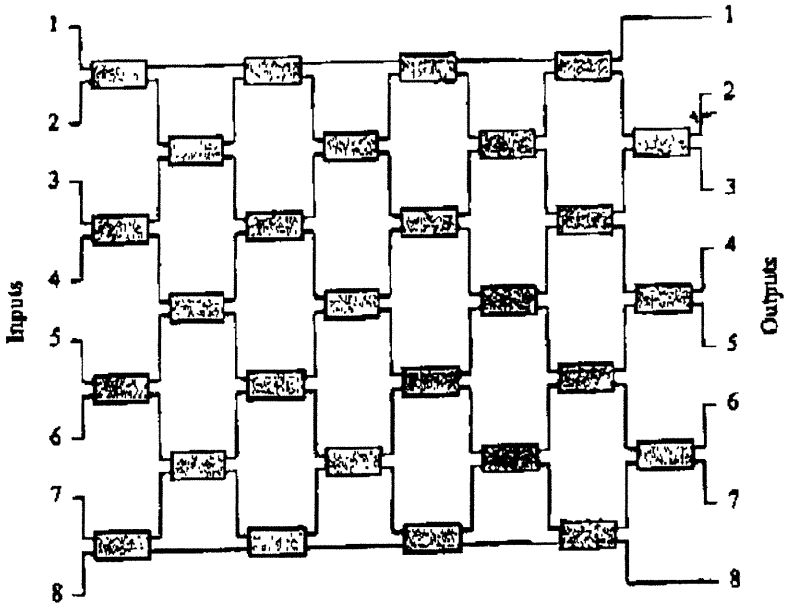

(b)

Figure 6.4 Examples of matrix switches built with 2x2 elements. (a) is a rearrangeable nonblocking 8x8 switch realized using twenty 2x2 switches interconnected in the Benes architecture; (b) is a rearrangeable nonblocking Spanke-Benes architecture built with twenty-eight 2x2 switches.

In conclusion, this 2 x 2 MEMS switch features fast switching speed, low insertion loss, integration compatible processing, wavelength transparency, compact packaging design and easy of assembly. It can find wide applications in all optical networking, such as multiple line switching protection, dynamic gain equalization and VOAs. Particularly, it is very suitable for OADMs, a key enabler for metro DWM optical networking, which requires the fast switching speed (less than 1 ms) and most likely requires the switches that can be integrated with other optical components, such as WDM multiplexer, demultiplxer, and VOA, etc. To our knowledge, none of the currently available switches can meet such requirements. This MEMS 2 x 2 is very promising for OADMs application.

REFERENCES:

1 **Zhang, N.,** *Improvement of Switch Output Channel Uniformity by Using On-chip Optical Path Balance Approach Thereby*. 2000.

2 **Zhang, N.**, *Compact 1x4 Optical Switch Design on Single MEMS chip Thereby*. 2000.

BIBLIOGRAPHIE:

Amitay, N., Presloy, F.V., *Optical Fiber Tapers-A Novel Approach to Self-aligned Beam Expansion and Single-mode Hardware*, J. Light. Tech., (1987), LT-5(1), 70-76.

Bau, H.H. de Rooij, N.F., Kloeck, B., *Mechanical Sensors* (Sensors-a Comprehensive Survey 7) (1994) (Weinheim).

BELLCORE, *Generic Requirements for Fiber Optic Switches,* Bellcore, TR-NWT-001073, 1994.

Bhardwaj, J.K., **Ashraf**, H., Advanced Silicon Etching Using High Density Plasma, Proc SPIE, 2639, (1998), 224-233.

Binnig, G., Quate, C.F., *Gerber,C., Phys.Rev.Lett.,* 56, (1986), 930.

Buser, R.A., *Theoretical and Experimental Investigations on Silicon Single Crystal Resonant Structures*, PhD Dissertation University of Neuchatel.

Campbell, S. A., *The Science and Engineering of Microelectronic Fabrication*, Oxford University Press, New York, 1996.

CIR, *Optical Switching Bazzar,* Optical Watch, (2000), **3**, 1-3.

Coburn, J.W., Winters H.F., *Conductance considerations in the reactive ion etching of high aspect ratio features*, Appl. Phys. Lett. 55(26), (1989), 2730-2732.

Davies, D.A.O., Fisher, M.A., *Integrated Lossless InGaAsP/InP 1-to-4 Optical Switch,* IEEE J. Quantum Electronics, 1994, **30 (3),** 717-723.

Dutta, R., Rouskas, G.N., *A Survey of Virtual Topology Design Algorithms for Wavelength Routed Optical Networks*, Optical Networks, (2000), 1 (1), 73-88.

Elmirghani, M.H., *All-Optical Wavelength Conversion: Technologies and Applications in DWDM Networks*, IEEE J. Communications, (2000), 3, 1-9.

Esashi, M. *High-rate directional Deep Dry Etching for Bulk Silicon Micromachining*, J. Micromech. Mircoeng., (1995), 5, 5-10.

Fan, L.S., Tai, Y.C., Muller, R.S., " *IC-Processed Micro-Motors Design, Technology, and Testing,*" Tech. Dig. IEEE Micro Electro Mech. Syst. Workshop, Salt Lake City, UT, Feb. 20-22, (1989), 1-6.

Gardner, J.W., *Microsensors: Principles and Applications* , (1994) (Chichester: Wiley).

Gardner, J.W., *Microsensors: Principles and Applications*, John Wiley & Sons, New York, 1995.

Gere, J.M., Timoshenko, S.P., *Mechanics of Materials*, PWS, 1997, Forth Edition.

Ghani, N., Dixit, S., Wang, T., *On IP-over-WDM Integration*, IEEE J. Communications, (2000), **3**, 13-26.

Gile, C.R., Aksyuk, V., Barber, R., *A Silicon MEMS Optical Switch Attenuator and Its Use in Lightwave Subsystems* IEEE J Selected Quantum Electronics, (1999), **5(1),** 18-25.

Gloge, D., *Weakly Guiding Fibers,* Appl. Opt., (1971), 10(10), 2252-2258.

Granestand, P., *Integrated Optics 4x4 Switch Matrix with Digital Optical Switches*, Electronics Letters, (1990), **26 (1),** 4-5.

Granestrand, P., *Strictly Non-blocking 8x8 Integrated Optical Switch Matrix in Ti:$LiNbO_3$*, Topical Meeting on Integrated and Guided Wave Optics, Opt. Soc. Am., 1986.

Gyimesi, M., Ostergaard, D., *"Electro-Mechanical Transducer for MEMS Analysis in ANSYS"*, Proc. ICCAD, IEEE, (1999) 283-286.

Harris, F.S.Jr., Tavennel, M.S., Mitchell, R.L., *Single-Slit Fresnel Diffraction Patterns: Comparison of Experimental and Theoretical Results*, J. Opt. Soc. Am., (1969), 59(3), 293-296.

Hirano,H., Furuhata, T., Gabriel, K.J., *Design, fabrication, and operation of submicron gap comb-drive microactuators,*J. Microelectromechanical system, 1(1), (1992), 52-58.

Hiroyyuki, F., Hiroshi, T., *Micro Actuators and Their Applications*, Mircoelectronics Journal, (1998), **29,** 637-640.

Hirth, P., Knodel, D., *Ein Digital Fernsprechanschlub Fur Lichtwellenleiter und Kupferkabel,* TE KADE, Tech. Mitt., (1981), 40-46.

Hoanca, B., Dubovitsky, S., *All-Optical Routing Using Wavelength Recongnizing Switches,* J. Lightwave Technology, (1998), 16(12), 2254.

Howe, R.T., Boser, B.E., Pisano, A.P., *Polysilison Integrated Microsystems:Technologies and Applications* Sensors Actuators, (1996), A 56, 167-77.

Huang Y.T., *Polarization-Independent Optical Switch Composed of Holographic Optical Elements*, Optical Letters, (1995), **20 (10),** 1198-1200.

Huang, L.S., Lee, S.S. Motamedi, E., Wu, C., *Optical Coupling Analysis and Vibration Characterization for Packaging of 2x2 MEMS VerticalTorsion Mirror Switches,* Proceedings of SPIE, (1998), **3513,** 135-143.

Jaecklin, V.P., Linder, C., de Rooij, N.F., Moret, J.M., *"Micromechanical Comb Actuators with Low Driving Voltage"*, J. Micromech. Microeng., 2 (1992), 250-255.

Jansen, H., de Boer, M., Elwenspoek, M., *The Black Silicon Method VI: High Aspect Ration Trench Etching for MEMS Applications*, Proc. 9th IEEE Workshop on MicroElectro Mechanical Systems, MEMS'96 (San Diego, CA, 1996), 250-7.

Jedrzejewski, K.P., Martinez, F., Minelly, J.D., Hussy, C.D., Payne, F.P., *Tapered-Beam Expander for Single-Mode Optical-fiber Gap Devices,* Electronics Letters, (1986), 22(2), 105-106.

Jin, X. *Optical Fiber Index Taper-Theoretical Analysis and Experiment Demonstration,* International J. Infrared and Millimeter Waves, (1998), 19(6), 875-886.

Juan, W.H., Pang, S.W., *Batch-Micromachined, High Aspect Ratio Si Mirror Arrays for Optical Switching applications,* Tech. Dig., Transducers'97, (1997), 93-96.

Keil, N., Yao, H.H., Zawadzki, C., *2x2 Digital Optical Switch Realised by Low Cost Polymer Waveguide Technology,* Electronics Letters, (1990), **32 (16),** 1470-1471.

Keil, R., Kiement, E., Mathyssek, K., Wittmann, J., *Experimental Investigation of the Beam Spot Size Radius in Single Mode Fiber Tapers,* Electronics Letters, (1984), 20(15), 621-622.

Khoe, G.D., Kock, H.G., Kuppers, D., Poulissen, J.H.F.M., DeVrieze, H.M., *Progress in Monomode Optical-fiber Interconnection Devices,* J. Lightwave Techno., (1984), LT-2(3), 217-227.

Khoe, G.D., *Practical Low-loss Lens Connector for Optical Fibers*, Electro. Lett., (1978), June 30, 163-164.

Kim, **C.J.**, **Pisano**, **A.P.**, **Muller**, **R.S.**, **Lim**, **M.G.**, *"Polysilicon Microgripper"* Tech Dig. IEEE Solid-State Sensor and Actuator Workshop, Hilton Head, SC, (1990), 48-51.

Kloeck, **B.**, *Design, Fabrication and Characterisation of Piezoresistive Pressure Sensors, Including the Study of Electrochamical Etch Stop* , PhD Dissertation University of Neuchatel, (1989).

Kuwahara H., Sasaki, M., Tokoyo, N., *Efficient Coupling from Semiconductor Lasers into Single-mode Fibers with Tapered Hemispherical Ends.*, Appl. Opt. (1980), 19(15), 2578-2583.

Ladany,I., Wdkstein, H.J., Botez, D., in the Processing of the IEDM,IEEE, New York, (1978).

Lee, **K.Y.**, **LaBianca**, **H.**, **Rishton**, **S.A.**, *Micromachining Applications of a High Resolution Ultrathick Photoresist,* J. Vac. Sci. Technol., (1995), B13, 3012-6.

Lee, **S.S., Huang, L.S.,** *Free-Space Micromachined Optical Switches Based on MEMS Vertical Torsion Mirrors,* J Lightwave Technology, (1999), **17(1),** 7-13.

Lin, L.Y., Goldstein, E. L., Simmons, J. M., Tkach, R. W., *High-Density Micromachined Polygon Optical Crossconnects Exploiting Network Connection-Symmetry,* IEEE Photonics Technology Letters, (1998), **10 (10),** 1425-1427.

Lin, L.Y., Goldstein, E. L., Tkach, R. W., *Free-Space Micromachined Optical Switches for Optical Networking,* IEEE J. Selected Topics in Quntum Electronics, (1999), **5 (1),** 4-9.

Lin, L.Y., Goldstein, E.L., Tkach, R.W., *Free-Space Micromachined Optical Switches with Submillisecond Switching Time for Large-Scale Optical Crossconnects,* IEEE Photonics Technology Letters, (1998), **10 (4),** 525-527.

Linder, C., Paratte, L., *Surface Micromachining* J. Micromech. Microeng., (1992), 2, 122-32.

Linder, C., Tschan, T., de Rooij, N.F., *Deep Dry Etching of Silicon:* a Novel Micromachining Tool , Sensors Mater., (1992), 3, 311-24.

Linder, C., Tschan, T., de Rooij, N.F., *Deep Dry Etching Techniques as a New IC Compatible Tool for Silicon Mircomachining,* Proc. Int Conf Solid State Sensors and Actuators TR (1991), 524-527.

Marchall, S., *New Applications Emerging as MEMS Technology Advances*, R&D Magazine, (1998), 32-37.

Marcus, D., *Light Transmission Optics*, Van Norstrand Reinhold, New York, N.Y. (1982).

Marcuse, D., *Loss Analysis of Single-mode Fiber Splices,* The Bell System Technical Journal, (1977), 56(5), 703-719.

Marcuse, D., *Theory of Dielectric Optical Waveguides*, (1974), Academic Press, New York.

Marxer, C., de Rooij, N.F., *Micro-Opto-Mechanical 2x2 Switch for Single-Mode Fibers Based on Plasma-Etched Silicon Mirrros and Electrostatic Actautor,* J. Lightwave Technolgy, (1999), **17 (1),** 10-17.

Marxer, C., Thio, C., *Vertical Mirrors Fabricated by Deep Reactive Ion Etching for Fiber-Optics Switching Applicatiosn*, IEEE J. MEMS, (1997), **6(3),** 275-278.

McVittie, J.P., **Gonzalez,C.**,*Anistropic Etching of Si Using SF_6 with C_2ClF_5 and Other Mixed Halocarbons*, Proc 5th Symp Plasma Processing-Electrochem Soc, (1985) 85-1, 552-567.

Mehregany, M., Nagarkar, P., Senturia, S.D., Lang, J.H., " *Operation of Microfabricated Harmonic and Ordinary Side-Drive Motors*", Tch. Dig. IEEE Micro Electro Mech. Syst. Workshop, Napa Valley, CA, Feb, 11-14, (1990), 1-8.

Muller, R.S., Howe, R.T., *Microsensors*, (1991) (New York: IEEE)

Nagase, R., *Silica-Based 8x8 Optical Matrix Switch Module with Hybrid Integrated Driving Circuits and its System Application*, J. Lightwave Technology, (1994), **12 (9),** 1631-1639.

Nicia, A., TE KADE, Tech. Mitt., (1981), 40-46

O'Connell, D., *Carries Banking on Optical Infrastructure,* Telecommunicaitons, (2000), **6**, S3-S5.

Odagiri, Y., Schikada, M., Kobayashi, K., *High-efficiency Laser to Fiber Coupling Circuit Using a Combination of a Cylindrical Lens and a Seltoc Lens*, Electron. Lett., (1977), 113, 345-396.

Ohnesorage, F., Binnig, G., Science, 260, (1993), 1451.

Okayama, H. Kawahara, M., Low-Crosstalk 2x2 Digital Optical Switch, Electronics Letters, (1994), **30 (5),** 403-405.

Okuno, M., Kato, K., Nagase, A., *Silica-Based 8x8 Optical Matrix Switch Integarting New Switching Units with Large Fabrication Tolerance*, IEEE J. Lightwave Technology, (1999), **17 (5),** 771-781.

Oliver, G.P., *The Integrated Services Digital Network,* IEE Conf. Publ., (1982), 209, 8-13.

Ostergaard, D., Gyimesi, M., Affour, B., "Efficient Reduced Order Modeling for System Simulation of Micro Electro Mechanical Systems (MEMS) from FEM Models" CAD, Design and Test, 1999.

Pang, C., *Dry Etching*, Short course at SPIE micromachining, 1999.

Private conversation

Ramaswami R., Sivarajan, K., *Optical Networks: A Practical Perspective, San Francisco*: Morgan Kaufman, 1998.

Ramaswami R., Sivarajan, K., *Routing and Wavelength Assignment in All Optical Networks*, IEEE/ACM Trans, Net., (1995), **3 (5),** 489-500.

Ristic, L., *Sensors Technology and Devices*, (Boston: Artech)

Riza, N., Polla, D., *Micromechanical Fiber-optic Switch s for Optical Networks*, Integrated Optics and Microstructures, (1992), **SPIE 1793,** 108-126.

Riza, N., Polla, D., *Microdynamical Fiber-Optic Switch and Method of*

Switching Using Same, US Patent 5208880, (1993).

Silvalingam, K, M., *Optical WDM Networks - Principles and Practice,* March, 2000.

Simmons, J.M., Saleh, A.A.M., Goldstein, .LY. Lin, *Optical Crossconnects of Reduced Complexity for WDM Networks with Bidirectional Symmetry*, IEEE Photonics Technology Letters, , (1998), **10 (10),** 819-821.

Snyder, A.W, Love J.D., *Optical Waveguide Theory*, (1983), Academic Press, New York.

Stewart, W.J., Love, J.D., *Design Limitation on Tapers and Couplers in Single Mode fibers*, Technical Digest IOOC-ECOC, (1985), 1, 559-562.24. **Payne F.P., Hussy C.D., Yataki, M.S.,** *Modeling Fused Single-Mode-Fiber Couplers,* Electronics Letters, (1985), 21(11), 460-462.

Sze S.M., *Semiconductor Sensors* (1994) (New York: Wiley)

Sze, S. M., *Semiconductor Sensors*, John Wiley & Sons, New York, 1994.

Takeshima, N., Gabrial, K.J., Ozaki, M., "*Electrostatic Parallelogram Actuators*" Dig. Tech. Papers, Transducers'91, San Francisco, CA, 63-66.

Tamura, Y., Maeda, H., Shikii, S., Yokoyama, B., *Single Mode Fiber WDM in the 1.2/1.3 Micron Wavelength Region*, IOOC-ECOC'85, (1985), 579-582.

Tang, W.C., *"Electrostatic Comb Drive for Resonant Sensor and Actuator Application"*, Ph.D. dissertation, University California, Berkeley, CA, 1990.

Tang, W.C., Nguyen, T.H., Howe, R.T., *"Laterally Driven Polysilison Rosonant Microstructures"* Tech. Dig. IEEE Micro Electro Zmech. Syst. Workshop, Salk Lake City, UT, Feb. 20-22, (1989), 53-59.

Temermeister, I., **Blayo, N.**, **Klemens, F.P.**, *Comparison of advanced plasma sources for etching applications,* J. Vac. Sci. Technol. B 12(4), (1994), 2310-2321.

Thylen, L., Karlsson, G., Nilsson, O., *Switching Technology for Future Guided WaveOptical Networks: Communication*, Academic Press, 1998.

Toshiyoshi, H., Fujita, H., *Electrostatic Micro Torsion Mirrors for an Optical Switch Matrix,* Journal of MEMS, (1996), **5 (4),** 231-237.

Toshiyoshi, **H., Miyauchi, D., Fujita, H,** *Electromagnetic Torsin Mirrors for Self-aligned Fiber-Optic Crossconnectors by Silicon Micromachining*, IEEE J Selected Topics in Quntum Electronics, (1999), **5 (1),** 10-17.

Trimmer, **W.S.N.**, **Gabriel**, **K.J.,** *"Design Considerations for a Practical Electrostatic Micro-Motor"*, Sensors and Actuators, 11 (1987), 189-206.

Tschan,**T.**, *Simulation, Design and Characterization of Silicon Piezoresistive Accerometer, Fabricated by a Bipolar-compatible Industrial Process*, PhD Dissertation University of Neuchatel, (1992).

US Patenet #5501893: *Method of Anisotropically Etching Silicon.*

Varghese, **M., Rabinovich**, **V.L.**, **Senturia**, **S.D.**, " *Reduced-Order Modeling of Lorentz Force Actuation with Model Basis Functions*", External customer exchange copy, 2000

Verhoeckz, N.A.M., Van Den Elzen, H.C., Snuders, W.A.M., Van Gerwen, P.J., *Digital Echo Cancellation for Baseband Data Transmission*, IEEE Trans., (1979), ASSP-27, 768-781.

Wagner, R., *Multiwavelength Lightwave Networks*, OFC'2000 Short Course, Maltimore, Maryland, 2000.

Wagner, R.E., Tomlinson, W.J., *Coupling Efficiency of Optics in Single-mode Fiber Components,* Appl. Optics, (1982), 21(5), 2671-2688.

Ware, A., Lacey, J., *Optical Switches in the Next-Generation Transport Network*, Telecommunications, (2000), **6**, S8-S12.

Weidel, E., *New Coupling Method in GaAs-laser-fiber coupling*, Electro. Lett., (1975), 11, 436-437.

Wu, M.C., *Micromachining for Optical and Optoelectronics Systems*, Proceedings of the IEEE, (1997), **85 (11),** 1833-1856.

Zhang, **N**, *Method of Etching a Wafer Layer Using a Sacrificial Wall and Structure Formed Thereby*, U.S. Patent Application S/N 09/372,700.

Zhang, **N**., *Method of Etching a Wafer Layer Using Multiple Layers of the Same Photoresistant Material and Structure Formed Thereby*, S/N 09/372,428.

Zhang N., *Microelectromechanical Optical Switch and Method of Manufacture Thereof*, U.S. Patent Application S/N 09/372, 265.

Zhang, N., *An Efficient, Low Loss Technique for Coupling Fibers to Photonic Devices Thereby*. 2000.

Zhang, N., *Improvement of Switch Output Channel Uniformity by Using On-chip Optical Path Balance Approach Thereby*. 2000.

Zhang, N., *Compact 1x4 Optical Switch Design on Single MEMS chip Thereby*. 2000.

APPENDIX A: COMB ACTUATOR STABILITY CONSIDERATIONS

Through the actuation testing, the stability is the key character to evaluate the actuator performance. As observed in Ref 24 of Chapter 2, the actuator with smaller gap is more likely to be unstable and fail to operate with smaller displacement. Here," unstable" means the situation in which the teeth of the electrode move in the direction perpendicular to the stroke direction and touch the stationary electrode. In this case, the short-circuit occurs and the actuators stops operating. Figure A1 schematically illustrates one moving electrode tooth placed between stationary electrode teeth. In this Figure, V is the applied voltage across the electrodes, g is the gap width, and l is the length of the overlap of the electrodes. The moving electrode tooth is suspended by two mechanical springs with spring constants of k_y in the direction perpendicular to the stroke and k_x in the direction of the stroke, respectively. Assume that the moving electrode tooth moves y in the Y direction; then the electrostatic force F_y generated by both sides of the parallel plate is

$$F_y = \frac{\varepsilon t l}{2(g-y)^2}V^2 - \frac{\varepsilon t l}{2(g+y)^2}V^2 \qquad \text{(A.1)}$$

Here, t is the thickness of the electrodes. A positive value of F_y proves that the suspended electrode is unstable. It looks as if there were a 'negative' spring. The equivalent 'negative' spring constant k_e when the moving tooth is placed at the center of the gap is

$$k_e = \frac{\partial F_y}{\partial y}\Big|_{y=0} = \frac{2\varepsilon t l V^2}{g^3} \qquad \text{(A.2)}$$

The mechanical spring with spring constant k_y keeps the position of the moving electrode against the instability of the electrostatic force. If $|k_y| > |k_e|$, the electrode stays stable; otherwise, the electrode become unstable and touches to the stationary electrode. Hence, to keep the electrode stable

$$|k_y| > \left|\frac{2\varepsilon t l V^2}{g^3}\right| \tag{A.3}$$

must be satisfied. Both terms are independently controlled; k_y is determined by the suspension design, and the expression on the right-hand side is determined by the gap width, overlap length, electrode thickness and applied voltage. Three tendencies are inferred from the equation above.

1) When we decrease the gap width, the instability increases proportionally to the inverse cube of the gap width g.
2) Instability increases proportional to the square of the applied voltage V.
3) Instability is proportional to the overlap length.

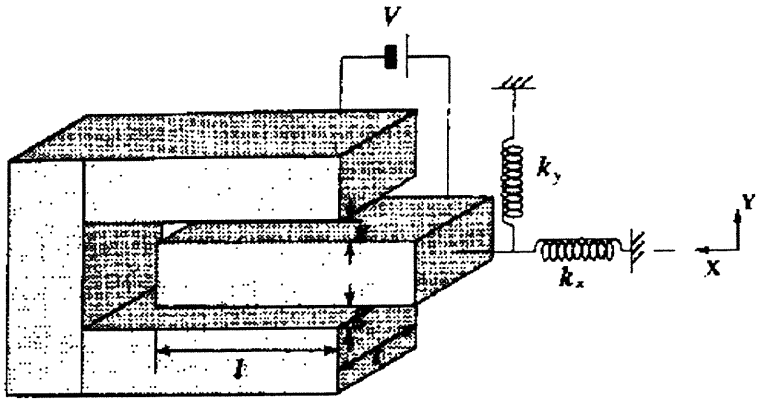

Figure A.1 Finger schematic diagram.

From 2) it is apparent that limiting the maximum applied voltage is quite important. To drive the electrostatic actuator, a commonly used technique is to apply a high bias voltage with a comparatively low operational voltage, but this is disadvantageous when the gap is small and instability is the dominant problem.

Item 3) implies that it is important to reduce the overlap length. Hence, it is advantageous to design initial overlap length as small as possible to get a long stroke.

Obviously, increasing the spring constant of the suspension k_y is the most effective way to stabilize the actuator. The ideal suspension is the suspension with a low k_x and at the same time with quite high k_y.

APPENDIX B: PROCESSING/QUALITY CONTROL FLOW

Process/Quality Control Flow Chart-1

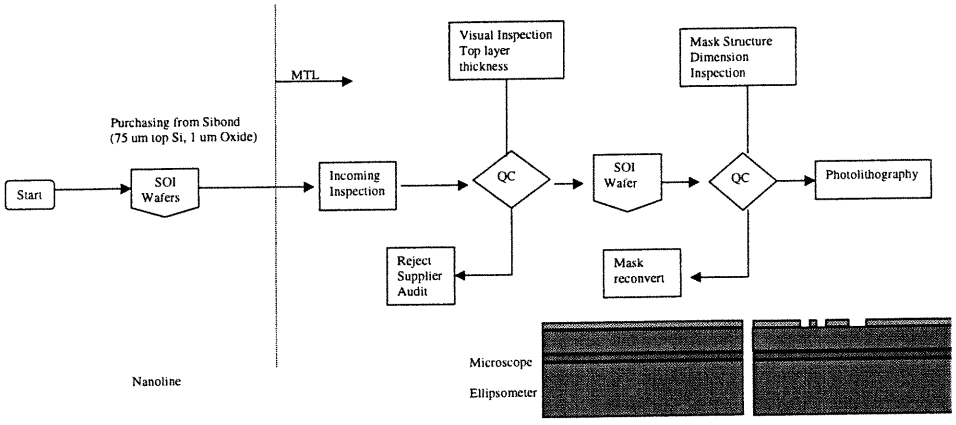

Process/Quality Control Flow Chart-2

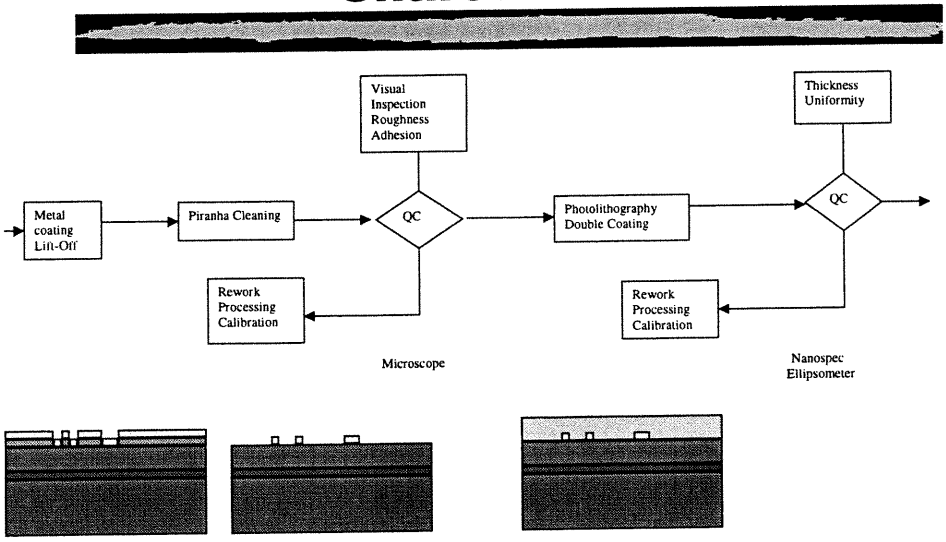

Process/Quality Control Flow Chart-3

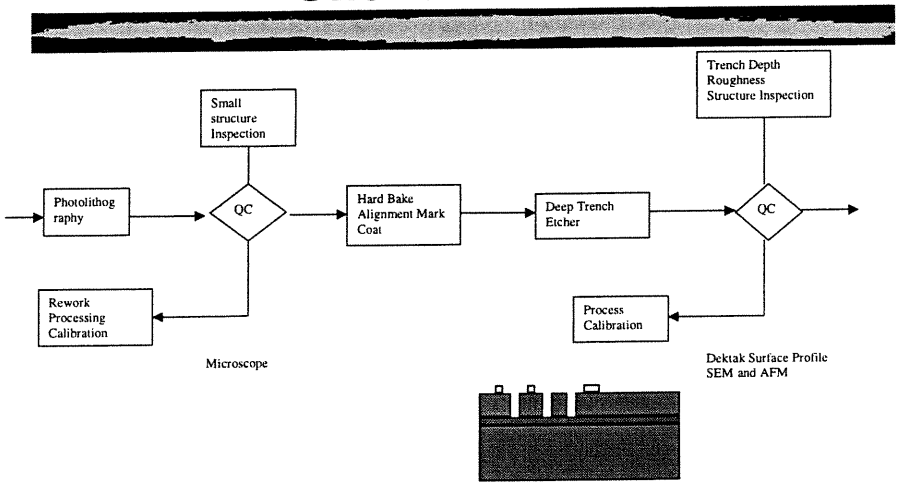

Process/Quality Control Flow Chart-4

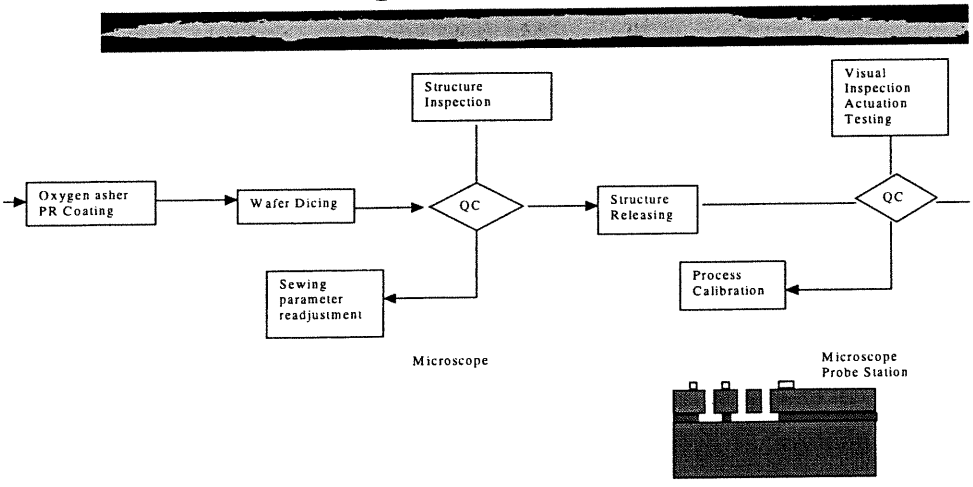

Process/Quality Control Flow Chart-5